

AD-A134 357

AN INVESTIGATION OF TIP-WALL VORTEX CAVITATION IN AN
AXIAL-FLOW PUMP. (U) PENNSYLVANIA STATE UNIV UNIVERSITY
PARK APPLIED RESEARCH LAB. B H SHUBA 27 MAY 83

1/2

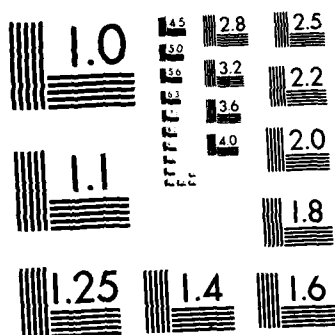
UNCLASSIFIED

ARL/PSU/TM-83-89 N00024-79-C-6043

F/G 20/4

NL





MICROCOPY RESOLUTION TEST CHART
NATIONAL BUREAU OF STANDARDS-1963-A

AD-A134357

6

AN INVESTIGATION OF TIP-WALL VORTEX CAVITATION
IN AN AXIAL-FLOW PUMP

B. H. Shuba

Technical Memorandum
File No. TM 83-89
May 27, 1983
Contract No. N00024-79-C-6043

Copy No. 19

The Pennsylvania State University
Applied Research Laboratory
Post Office Box 30
State College, PA 16801

Approved for Public Release
Distribution Unlimited

NAVY DEPARTMENT

NAVAL SEA SYSTEMS COMMAND

DTIC FILE COPY

[Handwritten signature and stamp]

REPORT DOCUMENTATION PAGE		READ INSTRUCTIONS BEFORE COMPLETING FORM
1. REPORT NUMBER TM 83-89	2. GOVT ACCESSION NO. AD-A134357	3. RECIPIENT'S CATALOG NUMBER
4. TITLE (and Subtitle) AN INVESTIGATION OF TIP-WALL VORTEX CAVITATION IN AN AXIAL-FLOW PUMP		5. TYPE OF REPORT & PERIOD COVERED Technical Memorandum
		6. PERFORMING ORG. REPORT NUMBER
7. AUTHOR(s) B. H. Shuba		8. CONTRACT OR GRANT NUMBER(s) N00024-79-C-6043
9. PERFORMING ORGANIZATION NAME AND ADDRESS Applied Research Laboratory Post Office Box 30 State College, PA 16801		10. PROGRAM ELEMENT, PROJECT, TASK AREA & WORK UNIT NUMBERS
11. CONTROLLING OFFICE NAME AND ADDRESS Naval Sea Systems Command Department of the Navy Washington, DC 20362		12. REPORT DATE May 27, 1983
		13. NUMBER OF PAGES 120
14. MONITORING AGENCY NAME & ADDRESS (if different from Controlling Office)		15. SECURITY CLASS. (of this report) UNCLASSIFIED
		15a. DECLASSIFICATION DOWNGRADING SCHEDULE
16. DISTRIBUTION STATEMENT (of this Report) Approved for public release. Distribution unlimited per NAVSEA - Sept. 7, 1983.		
17. DISTRIBUTION STATEMENT (of the abstract entered in Block 20, if different from Report)		
18. SUPPLEMENTARY NOTES		
19. KEY WORDS (Continue on reverse side if necessary and identify by block number) thesis, leakage, vortex, cavitation		
20. ABSTRACT (Continue on reverse side if necessary and identify by block number) This is an investigation of tip-wall vortex cavitation in axial-flow pumps. This form of cavitation occurs in pumps, and its effects need to be minimized. Because this form of vortex cavitation is not completely understood, a study of it is required. A relationship is required to predict the trends in tip-wall vortex cavitation.		

20. Previous investigations in clearance flows and vortex cavitation in axial-flow pumps are reviewed to determine the important flow field parameters. The tip clearance, rotor RPM, and tip-wall boundary-layer velocity profile are hypothesized to be the important parameters. An experimental program was conducted that determines the desinent cavitation number for correlation with these parameters.

Analysis of the data reveals the optimization required to minimize the occurrence of tip-wall vortex cavitation. The optimum clearance occurs for a clearance-to-maximum tip thickness ratio, λ , less than 0.15 depending on the form of cavitation observed in the tip region. If tip-wall vortex cavitation occurs, the optimum clearance ratio is less than 0.15. If gap cavitation in the clearance occurs, the optimum clearance ratio is near 0.15. Also, cavitation performance is improved for lower rotor RPM and a less-full endwall boundary-layer profile. Both give a decrease in the lift on the tip and, therefore, improve the cavitation performance.

A parametric correlation model is developed from Rankine vortex relationships. The model, which is a function of clearance and tip incidence velocity, predicts the slope of the cavitation number-clearance ratio trend in the range of $0.1 < \lambda < 0.4$. The magnitudes of the predicted values are determined by the only unspecified constant of the model. A recommendation is made to determine the value of this constant.



ABSTRACT

This is an investigation of tip-wall vortex cavitation in axial-flow pumps. This form of cavitation occurs in pumps, and its effects need to be minimized. Because this form of vortex cavitation is not completely understood, a study of it is required. A relationship is required to predict the trends in tip-wall vortex cavitation.

Previous investigations in clearance flows and vortex cavitation in axial-flow pumps are reviewed to determine the important flow field parameters. The tip clearance, rotor RPM, and tip-wall boundary-layer velocity profile are hypothesized to be the important parameters. An experimental program was conducted that determines the desinent cavitation number for correlation with these parameters.

Analysis of the data reveals the optimization required to minimize the occurrence of tip-wall vortex cavitation. The optimum clearance occurs for a clearance-to-maximum tip thickness ratio, λ , less than 0.15 depending on the form of cavitation observed in the tip region. If tip-wall vortex cavitation occurs, the optimum clearance ratio is less than 0.15. If gap cavitation in the clearance occurs, the optimum clearance ratio is near 0.15. Also, cavitation performance is improved for lower rotor RPM and a less-full endwall boundary-layer profile. Both give a decrease in the lift on the tip and, therefore, improve the cavitation performance.

A parametric correlation model is developed from Rankine vortex relationships. The model, which is a function of clearance and tip incidence velocity, predicts the slope of the cavitation number-clearance

ratio trend in the range of $0.1 < \lambda < 0.4$. The magnitudes of the predicted values are determined by the only unspecified constant of the model. A recommendation is made to determine the value of this constant.

TABLE OF CONTENTS

	<u>Page</u>
ABSTRACT	iii
LIST OF TABLES	vii
LIST OF FIGURES	viii
NOMENCLATURE	xi
ACKNOWLEDGMENTS	xiv
CHAPTER I: INTRODUCTION	1
1.1 Background	1
1.2 Objectives of the Investigation	3
CHAPTER II: PREVIOUS INVESTIGATIONS	6
2.1 Leakage Flows in Axial-Flow Compressors	6
2.1.1 The Rotor Tip Flow Field	6
2.1.2 Tip Flow Investigation By Gearhart	10
2.1.3 Axial Compressor Investigation by Lakshminarayana	11
2.2 Tip-Wall Vortex Cavitation Investigations	12
2.2.1 Leakage Flow Investigation by Rains	12
2.2.2 Axial-Flow Pump Cavitation Experiments by Mitchell	18
2.2.3 Comments on the Investigations of Rains and Mitchell	23
2.3 Vortex Investigations and Development	24
2.3.1 Trailing Vortex Investigations	24
2.3.2 Rankine Vortex Development	25
CHAPTER III: EXPERIMENTAL PROGRAM	29
3.1 Experimental Parameters	29
3.2 Experimental Apparatus	32
3.3 Experimental Program	35
3.4 Experimental Flow Visualization Technique	39

	<u>Page</u>
CHAPTER IV: EXPERIMENTAL DATA	42
4.1 Velocity Profiles	42
4.2 Cavitation Data	47
4.2.1 The σ - λ Trend	47
4.2.2 The σ -RPM Trend	63
4.2.3 The σ -Boundary Layer Trend	65
4.2.4 Discussion of the Experimental Data	71
4.3 Flow Visualization Results	72
CHAPTER V: PARAMETRIC CORRELATION MODEL	78
5.1 Requirements of the Model	78
5.2 Derivation of Circulation and Core Radius Sub-Models	79
5.3 Application and Discussion of the Model	83
CHAPTER VI: CONCLUSIONS OF THE INVESTIGATION	94
6.1 Conclusions from the Experimental Program	94
6.2 Conclusions of the Parametric Correlation Model	96
CHAPTER VII: RECOMMENDATIONS FOR FURTHER RESEARCH	97
REFERENCES	99
APPENDIX: DERIVATION OF SECONDARY AND VORTEX CIRCULATION	101

LIST OF TABLES

<u>Table</u>		<u>Page</u>
I	Tip-Wall Boundary-Layer Integral Properties	46
II	Comparison of Secondary and Vortex Circulation	104

LIST OF FIGURES

<u>Figure</u>		<u>Page</u>
1	Leakage Vortex Cavitation in an Axial Pump	4
2	Flow Field of an Axial-Flow Pump Rotor Blade	7
3a	Rains' Cavitation Data for a Stationary Blade	17
3b	Rains' Cavitation Data for an Axial-Flow Pump	17
4a	Mitchell's Cavitation Data for an Axial-Flow Pump at 600 RPM	19
4b	Mitchell's Cavitation Data for an Axial-Flow Pump at 675 RPM	20
4c	Mitchell's Cavitation Data for an Axial-Flow Pump at 750 RPM	21
5	Axial and Tangential Velocity Profiles of a Trailing Vortex	26
6a	Rankine Vortex Velocity Field	27
6b	Rankine Vortex Pressure Field	27
7	Boundary-Layer Growth with Screen Length	31
8	Schematic of Apparatus in Test Section	33
9	Water Tunnel and Laser System	36
10	Schematic of Laser Velocimeter System	37
11a	Boundary-Layer Profiles for Configuration 1	43
11b	Boundary-Layer Profiles for Configuration 2	44
11c	Boundary-Layer Profiles for Configuration 3	45
12a	Axial Velocity Profile Entering the Rotor	48
12b	Tangential Velocity Profile Entering the Rotor	49
13a	Cavitation Desinence Data for Configuration 1 with Air Content Effects	51
13b	Cavitation Desinence Data for Configuration 2 with Air Content Effects	52

<u>Figure</u>		<u>Page</u>
13c	Cavitation Desinence Data for Configuration 3 with Air Content Effects	53
14a	Cavitation Desinence Data for Varying RPM from Air Content Test	54
14b	Cavitation Desinence Data for Varying Air Content from Air Content Test	54
15a	Cavitation Desinence Data for Configuration 1 Corrected for Air Content	56
15b	Cavitation Desinence Data for Configuration 2 Corrected for Air Content	57
15c	Cavitation Desinence Data for Configuration 3 Corrected for Air Content	58
16	Comparison of Cavitation Data from Mitchell's, Gearhart's and the present investigation	62
17	Variation of Desinent Cavitation Number with RPM for Configuration 3	64
18	Variation of W_1 with Clearance Ratio for Configuration 3	67
19a	Variation of Cavitation Number with W_1/V_∞	68
19b	Variation of Cavitation Number with $(W_1/V_\infty)^2$	68
20	Variation of i with Clearance Ratio	70
21a	Oil-Paint Film Pattern on Pressure Surface	73
21b	Oil-Paint Film Pattern on Tip Surface	74
21c	Oil-Paint Film Pattern on Suction Surface	75
22	Comparison of Experimental Data and Model Results for the Present Investigation	85
23	Comparison of Experimental Data and Model Results for Mitchell's Investigation	87
24	Comparison of Experimental Data and Model Results for Gearhart's Investigation	88

<u>Figure</u>		<u>Page</u>
25	Model Estimates of Shed Lift Coefficient	89
26	Model Estimates of Vortex Core Radius	90
27	Variation of B with Reynolds Number	92

NOMENCLATURE

a	vortex core radius
A	area
b	distance of discontinuity surface from suction side
B	constant
B_{INT}	intercept on B axis
c	chord
C_L	lift coefficient
C_{L0}	lift coefficient at tip
C_{LT}	shed lift coefficient at tip
C_p	pressure coefficient
$C_{p_{min}}$	minimum pressure coefficient
h	clearance size
H	shape factor
i	tip incidence angle
k_s	equivalent sand grain roughness
\underline{n}	normal vector
P	static pressure
P_v	vapor pressure
r	radial coordinate
r_c	discontinuity surface radius
r_r	rotor radius
Re	Reynolds number
t_{max}	maximum tip thickness
t^*	vortex time-like parameter
u	boundary-layer velocity

u_{∞}	boundary-layer edge velocity
U_T	rotor tip speed
V	velocity
V_1	rotor inlet velocity
V_2	rotor exit velocity
V_x	axial velocity
V_{θ}	tangential velocity
V_{∞}	free stream velocity
W	relative velocity
W_1	relative tip incidence velocity
W_x	relative axial velocity
W_{θ}	relative tangential velocity
x	axial coordinate
α	angle of attack
α_{CAM}	camber angle
α_{STAG}	stagger angle
β	relative flow turning angle
β_1	relative flow inlet angle
β_2	relative flow outlet angle
Γ	circulation
Γ^*	circulation at vortex station
δ	boundary-layer thickness
δ^*	boundary-layer displacement thickness
ε	thickness-to-chord ratio
θ	boundary-layer momentum thickness
λ	clearance-to-maximum tip thickness ratio

ν	kinematic viscosity
ξ	vortex coordinate
ρ	density
σ	cavitation number
ϕ	flow coefficient
ω	vortex angular velocity
$\boldsymbol{\omega}$	vorticity vector
$\boldsymbol{\omega}_n$	vorticity vector in normal direction
$\boldsymbol{\omega}_n'$	vorticity vector in relative normal direction
$\boldsymbol{\omega}_{s_1}'$	inlet vorticity vector in relative streamwise direction
$\boldsymbol{\omega}_{s_2}'$	outlet vorticity vector in relative streamwise direction
Ω	rotor angular velocity

ACKNOWLEDGMENTS

I wish to express my appreciation to Dr. Michael L. Billet, a member of the research staff at the Garfield Thomas Water Tunnel, for his invaluable assistance throughout the course of this investigation. Also, I thank Walter S. Gearhart, a member of the research staff at the Garfield Thomas Water Tunnel, and Dr. Budugar Lakshminarayana, Professor of Aerospace Engineering, for their helpful discussions concerning this investigation. Lastly, I thank the staff of the Garfield Thomas Water Tunnel who assisted in the conduction of this investigation.

This investigation was conducted at the Garfield Thomas Water Tunnel at The Pennsylvania State University under the sponsorship of the Cavitation and Cavitation Noise Program of the Naval Sea Systems Command.

CHAPTER I

INTRODUCTION

1.1 Background

Many forms of cavitation are found in axial-flow pumps such as blade surface, trailing vortex, and tip vortex. This investigation is concerned with tip-wall vortex cavitation which is the form of tip vortex cavitation that occurs in pumps. The distinction between tip and tip-wall vortex cavitation is due to the physical design of the pump. Tip-wall vortex cavitation occurs for rotor/tip-wall interactions in pumps whereas tip vortex cavitation does not have tip-wall interactions.

The term tip-wall or "leakage" vortex originates from early investigations (1,2) of cascade and turbomachinery flows using flow visualization. These investigations showed that a vortex was shed from the suction side of the rotor blade tip. In these investigations a clearance existed between the blade tip and the tip-wall. The flow that passed through the clearance from the pressure side to the suction side was called the leakage flow. The flow visualization showed that the interaction of the leakage flow with the through flow on the suction side formed a sheet of vorticity that rolled up into a vortex, i.e., the tip-wall or leakage vortex.

In a liquid medium, such as water, the pressure in the tip-wall vortex may drop to the vapor pressure of the medium, and vortex cavitation would result. Thus, this form of cavitation is called tip-wall vortex cavitation.

As observed for cavitating vortex flows, tip-wall vortex cavitation inception occurs before other types of cavitation that may occur in a pump. All forms of cavitation are quantified by the cavitation number, σ ,

$$\sigma = \frac{P - P_v}{\frac{1}{2} \rho V_\infty^2} \quad (1)$$

Poor cavitation performance occurs for high cavitation numbers. Therefore, tip-wall vortex cavitation will have higher cavitation numbers than any other form of pump cavitation. Since cavitation is not desired in most instances, a means of reducing the tip-wall vortex cavitation number is required. However, this form of cavitation is not completely understood, so it is difficult to improve or estimate cavitation performance. The parameters of the flow field that influence tip-wall vortex cavitation have not been completely defined. Thus, an investigation to determine these parameters is required.

In addition to decreasing the cavitation performance of a pump, tip-wall vortex cavitation has other negative aspects such as flow energy losses and material damage. Flow energy losses occur because some flow intended to pass through the rotor disk instead passes through the clearance as the leakage flow. This flow is not given a momentum increase by the pump and, hence, the pump efficiency is decreased. The collapsing cavitation bubbles that are located near the tip-wall can result in material damage to the tip-wall over a period of time.

A photograph of tip-wall vortex cavitation in an axial-flow pump is shown in Figure 1. The rotor blade is moving from the bottom to the top of the photograph, and the axial-flow direction is from left to right. The cavitating vortex originates at the midchord station on the rotor suction side and trails downstream. The vortex is not attached to the blade, and no surface cavitation is seen on the tip. This photograph is typical of tip-wall vortex cavitation.

1.2 Objectives of the Investigation

Tip-wall vortex cavitation is not completely understood. The parameters that effect the size and strength of the tip-wall vortex are not defined. If tip-wall vortex cavitation is to be minimized, these parameters must be determined. Therefore, the objectives of the investigation are to determine the important parameters, conduct cavitation experiments investigating these parameters, and generate an empirical model for tip-wall vortex cavitation.

The first objective, determining the important parameters, will be accomplished by reviewing both the rotor tip flow field and previous investigations of tip-wall vortex cavitation. The rotor tip flow field of a pump is complex and must be understood before any conclusions are made about the formation of the tip-wall vortex. Reviewing the previous investigations serves two purposes. First, these investigations provide insight for the assumptions concerning the important parameters. Secondly, the data from these investigations serve as a basis for comparison with data from the present investigation.

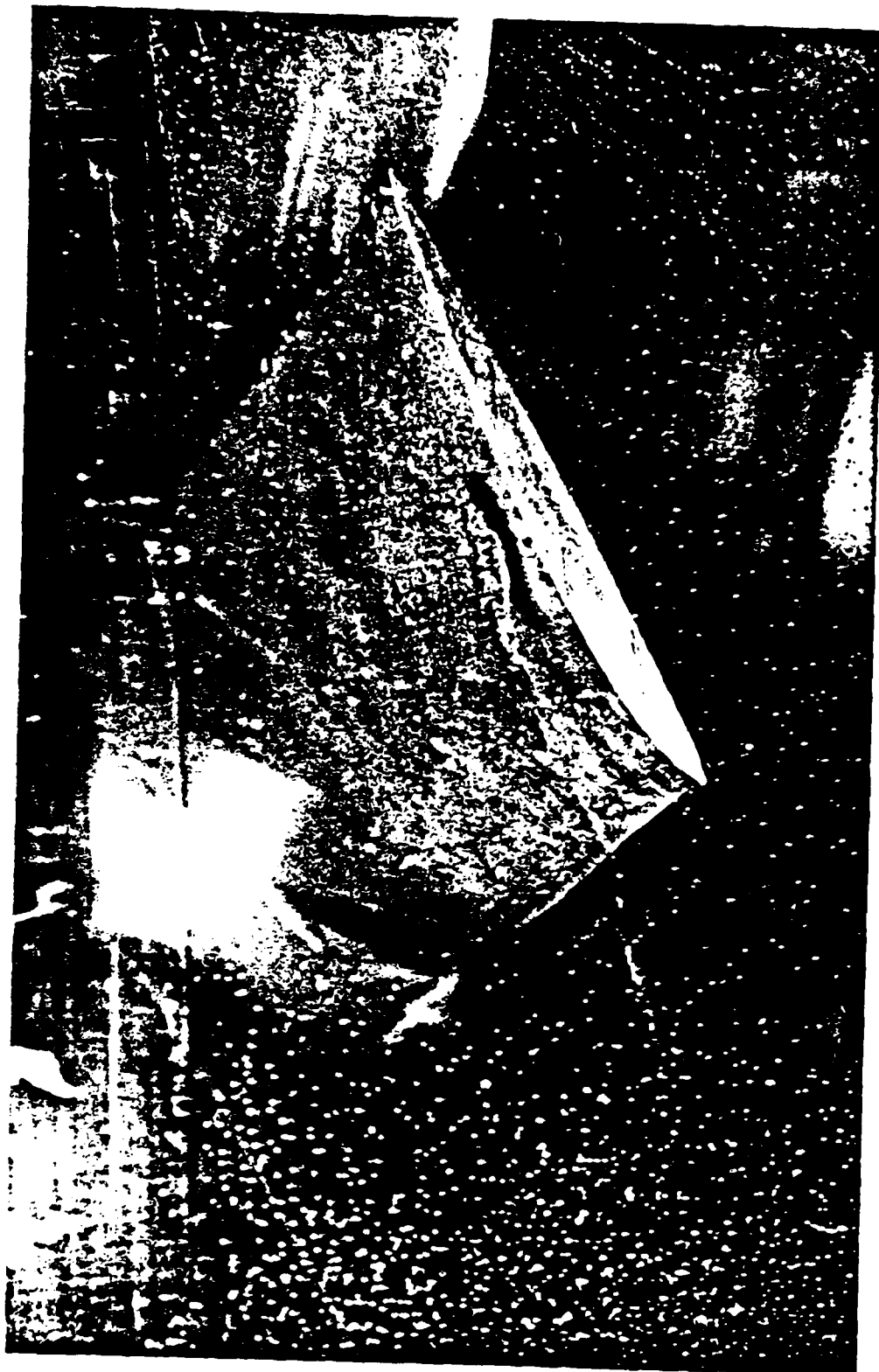


Figure 1. Leakage Vortex Cavitation in an Axial Pump.

Once the important parameters have been determined, an experimental program will be conducted. During this program, cavitation data will be obtained for a pump stage as the parameters are varied. Thus, the results of the program will provide the cavitation number as a function of these parameters. The cavitation data will be analyzed to obtain a correlation of the important parameters, and these data will be compared with previous : p-wall vortex cavitation data to correlate the important trends.

The last objective of this investigation is to generate an empirical model that will predict cavitation performance of the tip-wall vortex. This model will determine the cavitation number, or the minimum pressure coefficient, of the tip-wall vortex as a function of the important parameters of the pump flow field. The model will be derived from the trends of the experimental data and any analytical models developed in the previous investigations.

CHAPTER II

PREVIOUS INVESTIGATIONS

2.1 Leakage Flows in Axial-Flow Compressors

2.1.1 The Rotor Tip Flow Field. Axial-flow pumps, like axial-flow compressors, have complex flow fields. The complexity is due to the three-dimensional rotative nature of the pump. For instance, varying airfoil cross section, blade stagger and lean, rotor rotation, and inlet swirl all contribute to the complex flow field of a pump stage. Therefore, three-dimensional velocity and pressure fields are not easily calculated for a given geometry. A typical pump flow field is illustrated in Figure 2. As can be noted, the blade passage velocity components and boundary layers on the root-wall, blade surface, and tip-wall are significant as are the blade wakes. All of the complexity of the flow field is compounded in the tip region by the existence of the clearance. Because of this complexity, no complete analytical solution exists for the rotor tip flow field.

Figure 2 illustrates the leakage vorticity generated in the rotor tip region. The vorticity is important because it leads directly to the tip-wall vortex. Recalling vorticity laws, the leakage vorticity must be the sum of other vorticities either entering or generated in the tip region. Other vorticities in the tip region include the shed vorticity generated by the rotor and shed at the tip, the secondary vorticity generated by the flow turning through the clearance, and the scraping vorticity generated by the rotor tip

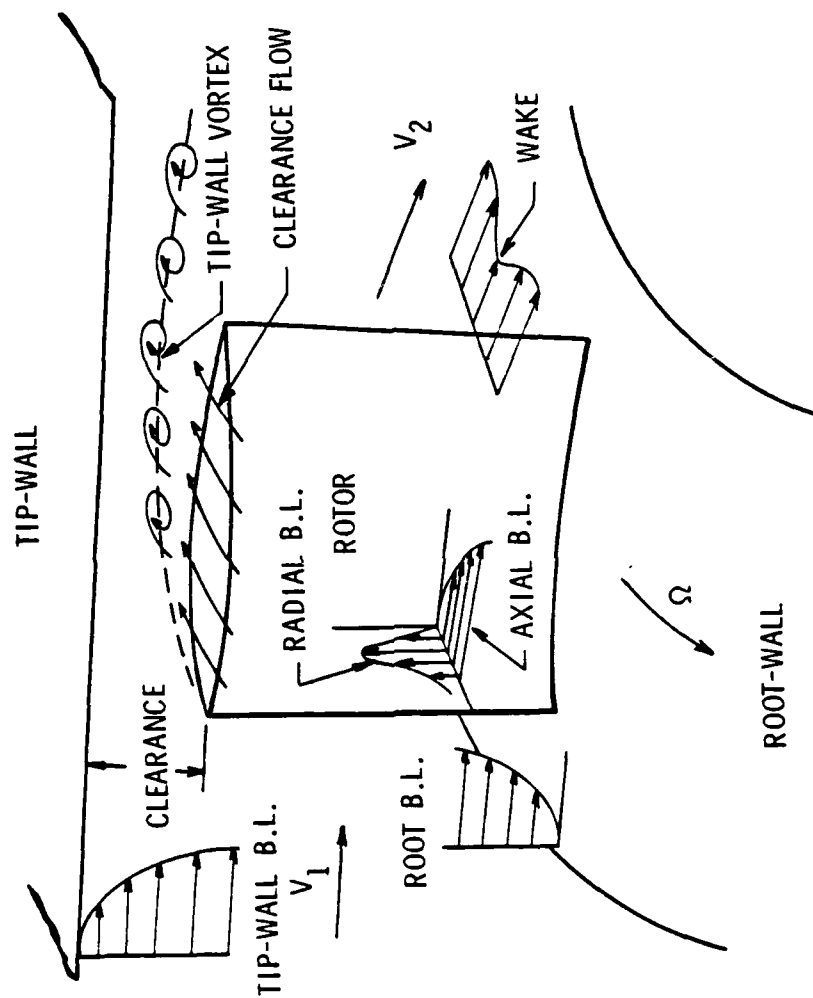


Figure 2. Flow Field of an Axial-Flow Pump Rotor Blade.

"scraping" the tip-wall boundary layer into a vortex. The shed and secondary vorticities form on the suction side of the rotor blade while the scraping vorticity forms on the pressure side and passes through the clearance to combine with the other vorticities.

For most pump stages the scraping and secondary vorticities are expected to be lower in magnitude than the shed vorticity. The clearance-to-span ratio is too high to allow for a strong scraping vorticity, and the turning of the leakage flow is too small to generate a strong secondary vorticity. An estimation of the secondary vorticity is derived in the Appendix. This estimation proves that the secondary vorticity is an order of magnitude lower than the vorticity expected in the tip-wall vortex. Since the scraping and secondary vorticities are small, the shed vorticity is expected to be of the same order as the leakage vorticity.

Vorticity is not easily measured in a flow, so measurements of other parameters that effect the vorticity are made and then correlated with these parameters. For a pump stage, the rotation, clearance, tip-wall, and blade geometric properties are expected to effect the shed vorticity and, correspondingly, the leakage vorticity which directly effects the cavitation performance.

Rotation infers that a relative velocity, that is used to calculate a Reynolds number, is associated with the rotor. Historically, many forms of cavitation have been correlated with Reynolds number. However, this correlation is done using the rotational speed, RPM, instead of the Reynolds number directly. Also, rotation effects the

lift of the blade tip as described by Dean (3). He found that blade loading increased with rotational speed for constant clearance. Blade loading, or lift, affects the tip-wall vortex. Thus, the cavitation performance may correlate with rotation in more than one parameter.

The size of the clearance and the velocity of the leakage flow limits the mass flow through the clearance. The mass flow through the clearance determines the degree of interaction between the leakage flow and the through flow on the suction side. This interaction produces the tip-wall vortex, so the tip-wall vortex is functionally dependent on the clearance.

The tip-wall is important to the flow field because a boundary layer forms on it. Generally, this boundary layer has a thickness greater than the clearance, so the rotor tip operates in an axial velocity lower than that found outside the boundary layer. Therefore, the loading on the tip changes which effects the tip-wall vortex. Also, since a boundary layer forms on the tip-wall and the rotor tip, a shear flow exists in the clearance.

Several of the rotor blade geometric properties such as the tip thickness and airfoil shape might be important to the tip-wall vortex. The tip thickness effects the development of the leakage flow in the clearance since the thickness corresponds to a length scale for the flow. The leakage flow can be thought of as a Couette flow that requires a finite length scale for complete development. Also, the airfoil cross section at the tip determines the pressure difference, and hence the lift, across the tip. The tip-wall vortex depends on tl

lift and, therefore, the airfoil cross section at the tip. The location of cavitation inception depends on the chordwise pressure distribution and the location of the minimum pressure both of which are determined by the airfoil cross section.

2.1.2 Tip Flow Investigation by Gearhart. Gearhart's investigation (4) attempted to determine the best tip shape of a rotor blade for optimum gap and vortex cavitation performance. Here, gap cavitation is defined as cavitation that occurs in the clearance region. His investigation included wind tunnel tests with a stationary rotor blade and moveable tip-wall. He measured the pressure drop across the clearance and conducted flow visualization tests. Because his tests were conducted in a wind tunnel, Gearhart's comments concerning cavitation were only inferred. The velocity at the exit of the clearance region determined the vortex cavitation performance while minimizing the separated flow region in the clearance improved gap cavitation.

For vortex cavitation, Gearhart concluded that a lower magnitude of the mean velocity at the exit of the clearance region improved performance. He found that a tip shape that diverged from pressure to suction side had a lower mean velocity at the clearance exit than a normal or converging tip shape. The diverging section reduced the mean velocity from the entrance to the exit of the clearance because of the area-velocity conservation for incompressible flow. Thus, a diverging tip shape had improved vortex cavitation performance.

From flow visualization studies, Gearhart observed that separation of the leakage flow from the tip surface in the clearance

led to gap cavitation. When a separate region occurred, a venturi effect existed in the clearance with high velocities and low pressures. The separation region occurred because the flow entering from the pressure side did not adhere to the blade surface. Gearhart found that rounding the corner formed by the pressure and tip surfaces reduced the amount of separation observed. Also, Gearhart found that a converging tip shape showed better separation characteristics than normal or diverging tip shapes. Thus, the optimum gap cavitation performance was given by rounding the clearance inlet corner and using a converging tip shape.

2.1.3 Axial Compressor Investigation by Lakshminarayana.

Lakshminarayana investigated tip flows in axial-flow compressors (5,6). Primarily, an analytic model was developed to predict blade-to-blade effects of the leakage flow. This development included discussions on shed lift and vorticity that will be presented here.

When developing this model, Lakshminarayana found through experiment that not all the circulation, or lift, was shed because the blade tip was near the tip-wall. He defined a shed lift coefficient as the ratio of shed lift to total lift at the tip. During the experiments, the shed lift was found to vary with the clearance. Specifically, the shed lift varied with the clearance to the $2/3$ power. For a certain range, Lakshminarayana simplified this power relationship to a linear variation with clearance. Thus, any model that uses the lift coefficient as a parameter to predict cavitation performance

must determine the variation of shed lift with clearance if the clearance is a parameter of the model.

As described in Section 2.1.1, three vorticities, the shed, secondary, and scraping, contribute to the leakage vorticity. Lakshminarayana hypothesized that if the sense of these vorticities differed their sum could be zero. He referred to a zero sum as optimum because it eliminated the tip-wall vortex and velocities associated with it. In this case, the flow field calculations in the tip region are simplified. In reality, the sum of the vorticities is not likely to be zero since the shed vorticity is much larger in magnitude than the other vorticities. Thus, optimum cavitation performance is found when the vorticities sum to a minimum value.

2.2 Tip-Wall Vortex Cavitation Investigations

2.2.1 Leakage Flow Investigation by Rains. Rains' investigation (7) pioneered tip clearance flow studies in axial-flow pumps. His investigation concerned the leakage flow and the formation of the tip-wall vortex. He developed analytic models for both flows and conducted cavitation experiments to confirm his results. Although mainly concerned with flow-energy losses, Rains' investigation represents a beginning for development of an analytic model and a data base for comparison of cavitation data.

Rains assumed an inviscid model for the flow at the exit of the clearance. The model consisted of a stiff jet that exited a slot and entered a cross flow at some angle. The stiff jet modelled the flow that exited the clearance, and the cross flow modelled the through flow

on the suction side of the rotor blade. Because the two flows have different magnitudes and directions, a discontinuous surface forms between them. Rains used discrete point vortex equations to calculate the deformation of the surface of discontinuity. A time-like parameter, t^* , determined the degree of deformation of the surface. t^* is written as

$$t^* = \frac{(\xi/c) C_{L_o}^{1/2}}{\lambda \epsilon} \quad (2)$$

where c is the blade tip chord, C_{L_o} is the lift coefficient at the tip, λ is the clearance-to-maximum tip thickness ratio, and ϵ is the thickness-to-chord ratio. ξ is the coordinate in the direction of the tip-wall vortex axis.

The derivation of Rains' model continued by determining equations for the radius of the rolled up discontinuity surface, r_c , and the length of the discontinuity surface, b . Both are given as functions of t^* as

$$r_c = 0.14 h t^{*.85} \quad (3)$$

$$b = 1.0 h t^{*.72} \quad (4)$$

Since r_c and b are functions of t^* , both increase continuously from the origin of the tip-wall vortex to some point downstream.

Applying the Rankine vortex pressure coefficient equation, Rains continued the derivation by defining the circulation, Γ^* , in the vortex. Again, the relationship is a function of t^* as well as the tip lift coefficient

$$\Gamma^* = \lambda \epsilon \left[\frac{4.0 + C_{L_o}}{C_{L_o}} \right]^{\frac{1}{2}} \frac{r_c}{h} \quad (5)$$

Note that blade geometric properties enter these equations.

Lastly, Rains developed an expression for the cavitation number, σ , of the vortex. He assumed that the vortex pressure field was superimposed on the pressure at the blade suction side. The expression was given as

$$\sigma = -C_p + \frac{C_{L_o} (4 + C_{L_o}) (r_c/h)^2}{8\pi^2 (1 + b/h)^2} \quad (6)$$

Again, the equation was a function of ϵ^* and C_{L_o} . The C_p term was found from the rotor suction side pressure measurements. The second term in Equation 6 was derived from the Rankine vortex pressure coefficient relationship using Equations 3 and 5 for the core radius and circulation, respectively. Equation 6 determined cavitation number for varying values of ξ that corresponded to chordwise stations. C_p was found at these chordwise stations that corresponded to the value of ξ being used in Equation 6.

In deriving Equation 6, Rains made three important assumptions. First, he assumed that the blade tip had zero thickness and that the pressure distribution was constant along the chord. In reality the blade tip had a finite thickness and a varying pressure distribution. Rains proposed that this difference would shift the origin of the ξ coordinate from the tip leading edge. Secondly, Rains estimated values

for the lift coefficient at the tip because they were not measured experimentally. Rains assumed that the presence of the tip-wall boundary layer increased the loading on the blade tip and that the only effect of rotation was to increase the loading on the tip. To account for the tip-wall boundary layer and the rotational effects, Rains developed an empirical relationship for the tip lift coefficient that included the free stream lift and lift generated by the presence of the tip-wall boundary layer. Lastly, Rains assumed that the secondary vorticity near the tip was distributed uniformly over the tip-wall region. He implied that no discrete secondary vortex formed. Therefore, he neglected the contribution of the secondary vorticity to the leakage vorticity.

In addition to the development of the analytical model, Rains conducted tip-wall vortex cavitation experiments for a stationary blade and an axial-flow pump configuration. This was done to determine the effect of rotation. The parameters of the experiments were the clearance and the flow coefficient. The flow coefficient was the mean value for the entire configuration.

The stationary blade was similar in design to the rotor blade used in the axial-flow pump. The clearance was varied by traversing the blade normal to the tip-wall. Rains developed an angle-of-attack/flow coefficient analogy for the stationary blade. This analogy converted angle-of-attack for the stationary blade into a flow coefficient for the axial-flow pump. Thus, flow coefficient trends could be compared between the two configurations.

The data from Rains' cavitation tests are shown in Figure 3a. The minimum σ was found at the smallest λ for all angles-of-attack, α . Generally, σ increased with λ for all α . The rate of increase was fairly constant from the smallest λ up to $\lambda = 0.15$. The rate of increase was less for $0.15 < \lambda < 0.34$. For constant clearance, σ increased with increasing α . Using the α/σ analogy, σ increased with decreasing ϕ .

Rains' cavitation data for the axial-flow pump configuration are shown in Figure 3b. For the design flow coefficient, the minimum σ was between $0.1 < \lambda < 0.3$. Below $\lambda = 0.1$, σ increased with decreasing λ . Similarly, above $\lambda = 0.3$, σ increased with increasing λ . For off-design flow coefficient, the data showed a slight perturbation to the above trend. For constant clearance, σ increased with decreasing ϕ which was the same result found for the stationary blade data. However, the trends of σ with λ for the stationary and rotating configurations were not similar. Rains concluded that rotation strongly affected the tip-wall vortex location and structure.

Rains also compared these data with his analytical model. Using the C_p measured for a stationary blade in Equation 6, he calculated σ at various chordwise stations for the design flow coefficient. He calculated the inception point of $\sigma = 1.05$ at $x/c = 0.4$. For the same parameters, the experimental σ was 0.88. This represents a 20% difference with respect to the experimental value.

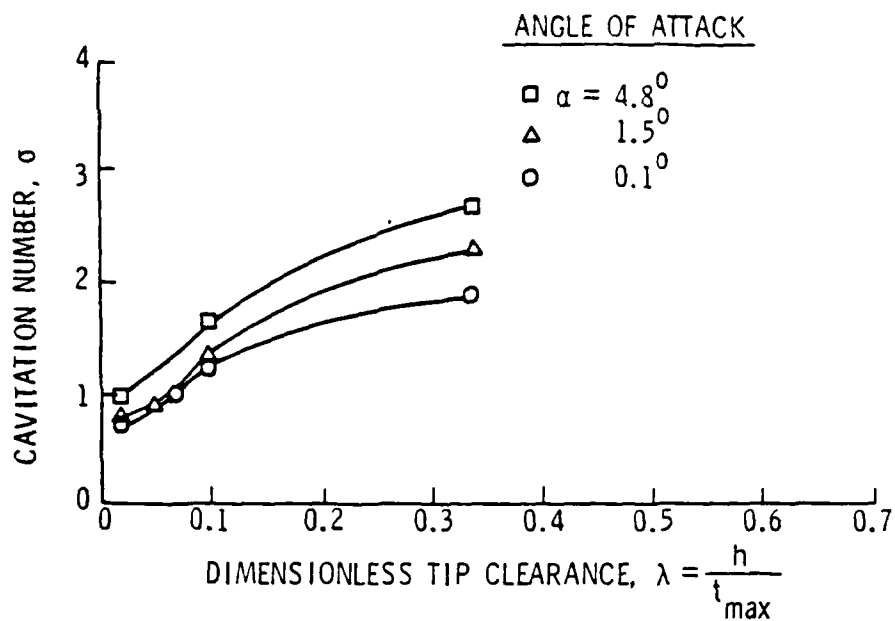


Figure 3a. Rains' Cavitation Data for a Stationary Blade,

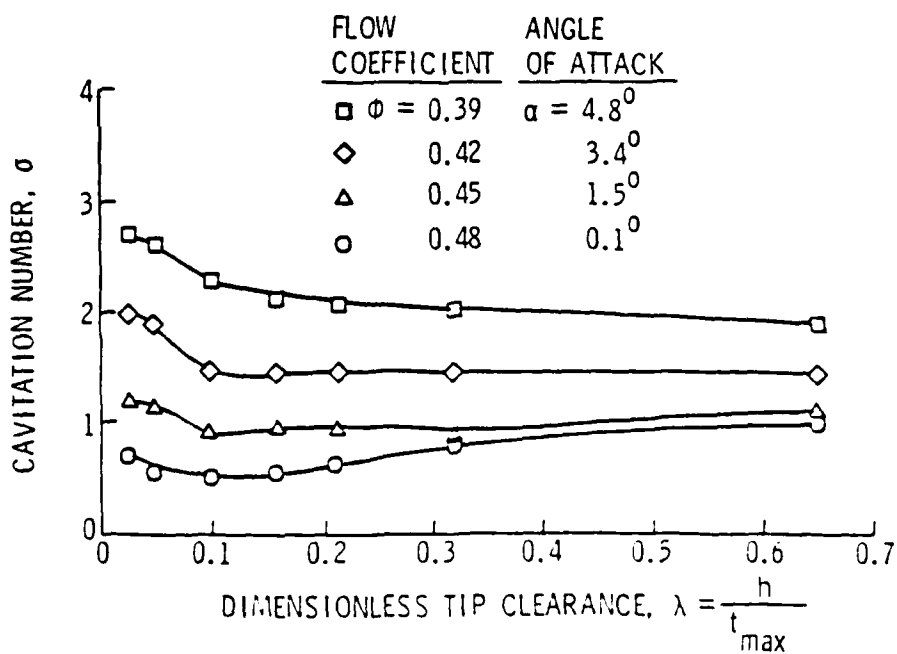


Figure 3b. Rains' Cavitation Data for an Axial-Flow Pump.

2.2.2 Axial-Flow Pump Cavitation Experiments by Mitchell.

Mitchell (8) also studied tip cavitation in axial-flow pumps. Tip cavitation implies that several forms of cavitation occurred in the tip region. These forms included blade surface and tip-wall vortex cavitation. Mitchell's investigation represented a more extensive experimental program than Rains' investigation which was done several years earlier. However, Mitchell did not attempt to develop an analytical model.

Tip cavitation experiments were conducted on a single stage, axial-flow pump in a water tunnel. Mitchell's investigation included the tip clearance, flow coefficient, and rotor RPM as the parameters. In addition, the tip-wall boundary layer was measured for one flow condition, and similar profiles were assumed for the other conditions. However, none of the possible parameters of the boundary layer were later correlated with the cavitation data. Hence, although it was measured, the boundary layer was not a parameter of Mitchell's investigation.

Mitchell's experimental data are shown in Figures 4a, 4b, and 4c as plots of cavitation number versus clearance ratio, σ - λ trends. These trends seemed almost independent of RPM except for a slight decrease in σ for increasing RPM at constant clearance. However, the percent difference in between the high and low RPM conditions was small and might not be greater than the experimental error. For all RPM at the design flow coefficient, the minimum σ was found approximately at $\lambda = 0.1$. Below $\lambda = 0.1$, σ increased with decreasing λ . Above

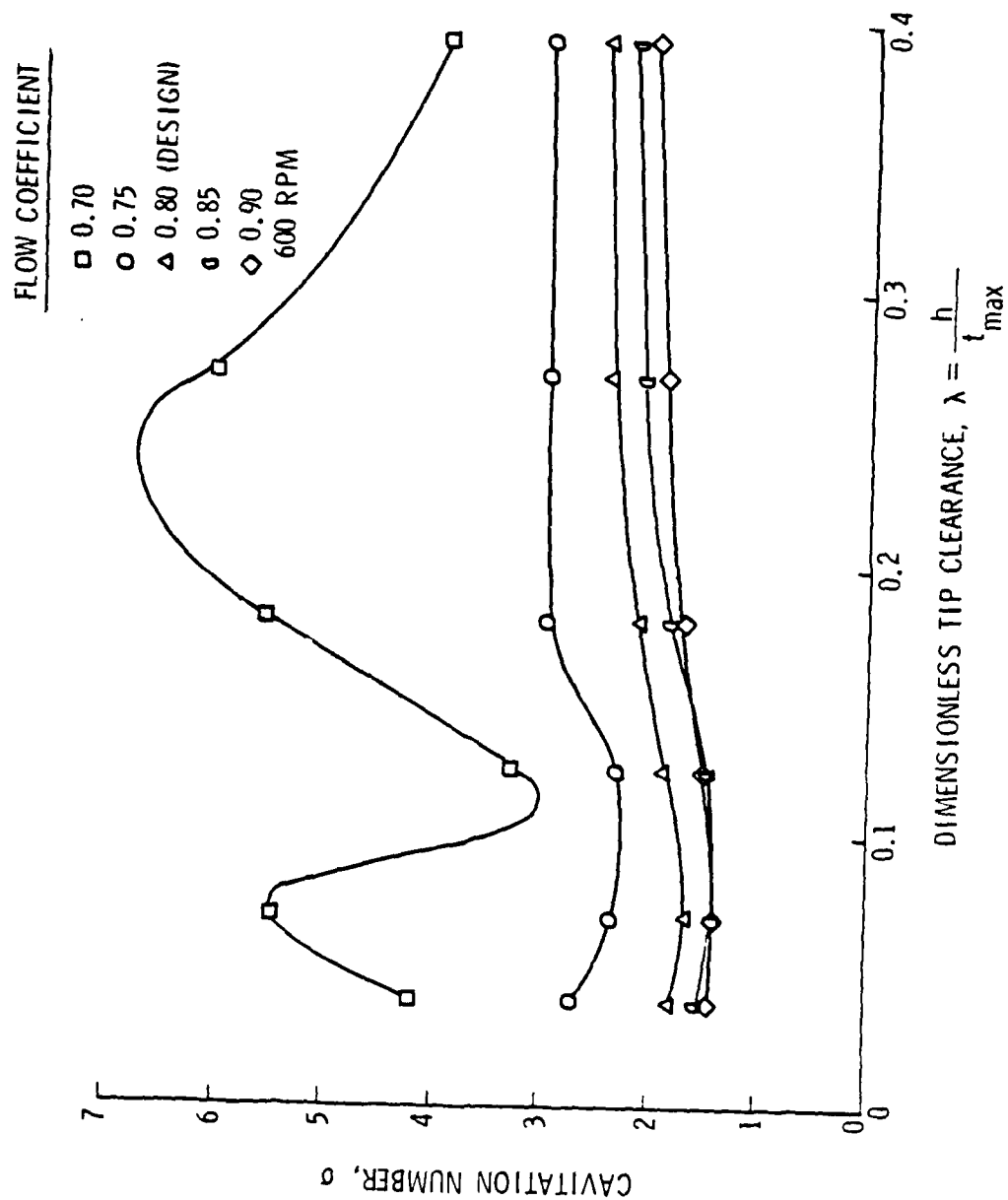


Figure 4a. Mitchell's Cavitation Data for an Axial-Flow Pump at 600 RPM.

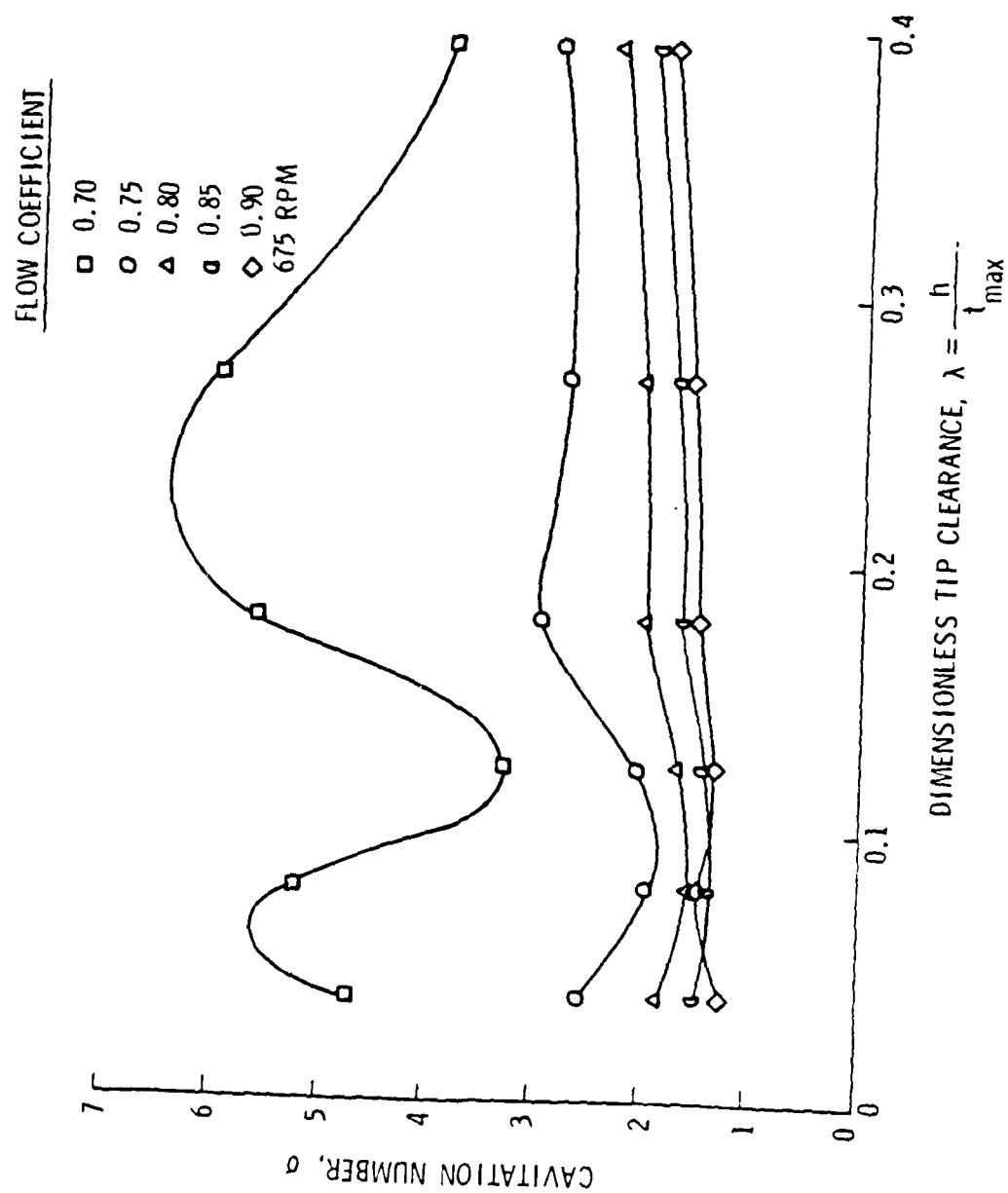


Figure 4b. Mitchell's Cavitation Data for an Axial-Flow Pump at 675 RPM,

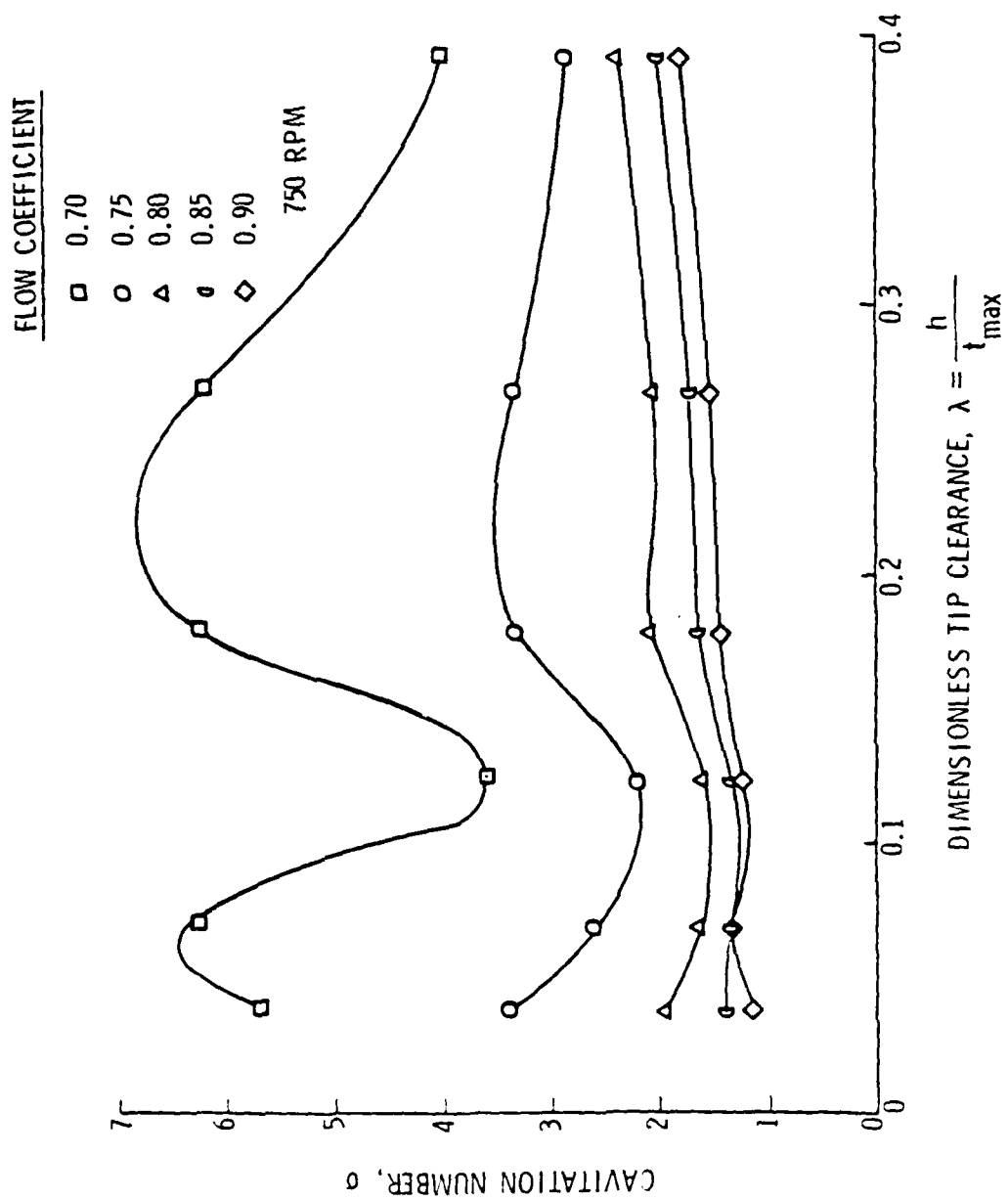


Figure 4c. Mitchell's Cavitation Data for an Axial-Flow Pump at 750 RPM.

$\lambda = 0.1$, σ increased with increasing λ . However, the rate of increase was greater in the range $0.1 < \lambda < 0.2$ than for $\lambda > 0.2$. Also, the rate of increase became negligible as λ approached 0.4 suggesting that σ asymptoted to a maximum value for large clearances. For constant clearance and RPM, σ increased with decreasing ϕ . At the lowest flow coefficient, the trend showed large variations in σ as compared to the design ϕ . Conversely, at the highest flow coefficient, the trend approached a straight, horizontal line.

As a result of these data, Mitchell made several important conclusions. A clearance ratio of 0.1 was found for optimum cavitation performance, and this value was independent of the flow coefficient and rotor rotation. He was not able to explain this result since he expected the minimum cavitation number to depend on a critical Reynolds number, R_e , that would vary with RPM giving a different optimum clearance. However, this trend did not appear in these data. Mitchell made another conclusion concerned with the regimes for surface and vortex cavitation. He observed that for $\lambda < 0.1$ blade surface cavitation was the dominant form, and for $\lambda > 0.1$, tip-wall vortex cavitation was the dominant form. He assumed that strong viscous stresses in the clearance for the $\lambda < 0.1$ case created the blade surface cavitation while for $\lambda > 0.1$ these viscous stresses were weak. Lastly, Mitchell noted that tip cavitation was not completely correlated by the parameters of his investigation. He suggested that a parameter from the tip-wall boundary layer, such as the laminar sublayer, might enter the correlation.

2.2.3 Comments on the Investigations of Rains and Mitchell. The investigations of Rains and Mitchell detailed in the prior sections constitute the majority of the available studies done on tip-wall vortex cavitation. From these investigations, several points deserve particular attention. Some common results were found in the experimental data although the method of determining cavitation differed in both investigations. Both used almost the same parameters and found they could not completely correlate the results. Also, the effect of air content on vortex cavitation was not addressed by either investigation.

The experimental data showed the same general trend in σ with λ . Both observed an optimum λ near 0.1 and showed this optimum to be invariant with flow coefficient. Mitchell found the σ - λ trend also invariant with RPM. This common trend must become a comparison for any future experiments even though the relative magnitudes of σ in the trends were not equal. Although both studies used axial-flow pumps in their experiments, the magnitudes of σ differed by a factor of two for the same clearance ratio. This difference might be explained by the different blade loadings on the tip.

Although similar trends were found, both investigations used different methods for determining the cavitation number. Recalling Equation 1 for the cavitation number, the cavitation pressure, P , was determined at different points in the cavitation development. Rains recorded the water tunnel test section static pressure when cavitation inception occurred. Rains noted that a 10% hysteresis in σ was observed between cavitation inception and desinence. Conversely,

Mitchell recorded the static pressure for cavitation desinence. Using different pressures in the calculation of σ leads to different magnitudes. However, during any experiment, consistency of the method used to determine the cavitation pressure results in the σ - λ trend being invariant of the method.

Another common conclusion of both investigations was that neither completely correlated cavitation number with all the important parameters for tip-wall vortex cavitation. Hence, at least one or more parameters of the tip flow field must enter the correlation before the trends can be explained. Mitchell suggested a parameter from the tip-wall boundary layer. However, Rains accounted for the boundary layer and suggested that bubble dynamic effects in the vortex should be considered.

The effect of the air content on the inception of cavitation was not considered by either investigation. Rains did not record the air content during his experiments, nor did he discuss its effects. Mitchell noted that the air content was kept constant at 16 cubic centimeters per liter in his experiments, but he did not determine its effects on the cavitation performance. Several investigations (9,10) of vortex cavitation showed that air content has a substantial effect on cavitation.

2.3 Vortex Investigations and Development

2.3.1 Trailing Vortex Investigations. A previous section detailed the tip flow field of an axial-flow pump and discussed the parameters

important to the tip-wall vortex. However, the structure of the tip-wall vortex was not discussed, but it must be understood to predict cavitation performance.

Observations of trailing vortices, including tip vortices, of axial-flow pumps indicate that they have a similar structure. Although the mechanisms that form them are different, cavitation still occurs in discrete cores that trail in helical patterns downstream from the blade tip. Hence, knowledge of any trailing vortex structure can be helpful in understanding the tip-wall vortex structure.

In a trailing vortex investigation, Billet (10) mapped the velocity field of the vortex using laser velocimetry. Figure 5 shows the axial and tangential velocities as a function of the radial distance from the center of the vortex. Up to 0.4 inches, the tangential velocity increases linearly and beyond 0.4 inches it decreases as an inverse function of the radial distance. This form of a velocity profile is similar to the inviscid Rankine vortex velocity field. A Rankine vortex has a rotational core and irrotational field outside the core. Therefore, since trailing vortices are similar, the tip-wall vortex is expected to have a Rankine structure.

2.3.2 Rankine Vortex Development. The inviscid Rankine vortex velocity field is shown in Figure 6a as a function of the radial coordinate, r . Included are the relationships for the rotational and irrotational velocity fields. The core radius, a , separates these two fields. The circulation of the vortex, entirely contained within the core, is given as

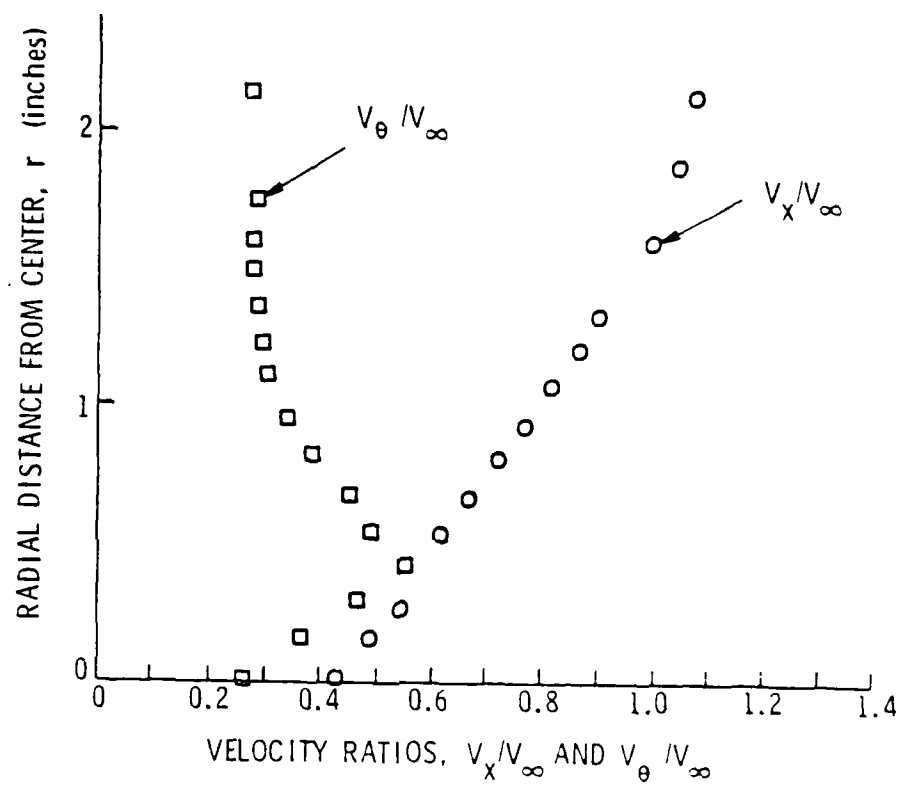


Figure 5. Axial and Tangential Velocity Profiles of a Trailing Vortex.

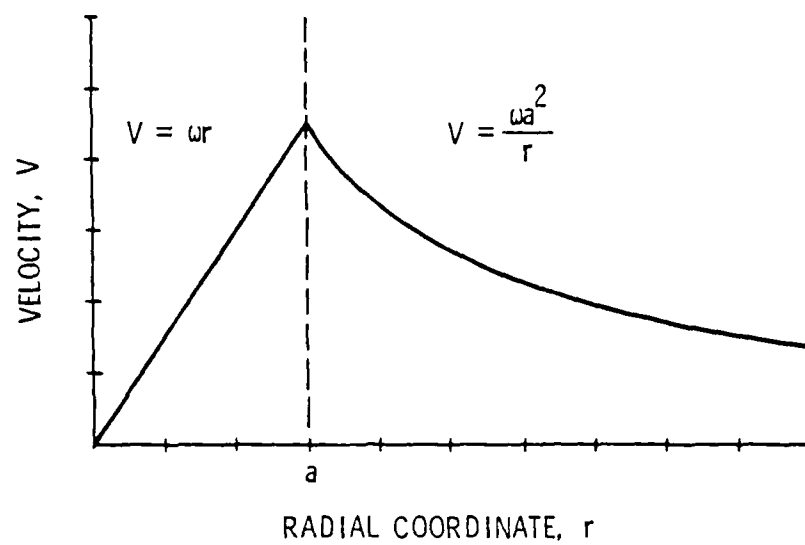


Figure 6a. Rankine Vortex Velocity Field.

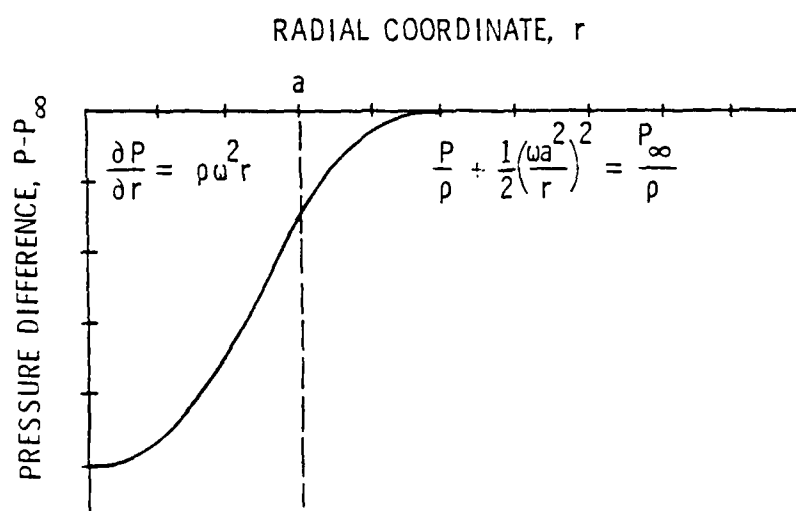


Figure 6b. Rankine Vortex Pressure Field.

$$\Gamma = 2\pi a^2 \omega \quad (7)$$

where ω is the angular velocity of the core. All the vorticity of the tip-wall vortex must be contained in this core, so the circulation in Equation 7 can estimate the magnitude of the leakage vorticity.

The pressure field about a Rankine vortex is shown in Figure 6b. The pressure reaches a minimum at the core center and increases to ambient at a location outside the core. Since incipient cavitation occurs at the point of minimum pressure, the vortex core center will cavitate first if the pressure is approximately equal to the vapor pressure, P_v . Any point in the vortex may cavitate if the pressure there is below P_v .

The pressure coefficient, $C_{p_{\min}}$, for the Rankine vortex is given by

$$C_{p_{\min}} = -2 \left[\frac{\Gamma}{2\pi a V^2} \right]^2 \quad (8)$$

where V is a reference velocity, and Γ is defined in Equation 7. If $C_{p_{\min}}$ is a measure of the cavitation number, Equation 8 can be used as a basis for a model to predict cavitation performance of the tip-wall vortex. If so, the parameters of the model would be the circulation, core radius, and reference velocity. Since the circulation and core radius would be difficult to measure experimentally, they could be found as functions of other parameters such as the clearance, RPM, and tip-wall boundary layer. Therefore, the model of Equation 8 would reduce to a function of these parameters.

CHAPTER III

EXPERIMENTAL PROGRAM

3.1 Experimental Parameters

An objective of this investigation is to conduct tip-wall vortex cavitation experiments. To do so, the parameters of the experiment must be defined. Hence, discussions of the previous investigations and the tip flow field provide the initial assumptions for these parameters and their range.

Based on the foregoing discussions, the parameters for the experimental program included the clearance, RPM, and tip-wall boundary layer. The clearance was included because it gives the σ - λ trend which is not completely understood. This trend is required for comparison with previous data. Similar trends would validate the data and confirm the optimum clearance for cavitation performance.

Although the σ - λ trend was independent of RPM in the previous studies, the RPM was included as a parameter because it provides a Reynolds number variation. In the previous studies the trend in σ with RPM at constant clearance was small. However, whether σ increases or decreases with RPM is uncertain. Varying RPM gives a Reynolds number variation without changing the flow coefficient. Variation of flow coefficient proved to have no effect on the location of optimum clearance. Thus, the present experiment was run at the design flow coefficient for the pump stage.

At least one parameter of the tip-wall boundary layer will enter the correlation of the data. The study of the tip flow field and the suggestions from the previous investigations justify the use of a

boundary-layer parameter. Physically, the tip-wall boundary layer alters the loading on the blade tip that effects the tip-wall vortex. Which parameter of the boundary layer to include is uncertain; therefore, the boundary-layer velocity profiles were measured at each test condition. Later, a parameter can be extracted from the profiles for correlation.

The range of the parameters in the experiment was determined by the previous investigations and mechanical limitations. The σ - λ trend helps to define the range of the clearance. Typically, a clearance should be below, near, and above the expected optimum. The final values of clearance were chosen to be 0.016, 0.035, 0.060, 0.075, 0.091, and 0.100 inches. These correspond to clearance ratios of 0.064, 0.140, 0.240, 0.300, 0.364, and 0.400.

The range of RPM was constrained by the power limit of the drive motor. Three values of RPM were required to show a trend and the values of 502, 669, and 836 RPM were determined.

The range of the boundary-layer parameter was found by calculation. The boundary-layer thickness, δ , was used to quantify the changes in the boundary layer. Unfortunately, δ varies as $V^{-1/5}$, so it does not change significantly with RPM which determines the velocity, V . Therefore, modification of the boundary layer was required to give a larger variation in δ . Simple modification was accomplished by roughening the tip-wall with wire mesh screen. A study by Bechtel (11) showed a linear growth of δ with increasing length of the screen. Bechtel's data are shown in Figure 7. These data were interpolated to determine screen lengths for the present

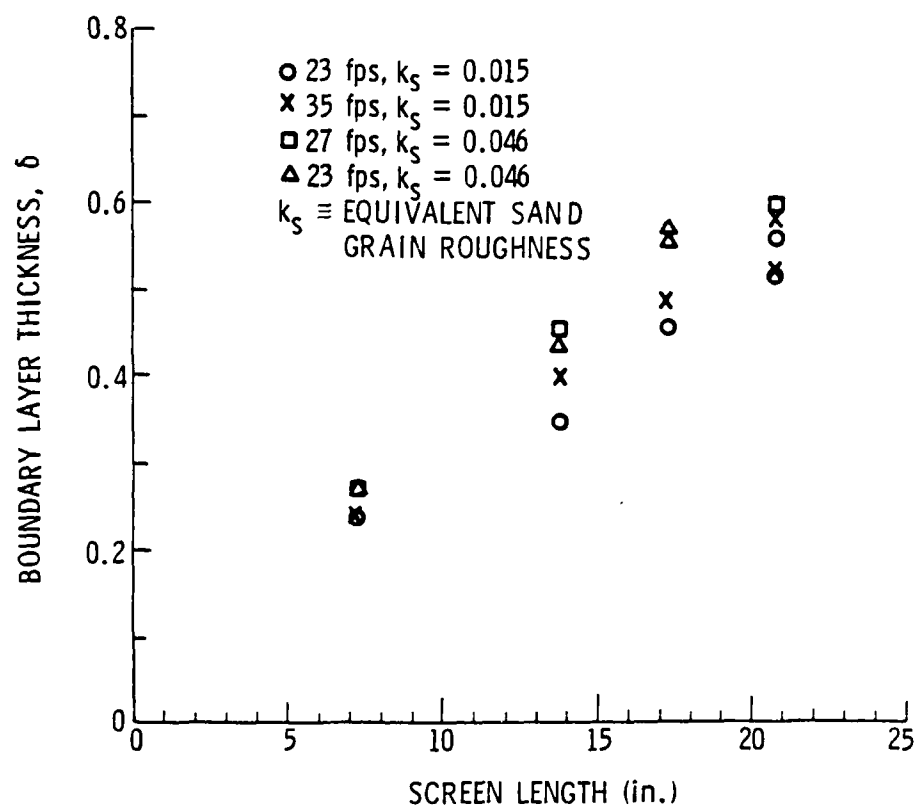


Figure 7. Boundary-Layer Growth with Screen Length.

investigation where three boundary-layer configurations were required to define a trend. The first configuration was with no screen modification. The second used a 4.25-inch length of 0.25-inch mesh screen, and the third used a 8.50-inch length of the same screen.

In addition to the clearance, RPM, and boundary-layer parameters, the air content of the water was recorded periodically. Although the air content was not correlated like the other parameters, it was recorded to document its effects on cavitation and possibly to minimize them.

3.2 Experimental Apparatus

The tip-wall vortex cavitation experiments of the present investigation were conducted in the 12-inch diameter water tunnel at the Garfield Thomas Water Tunnel. Specific details about this facility are given by Lehman (12). The experimental apparatus can be divided into three groups: the apparatus in the water tunnel, the control and measurement equipment, and the laser velocimeter system.

The apparatus in the water tunnel can be subdivided into the pump stage and drive mechanisms. The pump stage was located in the tunnel test section and is illustrated in Figure 8. The major components were the rotor, stator vanes, and liner. The rotor and stator vanes were typical for axial-flow pump stage designs. The liner contour included a smooth juncture with the tunnel wall, a constant clearance across the blade tip chord, and a diffuser angle to prevent separation. To assist clearance change, the liner was made in halves. The upstream half was made of transparent lucite

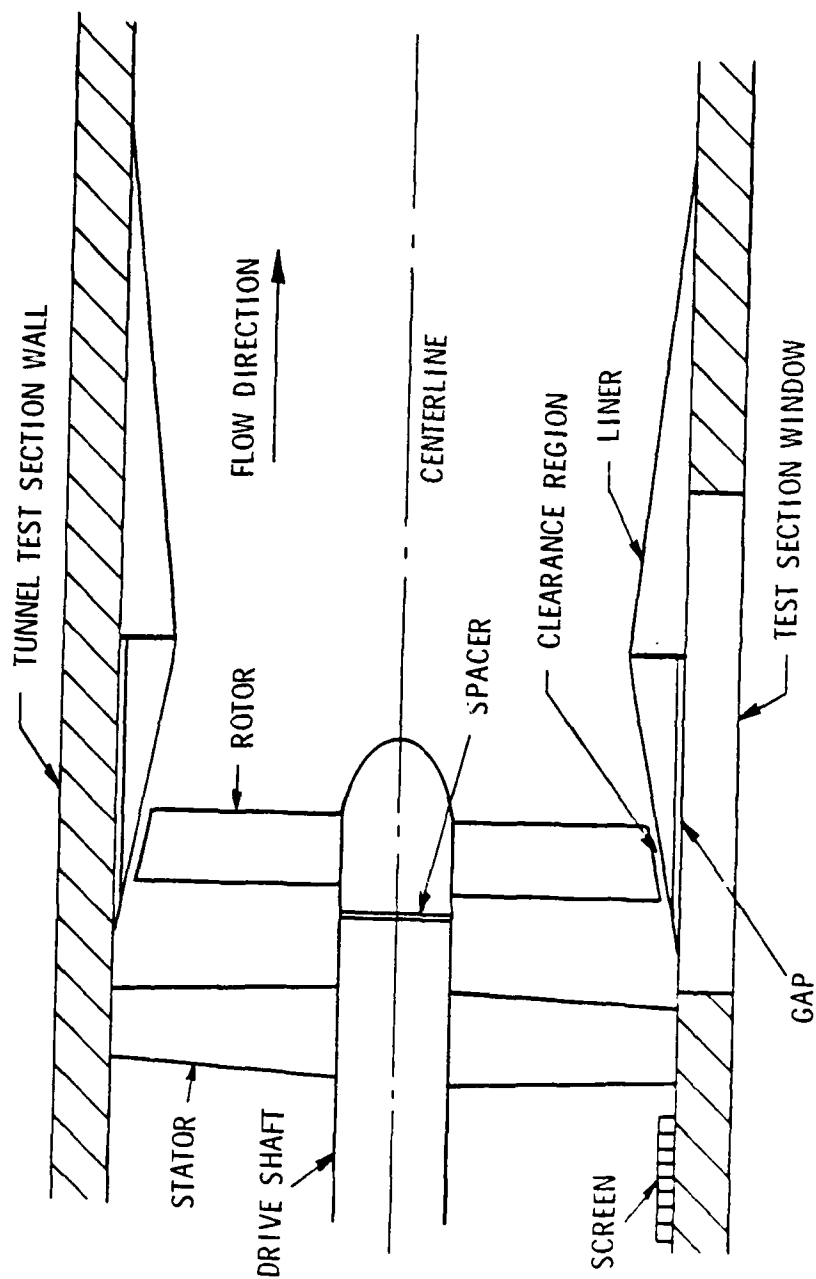


Figure 8. Schematic of Apparatus in Test Section.

for laser beam access. The gap between the liner and the test section window prevented refraction of the laser beam at the interface of the surfaces.

The clearance was adjusted by changing the spacer between the rotor and drive shaft. Each clearance was measured with gauges to verify its value.

The screens for boundary-layer modification were mounted upstream of the stator vanes. Their axial position corresponded to the downstream location for cavitation observation. The screens were mounted with epoxy and screws for ease of removal.

The drive mechanisms consisted of the dynamometer and the drive shaft. The dynamometer encased two 20 Hp electric motors and was mounted in the nozzle of the water tunnel. The drive shaft connected the dynamometer to the rotor.

The control and measurement equipment consisted of the pressure transducers and the water tunnel and dynamometer control panels. The pressure transducers measure the test section static pressure and the mean axial velocity. The transducers and associated electronics were calibrated regularly to avoid drift in the measurements.

The tunnel pressure and velocity were controlled at the water tunnel panel. The tunnel has independent pressure and velocity controls.

The dynamometer panel controlled the voltage-frequency going to the drive motors that regulated the RPM of the rotor. The value of the RPM was found from an encoder mounted on the drive shaft.

The output signal from the shaft encoder drove a display for the RPM and a strobe light for cavitation observation.

The laser velocimeter system measured the velocity components in the test section. Figure 9 shows the system situated near the water tunnel test section. A schematic of the laser velocimeter system is shown in Figure 10. The system had three major components: the laser, the optics, and the processing equipment. The laser and the optics were mounted on a three-axis traversing table. This table located the position of the control volume in the test section. The system operated in a dual beam backscatter mode. In this mode the light scattered from particulate passing through the control volume was collected through the transmitting lens and was focused on a photomultiplier. The counter-processor converted the photomultiplier signal to a digital signal for use in the microcomputer. Also, the counter-processor counted the number of signals and stopped processing after a desired amount was reached. Thus, the sample size was controlled. The microcomputer tabulated the digital output into a histogram from which the mean velocity and local turbulence intensity of the particulate were calculated.

3.3 Experimental Program

The present investigation employed a parametric experimental program. The parameters of the experiment were varied to minimize the time of the program. The order and method for varying the parameters is discussed in this section. Also, a typical test run is defined and discussed.

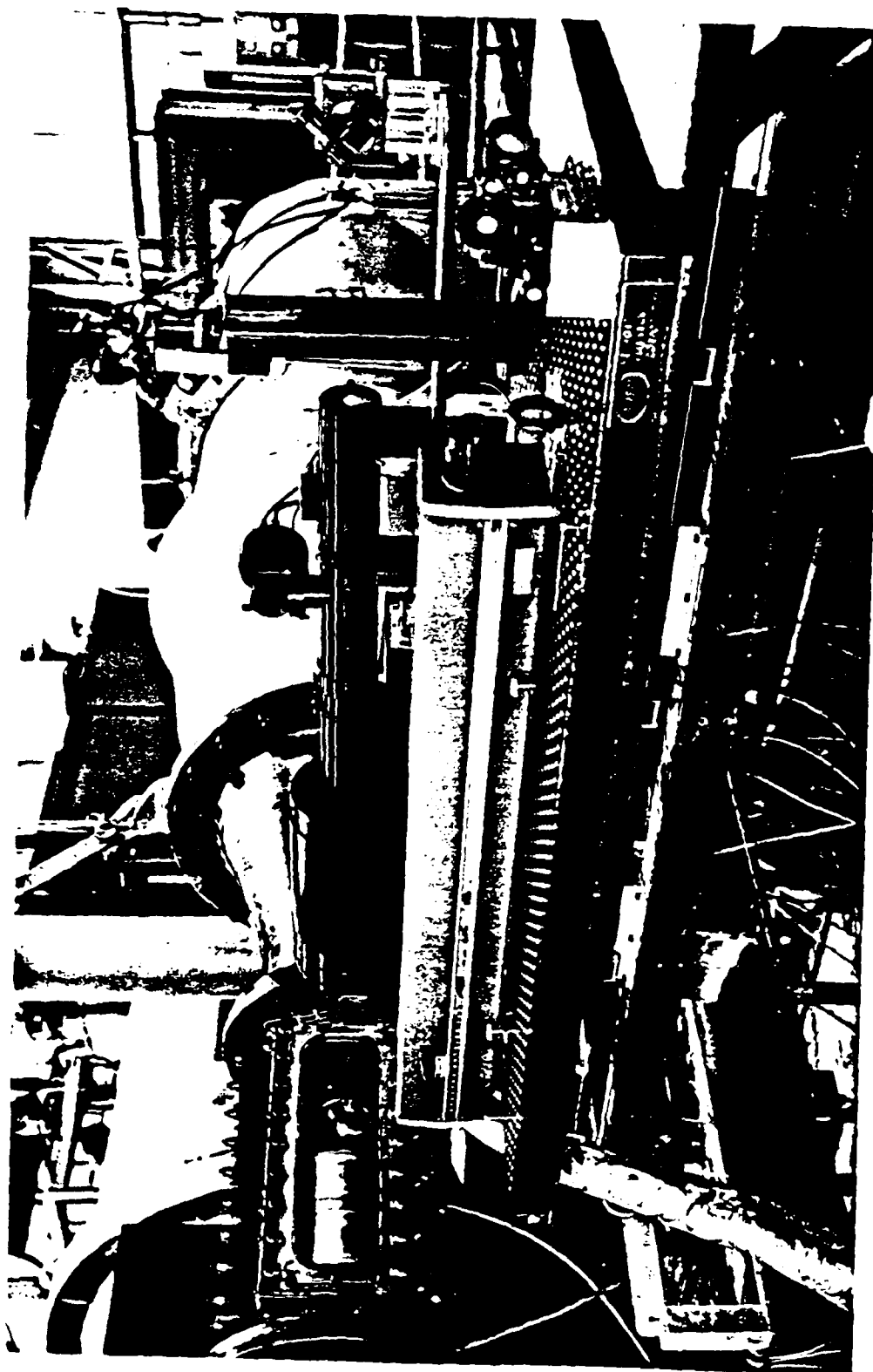


Figure 9. Water Tunnel and Laser System.

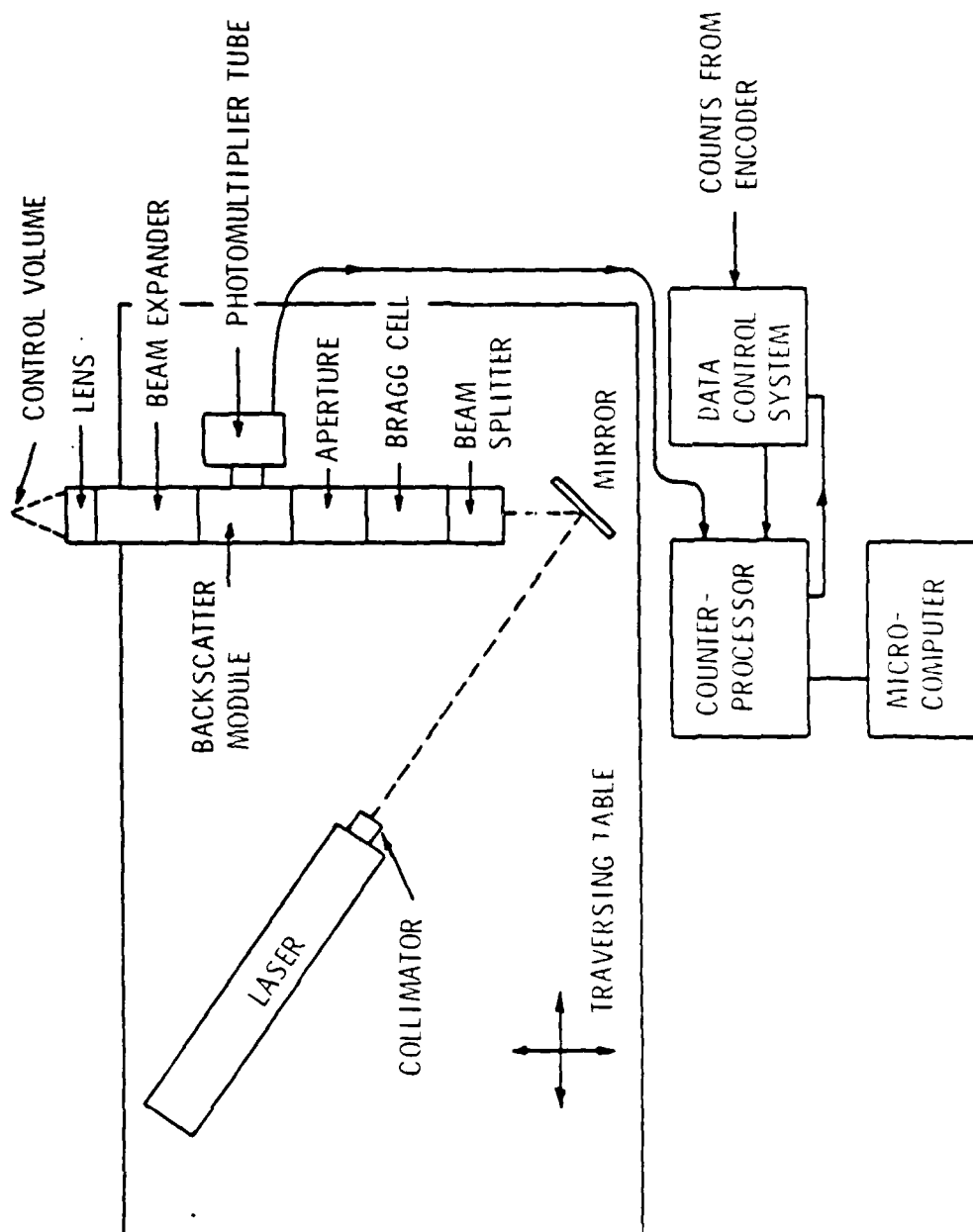


Figure 10. Schematic of Laser Velocimeter System.

For a test run, the RPM was varied often while the tip-wall boundary layer was varied least. The RPM was adjusted at the dynamometer control panel. The clearance was more complicated to change. The procedure involved draining and opening the tunnel, removing the liner, and replacing the spacer at the forward face of the rotor. Modifying the boundary layer involved changing the screen on the tunnel wall. This procedure included changing the clearance plus removing the stator vanes and old screen, mounting the new screen, and reassembling the apparatus.

The cavitation data for one set of parameters established a test run. The procedure for one test run began with setting the clearance and boundary-layer configuration. With the tunnel filled, the rotor RPM was set. Next, the operator at the tunnel control panel lowered the tunnel pressure. Throughout the program the operator attempted to keep the rate of pressure decrease and increase constant. An observer at the test section window observed cavitation inception on the desired blade using the strobe light synchronized with the shaft encoder. The pressure was held constant once fully developed, tip-wall vortex cavitation was observed. Next, the operator slowly raised the tunnel pressure. As the pressure increased, the vortex cavitation flashed which is a condition where the cavitating vortex is seen only intermittently. Cavitation desinence was defined in this investigation as the state when no cavitating vortex was observed for five seconds. At this state the test section static pressure and velocity were recorded. Also, the atmospheric pressure and water temperature were recorded. This procedure was repeated for the same parameters, and

the average cavitation number for the repeated runs was used as the experimental value.

Along with the aforementioned procedure, the tip-wall boundary layer was measured for the three screen configurations at three RPM. Thus, nine boundary-layer velocity profiles were recorded. These measurements were taken at a location 0.5-inches upstream of the clearance. However, this does not infer that the boundary layer has no effect on the σ - λ trend, rather that the boundary layer does not vary significantly with clearance.

As mentioned previously, the air content was measured periodically during the program. A Van Slyke manometer measured the air content in moles of air per million moles of water (ppm). During the program, the air content was kept in the range between 5 and 7 ppm. If the air content fell below 5 ppm, higher air content water was mixed with the tunnel water until the proper range was obtained. If the air content was above 7 ppm, the tunnel water was passed through the degasser.

3.4 Experimental Flow Visualization Technique

Flow visualization was performed to aid the understanding of the flow field. In the present experimental program, an oil-paint film technique was used as the method of visualization. This technique utilized an oil-paint mixture to form a film that shows a pattern on the rotor blades. The procedure of this technique was relatively simple and it has several advantages and some disadvantages.

The procedure began with mixing an oil-base paint with a heavy weight oil. The paint was mixed with oil to improve its consistency

and increase its viscosity. Also, using oil-base paint prevented any diffusion of the paint into the tunnel water. Next, the mixture was applied to the rotor blade leading edge from root to tip and along the chord at the tip. With the tunnel filled and at a pressure greater than atmospheric, the rotor was brought to the desired RPM, held there for approximately 20 seconds, and stopped. While rotating, the flow about the blade carried the mixture downstream along the blade surfaces forming lines similar to streamlines. However, because the mixture has mass, these lines might more closely resemble streaklines. After the rotor was stopped, it was removed from the tunnel and photographed.

The oil-paint film technique for flow visualization has several advantages in addition to its simple procedure. For one, it diagnoses the flow over the blade surface. Separated regions, transition, radial flow, and tip leakage are observed from the streakline pattern. Also, this pattern can be preserved permanently on a photograph.

Several disadvantages exist with the oil-paint film technique. First, the mixture moves across the blade at different speeds because the rotor velocity starts from rest, reaches a maximum, and then decreases. Thus, the streakline pattern is a time-history of the rotor velocity, and the pattern is not that at the one RPM. Another disadvantage of this technique is that the blade passage flow is not visualized. Only inferences of how the pattern on the blade is effected by the passage flow can be made.

Lastly, the mixture of paint and oil is critical. The mixture viscosity must be greater than the water viscosity to minimize the

effect the mixture has on the blade surface boundary layer. Kuiper (13) found that the ratio of fluid viscosity to mixture viscosity should be much less than unity. In this case the mixture velocity during rotation was low, and the boundary layer would remain unaffected by the mixture.

CHAPTER IV

EXPERIMENTAL DATA

4.1 Velocity Profiles

The experimental program included laser velocimetry measurements. The tip-wall boundary layer was measured for the three boundary-layer configurations at three RPM yielding nine velocity profiles. In addition, the axial and tangential velocity profiles were measured from root to tip in between the stator and rotor. All the boundary-layer profiles were measured in a plane just upstream of the rotor.

For the tip-wall boundary layers, the configurations are labeled 1, 2, and 3 corresponding to the case with no screen, 4.25 inches of screen, and 8.50 inches of screen, respectively. The nine velocity profiles are shown in Figures 11a, 11b, and 11c where each figure corresponds to one configuration. For a given configuration, the profiles are similar indicating little change with RPM. All profiles are turbulent and similar to a $1/5$ th power law profile. Also, the boundary-layer thickness increases with configuration number which indicates that the screen caused the increase in thickness. However, the general shape of the profiles did not change with screen modification.

Since the velocity profiles are known in discrete form and the thickness, δ , is known, the integral properties: displacement thickness, δ^* , momentum thickness, θ , and the shape factor, H , can be calculated. Table 1 lists δ , δ^* , θ , and H for the nine profiles. Boundary-layer thickness increases with screen length by even increments and, hence,

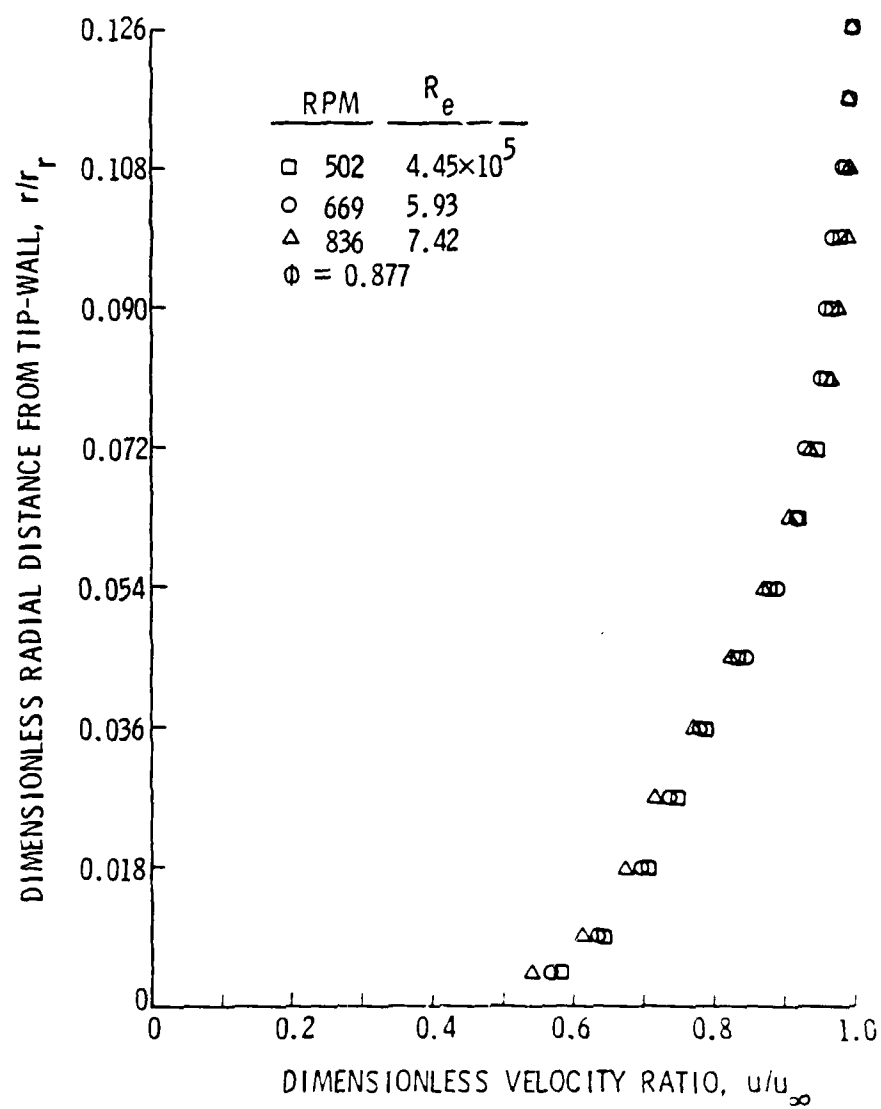


Figure 11a. Boundary-Layer Profiles for Configuration 1.

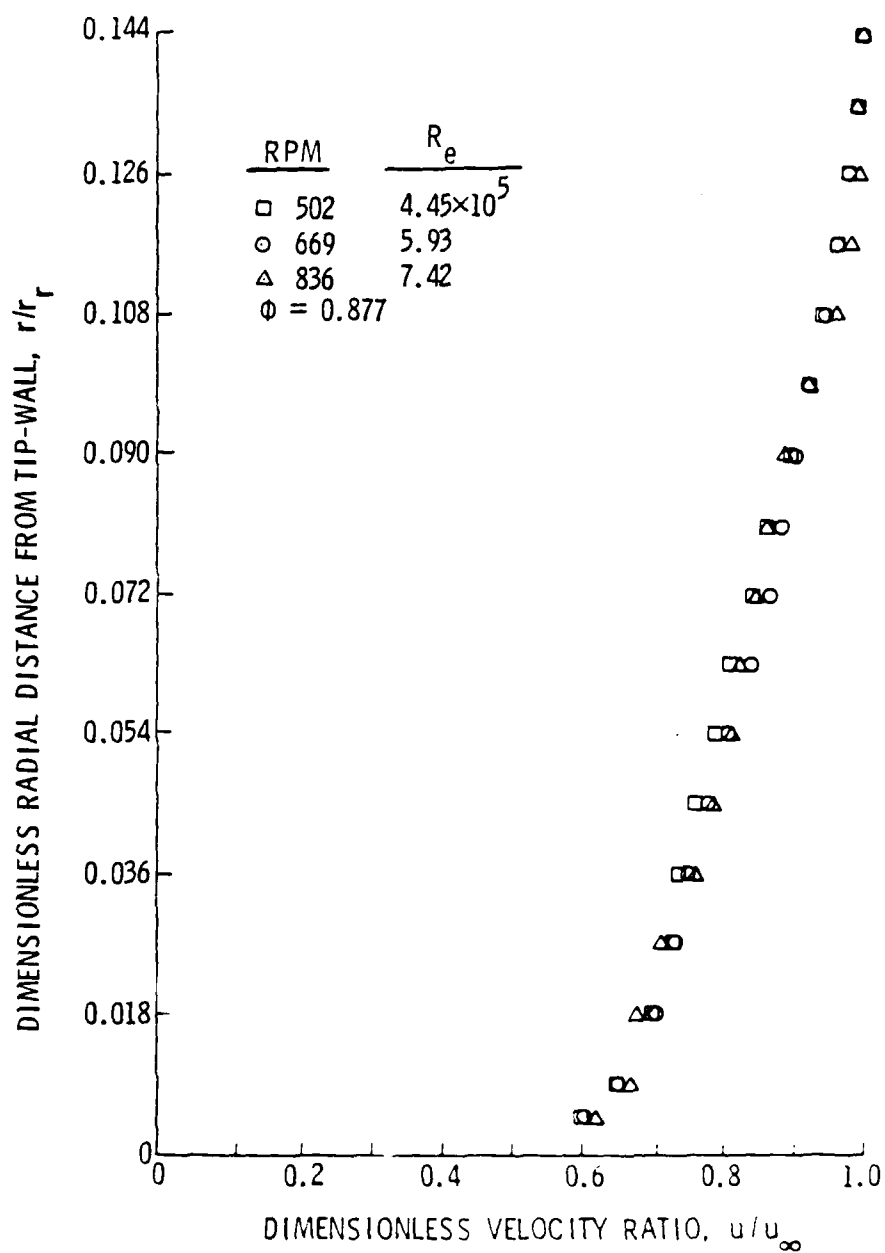


Figure 11b. Boundary-Layer Profiles for Configuration 2.

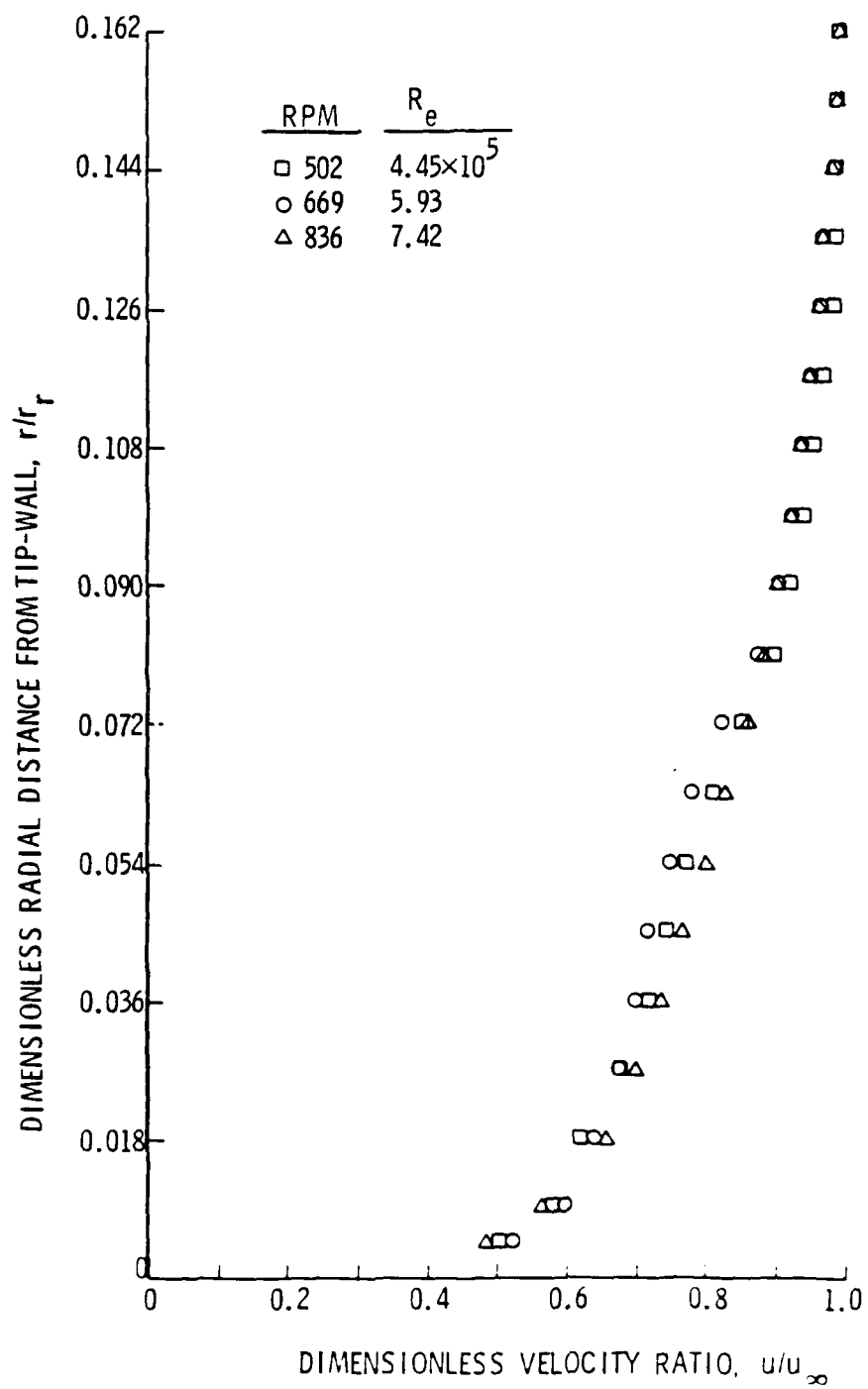


Figure 11c. Boundary-Layer Profiles for Configuration 3.

TABLE I

TIP-WALL BOUNDARY-LAYER INTEGRAL PROPERTIES

<u>Configuration</u>	<u>RPM</u>	<u>δ/r_r</u>	<u>δ^*/δ</u>	<u>θ/δ</u>	<u>H</u>
1	502	.1260	.1461	.0931	1.569
1	669	.1260	.1503	.0963	1.560
1	836	.1260	.1537	.0959	1.604
2	502	.1440	.1760	.1188	1.482
2	669	.1440	.1695	.1144	1.482
2	836	.1440	.1693	.1138	1.487
3	502	.1620	.1638	.1047	1.565
3	669	.1620	.1766	.1141	1.547
3	826	.1620	.1629	.1067	1.527

is a linear variation which is expected given Bechtel's results. δ is an order of magnitude greater than the clearances used in the tests. Therefore, the axial velocities entering the clearance are significantly less than the boundary-layer edge velocity.

For the integral properties, Table 1 shows the δ^* and θ increase with δ as expected for similar profiles. However, H for configuration 2 is lower than H for configurations 1 and 3. A lower shape factor indicates a fuller profile and higher velocities in the clearance.

In addition to the tip-wall boundary-layer velocity profiles, the axial and tangential velocities were measured. These profiles are shown in Figures 12a and 12b. The axial velocity is fairly constant from root to tip. The boundary-layer deficit at the root is much greater than that at the tip. This is accounted for by the high tangential velocity at the root that decreases linearly to a minimum tangential velocity at the tip. Higher turning is given at the root because of design loading. At the tip, the axial and tangential velocities indicate 10 degrees of turning of the flow by the stator vanes. From root to tip, the stator vanes turn the flow in a direction opposite to the rotor rotation; therefore, the tangential velocities are negative as shown in Figure 12b.

4.2 Cavitation Data

4.2.1 The σ - λ Trend. Cavitation data were obtained as a function of the clearance, rotor RPM, and tip-wall boundary-layer configuration. The variation of desinent cavitation number with clearance, the σ - λ trend, is presented and discussed in this section.

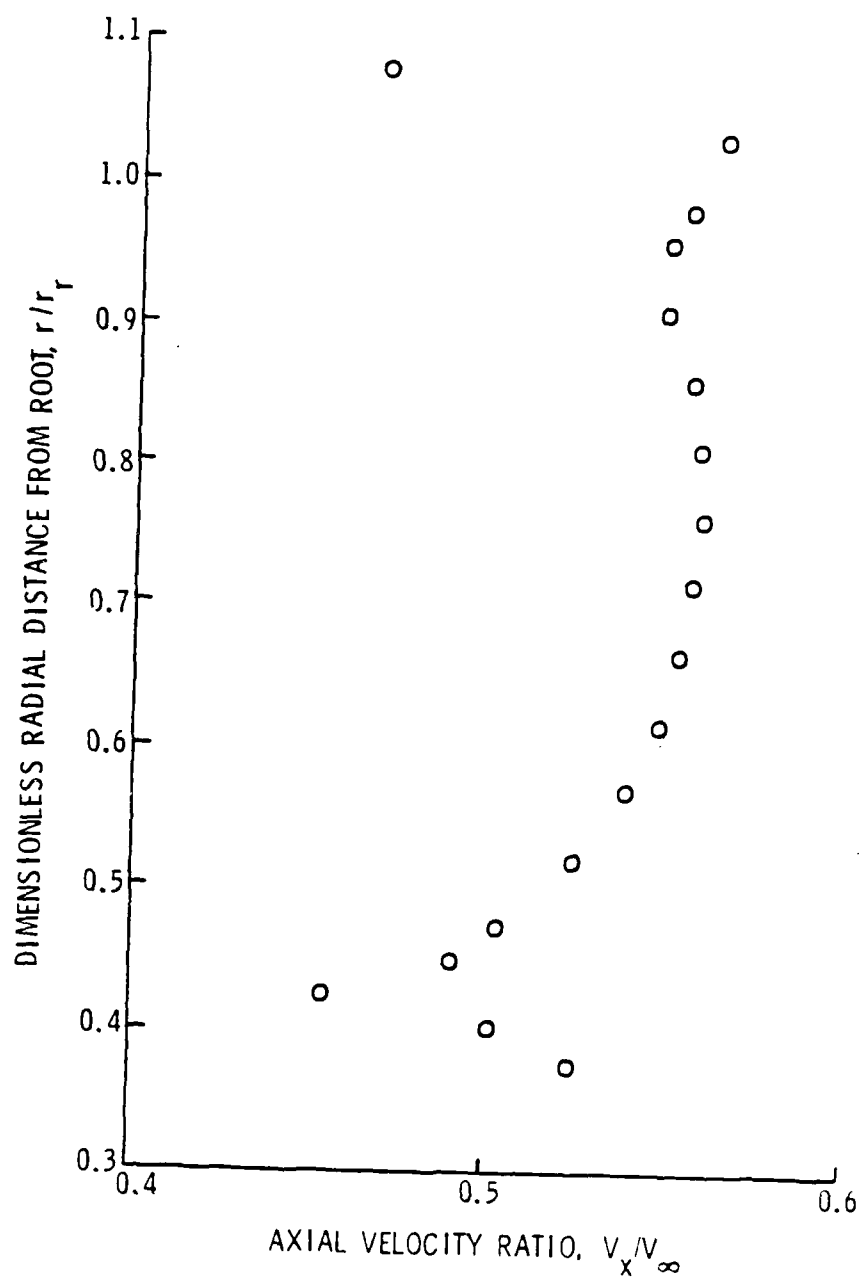


Figure 12a. Axial Velocity Profile Entering the Rotor.

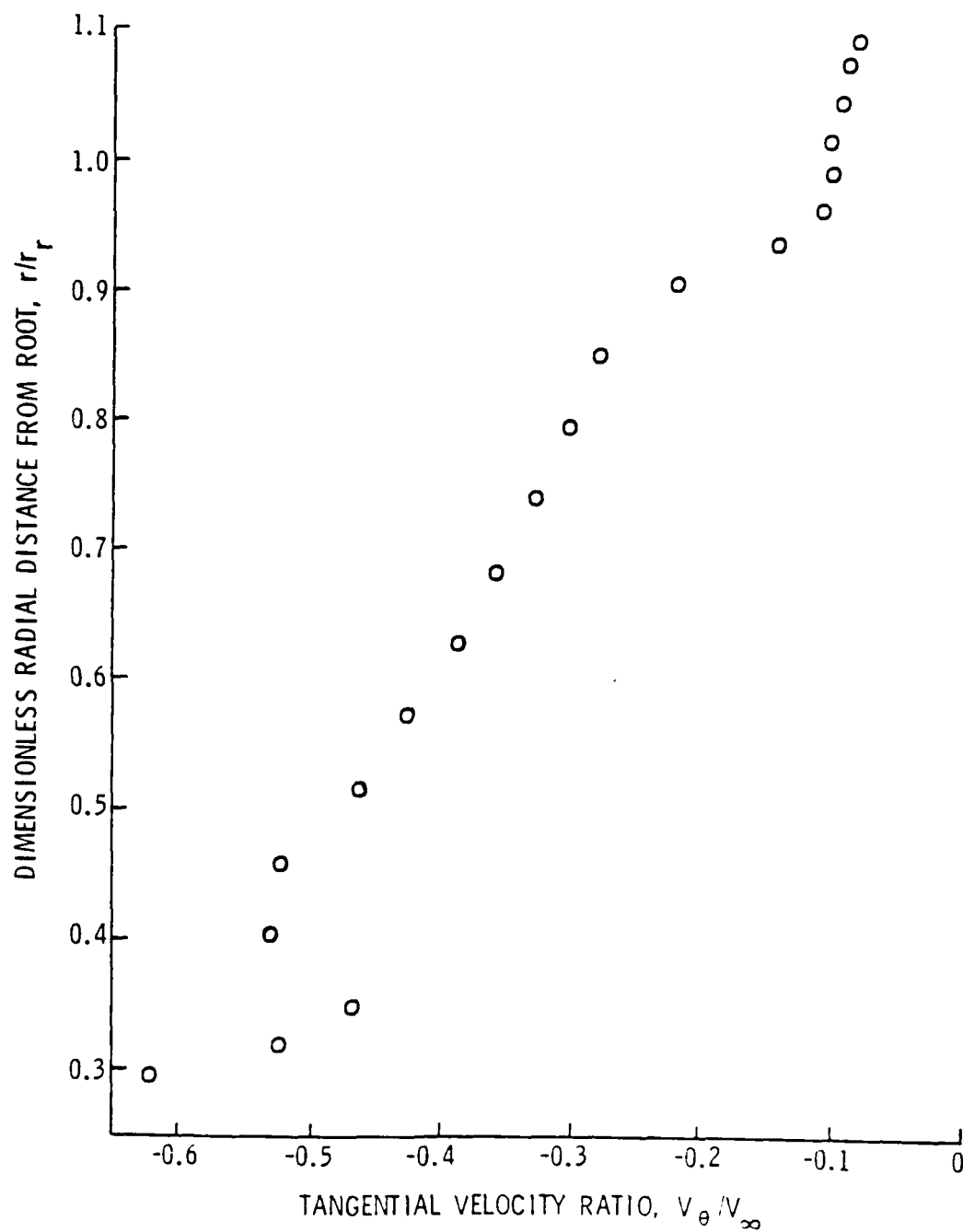


Figure 12b. Tangential Velocity Profile Entering the Rotor.

Typically, trends in cavitation number with any one parameter are found by plotting cavitation number versus this parameter while keeping the other parameters constant. Early analysis of the data found significant air content effects that are also discussed. Lastly, these data are compared with previous tip-wall vortex cavitation data.

Cavitation data are shown in Figures 13a, 13b, and 13c. For boundary-layer configurations 1 and 3, the desinent cavitation index, σ_d , increases with decreasing RPM for constant clearance and flow coefficient. Large intervals in σ_d exist between lines of constant RPM. This trend indicates a strong air content influence on σ_d since previous studies showed that σ_d increased with RPM at constant clearance. Only configuration 2 failed to show a significant air content effect.

Since air content effects were detected during the experimental program, a test was devised to determine the magnitude of their effect. The test involved determining σ_d for three air contents, 2, 7, and 11 ppm, at three RPM for constant clearance and boundary-layer configuration. The results of this test are shown in Figure 14a. For lines of constant air content, σ_d decreases with increasing RPM. As expected, for constant RPM, σ_d increases with air content. A minimum σ_d would be found by either increasing RPM to very large values or decreasing air content to zero. However, neither case is practical. An estimation of the minimum σ_d is found if the data are plotted as σ_d versus air content as shown in Figure 14b. The minimum σ_d is found by extrapolating the lines of constant RPM to the σ_d axis.

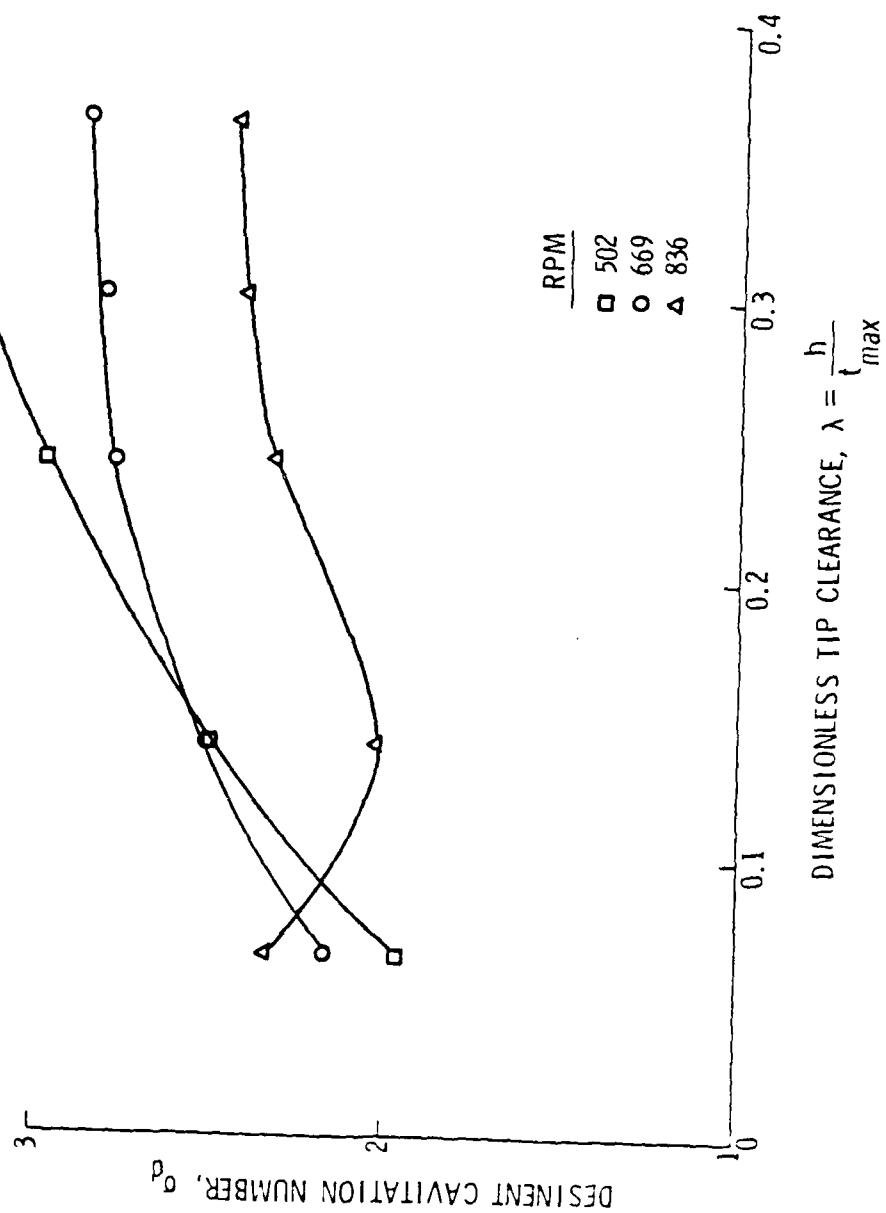


Figure 13a. Cavitation Desinence Data for Configuration 1 with Air Content Effects.

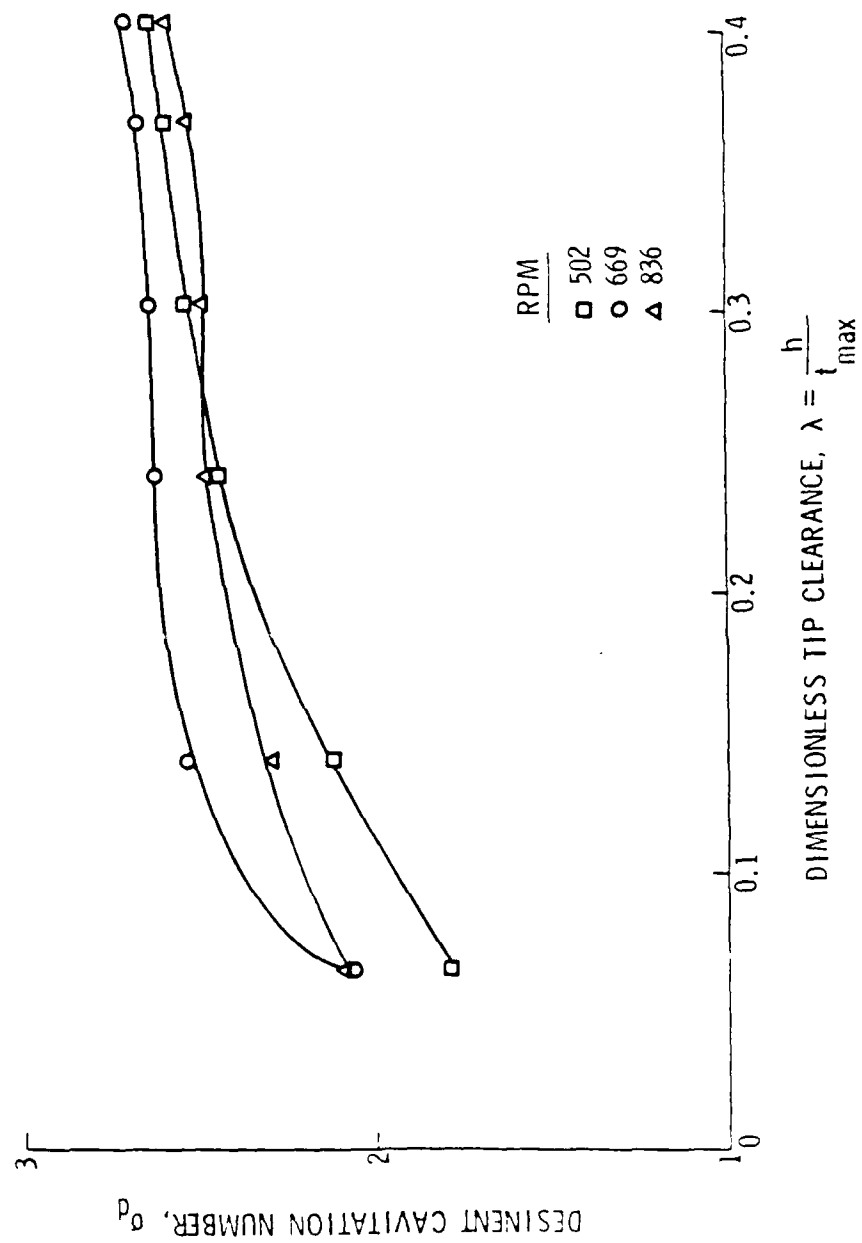


Figure 13b. Cavitation Desinence Data for Configuration 2 with Air Content Effects.

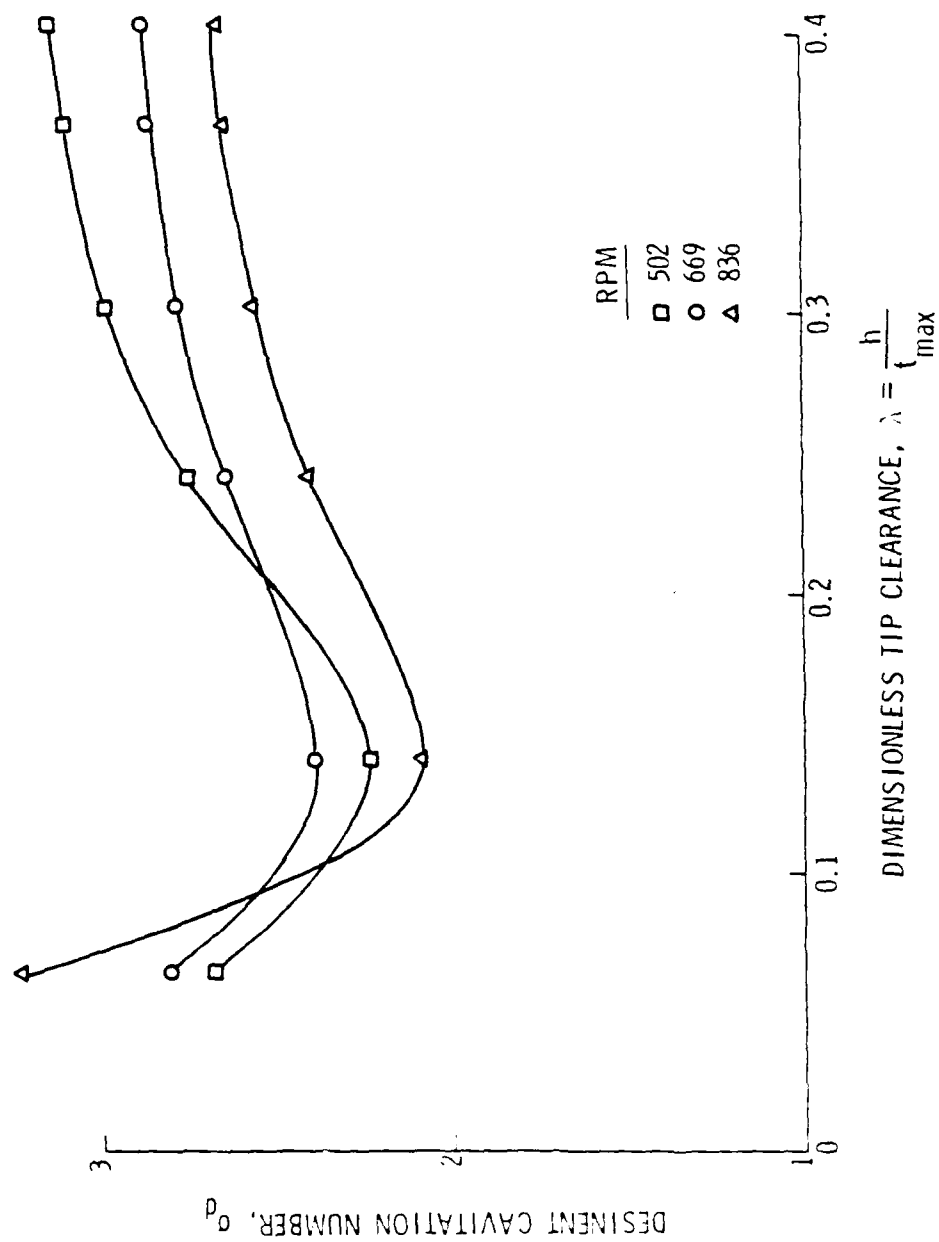


Figure 13c. Cavitation Desinence Data for Configuration 3 with Air Content Effects.

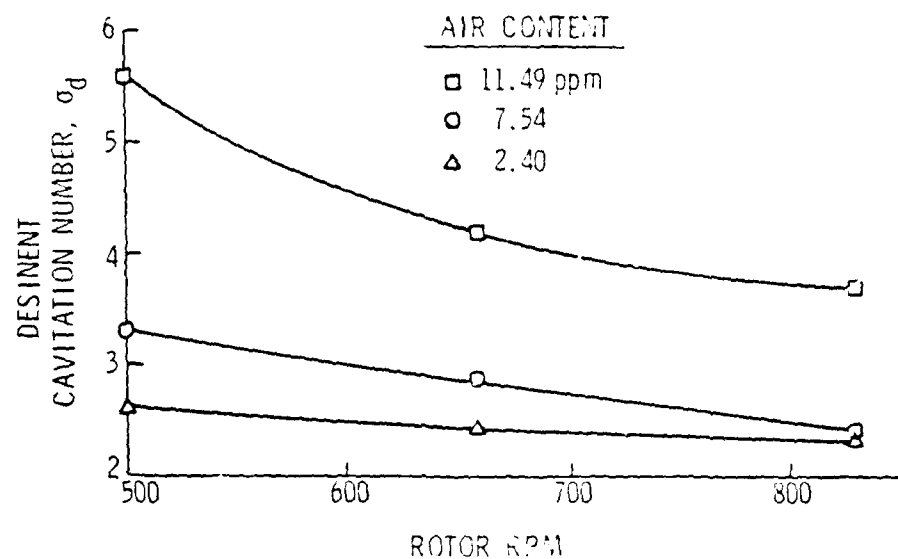


Figure 14a. Cavitation Desinence Data for Varying RPM from Air Content Test.

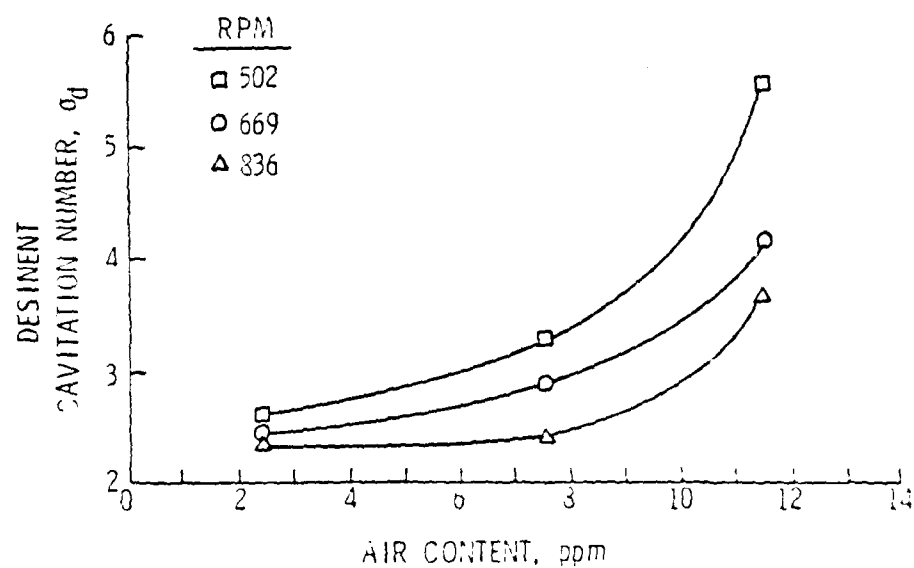


Figure 14b. Cavitation Desinence Data for Varying Air Content from Air Content Test.

The minimum σ_d is estimated as the σ_d intercept and is valid for all air content. Cavitation data are corrected by subtracting the increment, $\Delta\sigma_d$, where

$$\Delta\sigma_d = \sigma_{d_{ACT}} - \sigma_{d_{MIN}} \quad (9)$$

$\sigma_{d_{ACT}}$ is the σ_d for a specific air content from Figure 14b. Ideally, the corrected σ_d have no air content effects. These corrected data are shown in Figures 15a, 15b, and 15c.

Several observations concerning the corrected data require discussion. The value of the clearance for optimum cavitation performance is not consistent for all data. Also, the slopes of the constant RPM lines vary among the boundary-layer configurations as well as within each configuration.

Figures 15a, 15b, and 15c indicate two different trends for the optimum clearance when $\lambda < 0.15$. The cavitation number either increases or decreases for clearances less than $\lambda = 0.15$ depending on the form of cavitation observed. If vortex cavitation is observed for $\lambda = 0.064$, σ_d is lower there than at $\lambda = 0.14$, and the optimum clearance occurs at $\lambda = 0.064$. However, if gap cavitation in the clearance is observed for $\lambda = 0.064$, σ_d is higher than at $\lambda = 0.14$, and the optimum clearance occurs at $\lambda = 0.14$. Typically, the highest RPM conditions exhibit gap cavitation for all boundary-layer configurations. All RPM conditions for configuration 3 exhibit gap cavitation. The 502 and 669 RPM conditions for configuration 1 and 2 exhibit only tip-wall vortex cavitation.

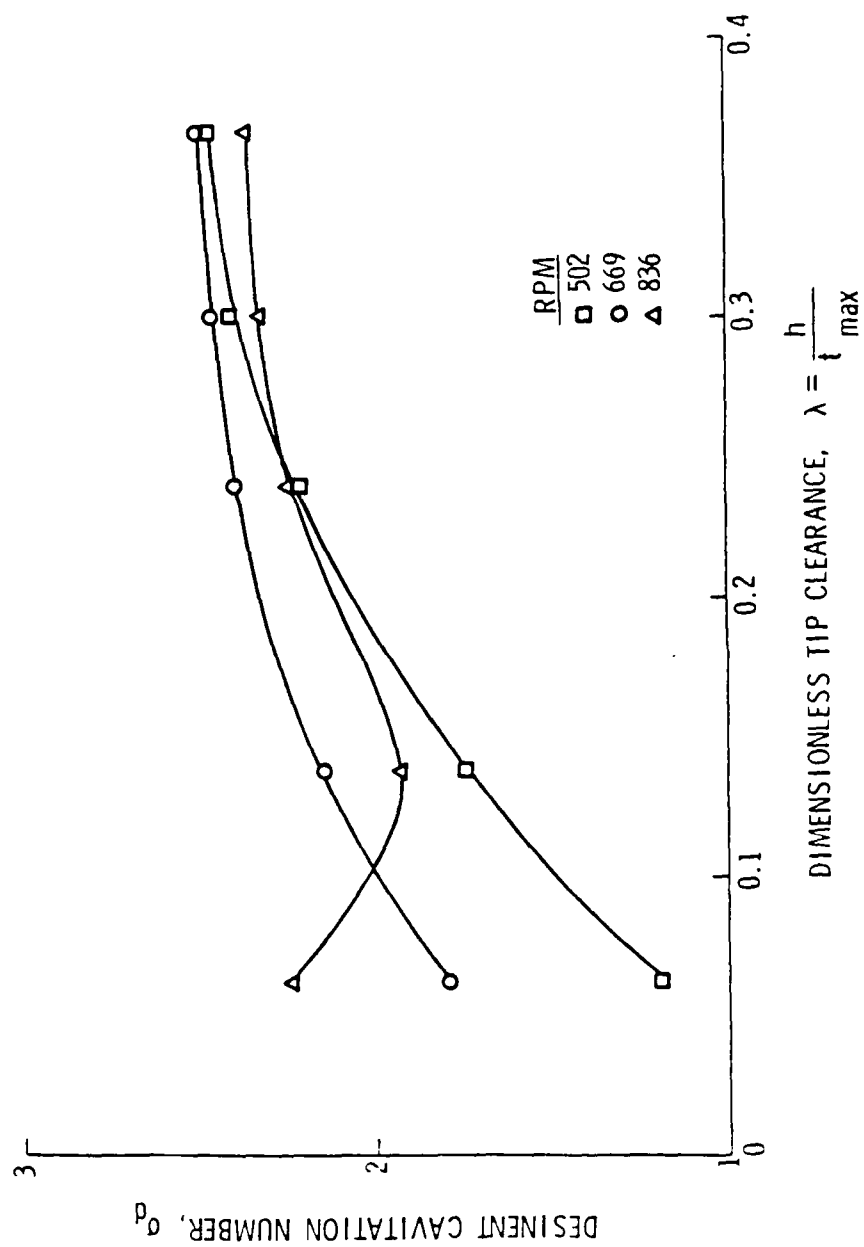


Figure 15a. Cavitation Desinence Data for Configuration 1 Corrected for Air Content.

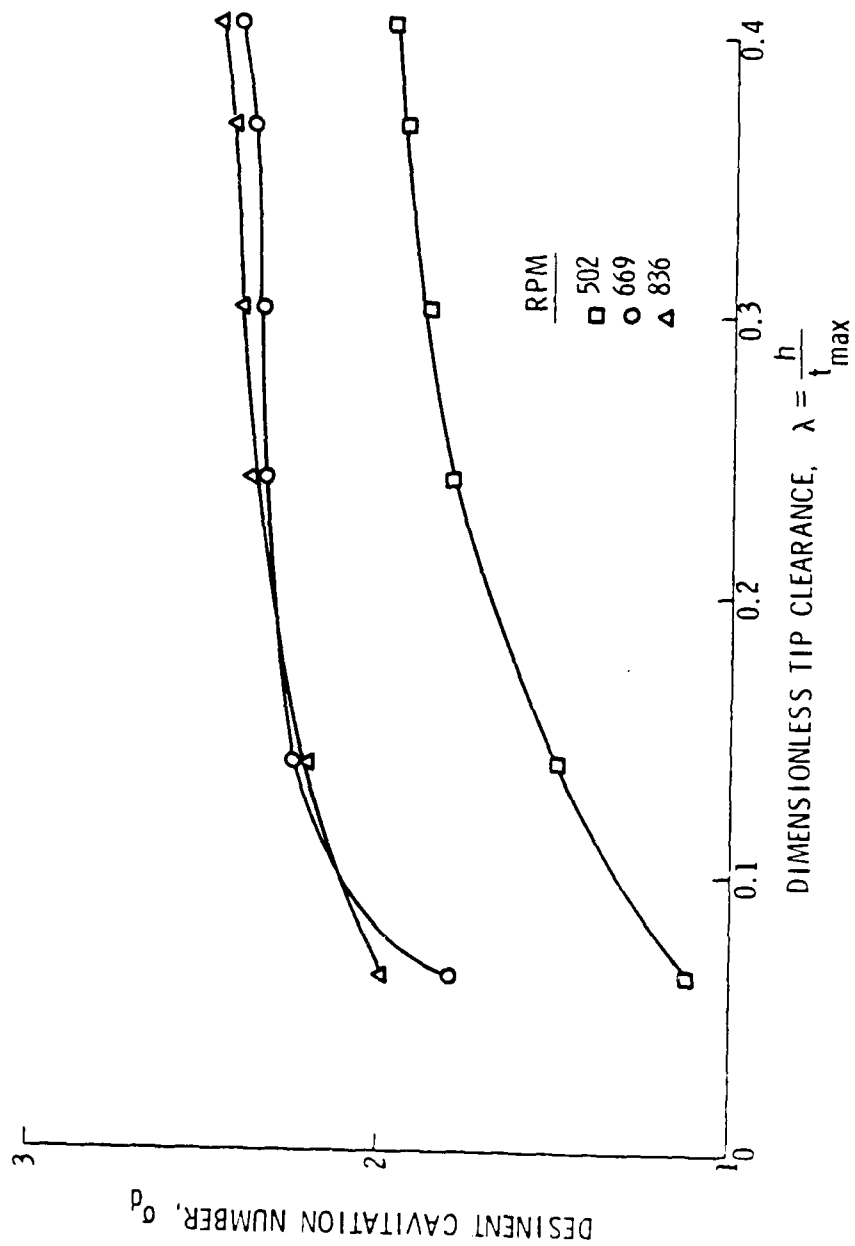


Figure 15b. Cavitation Desinence Data for Configuration 2 Corrected for Air Content.

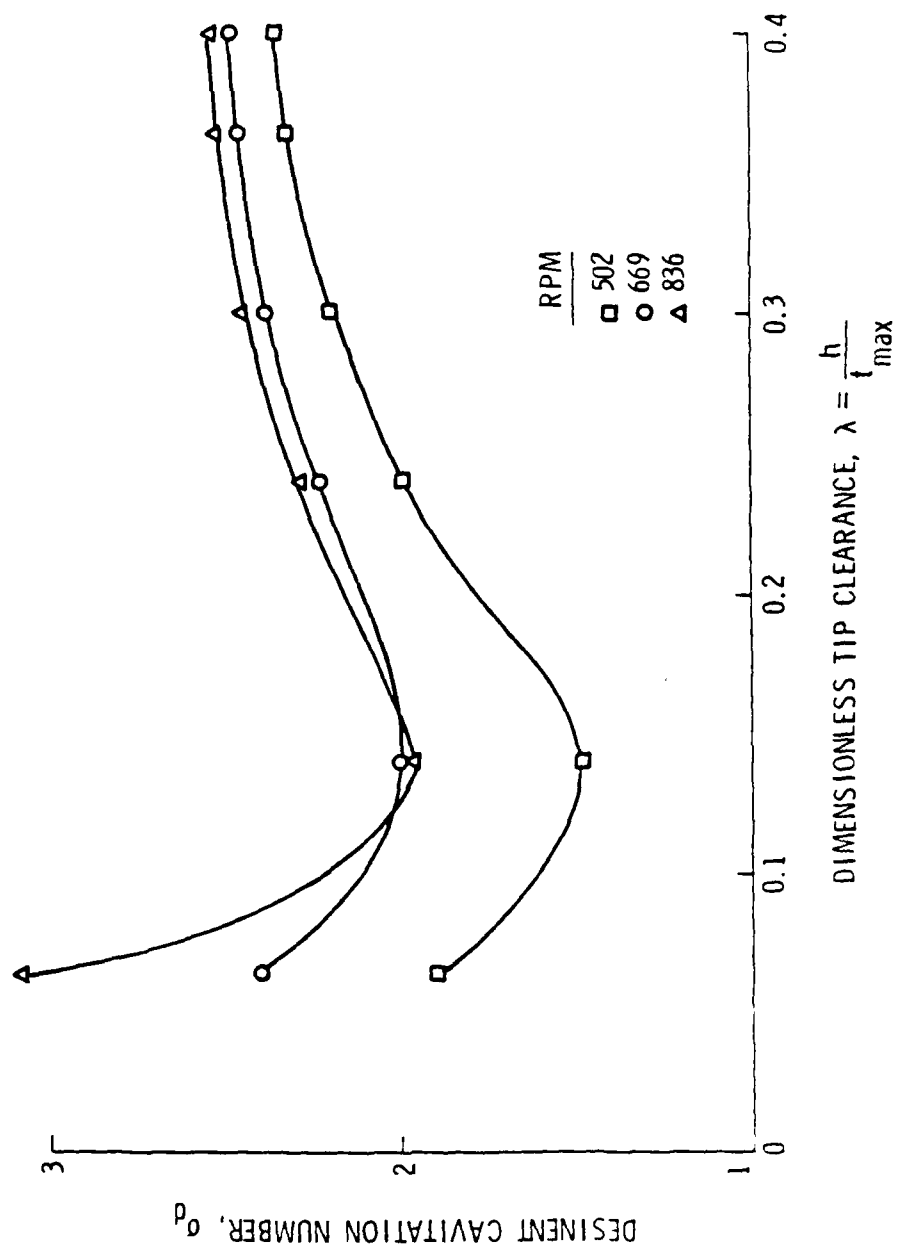


Figure 15c. Cavitation Desinence Data for Configuration 3 Corrected for Air Content.

Recall that the region $\lambda < 0.1$ was expected to have strong viscous stresses in the clearance. Therefore, the form of cavitation that occurs must depend on a critical velocity in the clearance. If the critical velocity is high, as would occur for high RPM, a separation of the flow from the tip surface might occur that could lead to gap cavitation. However, if the critical velocity is low, separation in the clearance might not occur, and tip-wall vortex cavitation would determine the desinent cavitation number.

When gap cavitation determines the critical cavitation number at $\lambda = 0.064$, this σ_d varies between 15% and 50% higher than σ_d at $\lambda = 0.14$ based on the optimum σ_d . Similarly, when tip-wall vortex cavitation determines the cavitation number at $\lambda = 0.064$, σ_d varies between 20% and 30% lower than σ_d at $\lambda = 0.14$. The unsteady nature of the viscous clearance flow must account for the unpredictable σ_d at $\lambda = 0.064$.

The σ - λ trends are all fairly consistent for $\lambda < 0.15$. The typical σ - λ curve increases almost logarithmically for the range $0.15 < \lambda < 0.40$. As $\lambda = 0.40$ is approached, the curve seems to asymptote to a limiting value. At the largest clearances, the cavitation numbers fall in the range $2.3 < \sigma_d < 2.5$ for all RPM and boundary-layer configurations. The exception is the 502 RPM condition for configuration 2 that has a maximum σ_d of 1.95. This particular curve may have been improperly adjusted by the removal of the air content effects since configuration 2 did not originally have a strong air content influence.

Considering configuration 3 as the typical data set, σ_d at $\lambda = 0.40$ is 25% higher than σ_d at $\lambda = 0.14$, the optimum clearance, for all RPM. The different slopes of the σ - λ trends between the 502 and higher RPM conditions are evident for all configurations. This fact indicates that the different slopes are a result of rotational effects and are not boundary layer dependent.

The slope of the σ - λ trend for $\lambda > 0.15$ must have a physical explanation. Hypothetically, as the clearance increases from $\lambda = 0.15$, the blade tip moves away from the tip-wall and into a higher velocity region of the tip-wall boundary layer. Thus, the velocity through the clearance is increasing as is the shed lift at the tip. The increased velocity must increase the mass flow through the clearance. Therefore, a stronger interaction occurs between the leakage flow and the through flow on the suction side which increases the size and strength of the tip-wall vortex. However, the functional dependence of the vortex structure on the clearance is not known.

As seen in Figure 15b, the slope of the σ - λ trends for configuration 2 are less than configurations 1 and 3 over the range $0.15 < \lambda < 0.40$. The different slopes correlate with the shape factors from Table 1. Configuration 2 has lower shape factors than 1 and 3. A lower shape factor corresponds to a fuller velocity profile that might cause a different σ - λ trend. For a fuller velocity profile the velocity at the tip is higher, and the lift on the tip is increased which creates a stronger tip-wall vortex and higher desinent cavitation numbers.

The three boundary-layer configurations indicate a general trend for the variation with RPM. Typically, σ_d increases with RPM for constant clearance. This trend is distorted for configuration 1 where the 669 RPM condition gives the highest σ_d . Generally, the data for 669 and 836 RPM differ by only a few percent over the range $0.15 < \lambda < 0.40$.

The present data are compared with tip-wall vortex cavitation data from previous investigations in Figure 16. The data from configuration 3 are used from the present investigation. Some data obtained by Gearhart (14) are used for comparison while Mitchell's data are excerpted from Figures 4a, 4b, and 4c. The figure shows a consistent σ - λ trend with optimum clearance between $0.10 < \lambda < 0.15$.

Gearhart's data do not include clearances less than 0.10, so the optimum clearance for his data is taken as 0.10. Also, the slopes for all data are consistent; however, the magnitudes of σ_d are different at constant clearance. Hence, the slope seems independent of the experimental parameters, the air content, the method of determining σ_d , and the test facility. The magnitudes are dependent on one or more of these effects.

The foregoing discussions of the σ - λ trends indicate that the clearance is important to tip-wall vortex cavitation and must be included as a parameter of any model development. The direct correlation of desinent cavitation number with clearance is not evident from the data because the clearance also effects the lift on the tip and the mass flow through the clearance. These values were not measured as a function of clearance, but they directly determine the cavitation results.

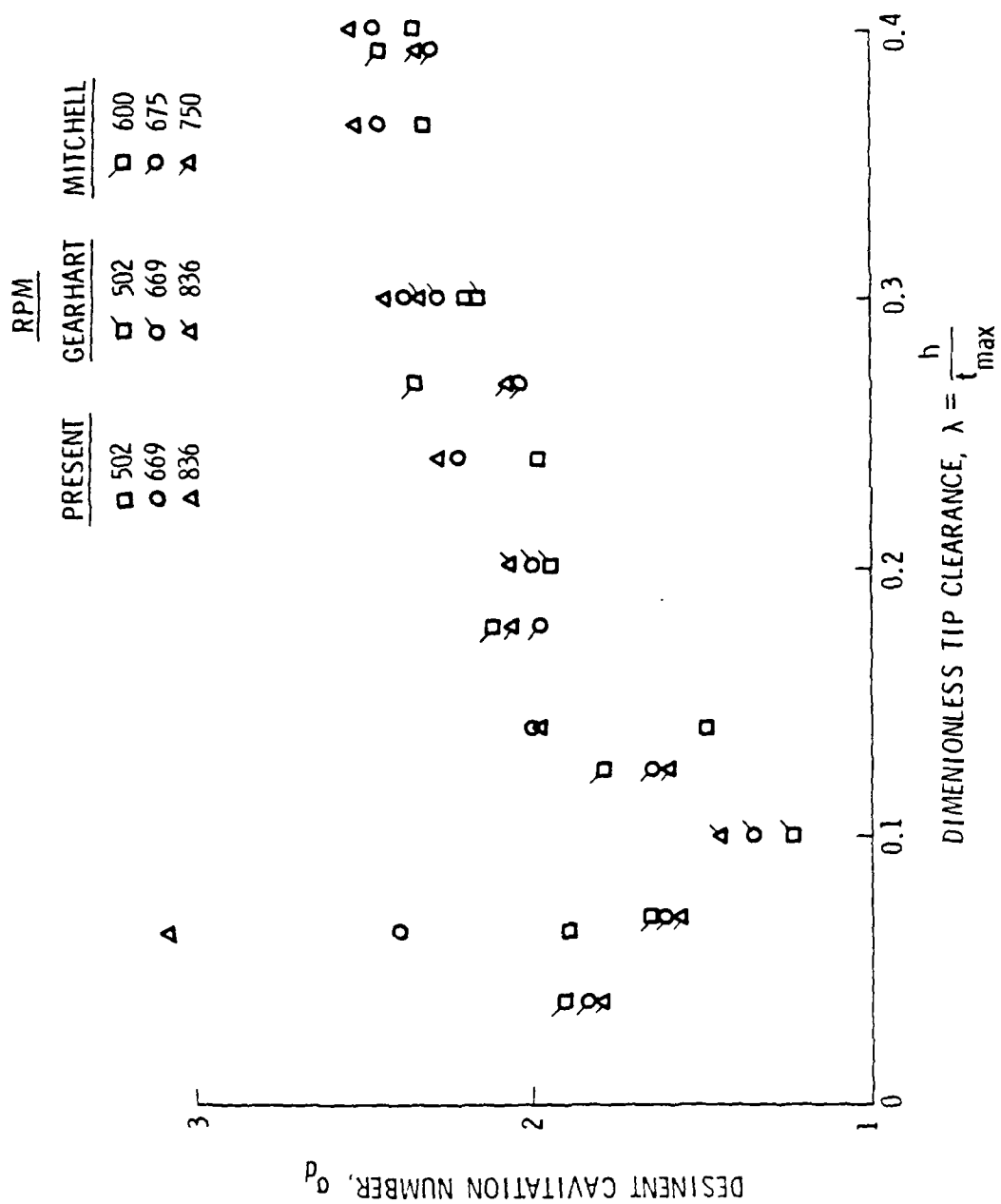


Figure 16. Comparison of Cavitation Data from Mitchell's, Gearhart's and the present investigation.

4.2.2 The σ -RPM Trend. Boundary-layer configuration 3 is shown in Figure 17 as representative of the σ -RPM trend for lines of constant clearance. This section discusses the importance of RPM as a parameter for tip-wall vortex cavitation.

The clearance ratio of 0.064 inches differs markedly from the other lines of constant clearance. Recall that the smallest clearance is in the viscous regime while the other clearances are not. For clearance ratios equal to and greater than 0.14, the σ -RPM trends are similar.

The best cavitation performance is found at $\lambda = 0.14$ for all RPM. For succeeding larger clearances the increment in σ_d decreases with each clearance. For large clearances this increment seems constant with RPM indicating that the slopes are independent of RPM. For $\lambda = 0.40$, the slope is nearly linear and equal to 5.39×10^{-4} . A small slope shows that σ_d has little dependency on RPM at that clearance. A more significant influence is indicated at the optimum clearance where a 33% change in σ_d occurs between the minimum and maximum RPM. Thus, for variable clearance and RPM, the best tip-wall vortex cavitation performance occurs at the optimum clearance, $0.10 < \lambda < 0.15$, and the lowest RPM at the design point.

The small slope of the lines of constant clearance for the σ -RPM trends indicates that the vortex pressure and, hence, the vortex structure vary only slightly with RPM. Inference can be made that the lift shed from the blade tip also varies slightly with RPM. Dean found that the lift at the tip of a rotor would increase with RPM. With more lift on the tip, more is likely to be shed from it.

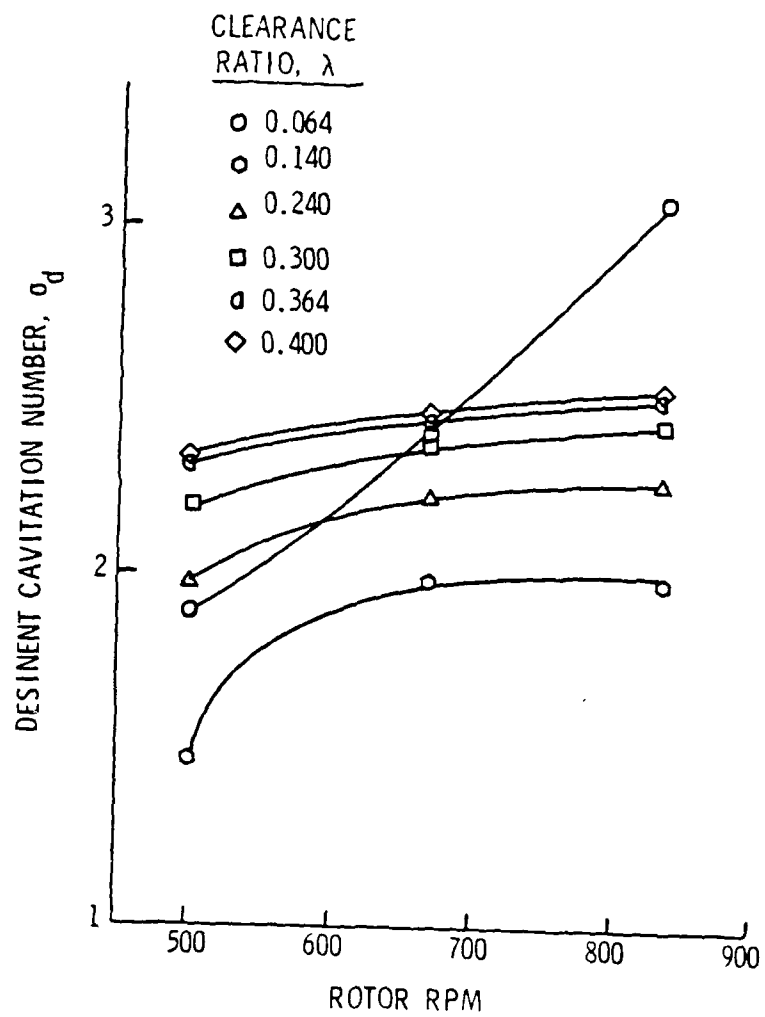


Figure 17. Variation of Desinent Cavitation Number with RPM for Configuration 3.

Therefore, the tip-wall vortex would be stronger and would exhibit poorer cavitation performance with increasing RPM. Dean did not estimate the magnitude for the change in lift with RPM, but the σ -RPM trend at large clearances indicates this change is not significant. Hence, RPM does not seem to be a strong correlating parameter for the analytical model.

4.2.3 The σ -Boundary Layer Trend. Neither the σ - λ nor the σ -RPM trends discussed in the previous sections provided a complete understanding of tip-wall vortex cavitation. Therefore, as speculated earlier, another parameter, likely one from the tip-wall boundary layer, must enter the correlation. The parameter can be derived from the boundary-layer velocity profiles measured during the experimental program. Some parameters can be measured as functions of clearance since the radial coordinate, r , of the profiles is equivalent to the clearance, h . Also, the integral properties can be used as parameters. They are limited to comparisons of the lines of constant clearance since the integral properties are not determined as functions of clearance.

Parameters from the boundary layer are likely to effect the mass flow through the clearance and the lift on the blade tip both of which influence the vortex structure. The mass flow in the clearance depends on the velocity in the clearance that implies the incidence velocity at the tip, W_1 , may be a parameter of importance. Likewise, the lift on the tip depends on the incidence angle of the tip, i .

The incidence velocity is found by constructing the velocity triangles for the relative frame of reference. Thus, W_1 is given by

$$W_1 = \left[W_x^2 + (W_\theta + U_T)^2 \right]^{1/2} \quad (10)$$

The boundary-layer axial velocity, W_x , is taken from the profile data at the desired clearance as is the tangential velocity, W_θ . W_θ adds to the tip speed, U_T , because the tangential velocity direction is opposed to the rotational direction. W_1 is calculated for each clearance. Figure 18 shows the trend in W_1 with λ for boundary-layer configuration 3. The shape of the trend is similar to the σ - λ trend. However, W_1 has only a 3% change over the range of λ , whereas σ_d has a 25% change for the same range. Therefore, W_1 seems to be a correlating parameter, but its effect would be greater if it varied to a higher power.

As a confirmation of its correlation with W_1 , the variations of σ_d with W_1 and W_2^2 are shown in Figures 19a and 19b. For the σ - W_1 trends, the lines of constant RPM are linear for $\lambda > 0.24$. However, the slope of the 502 RPM condition is not consistent with the other RPM conditions. Similarly, the σ - W_1^2 trends are linear for $\lambda > 0.14$ with the 502 RPM condition differing in slope. In each case, the smallest clearance does not fall in the linear range. Since the σ - W_1 trends are linear, W_1 could be a parameter for the eventual correlation model. However, the data are not completely collapsed since the lines of constant RPM do not overlap. Hence, another parameter, which varies more strongly with RPM, must enter the correlation.

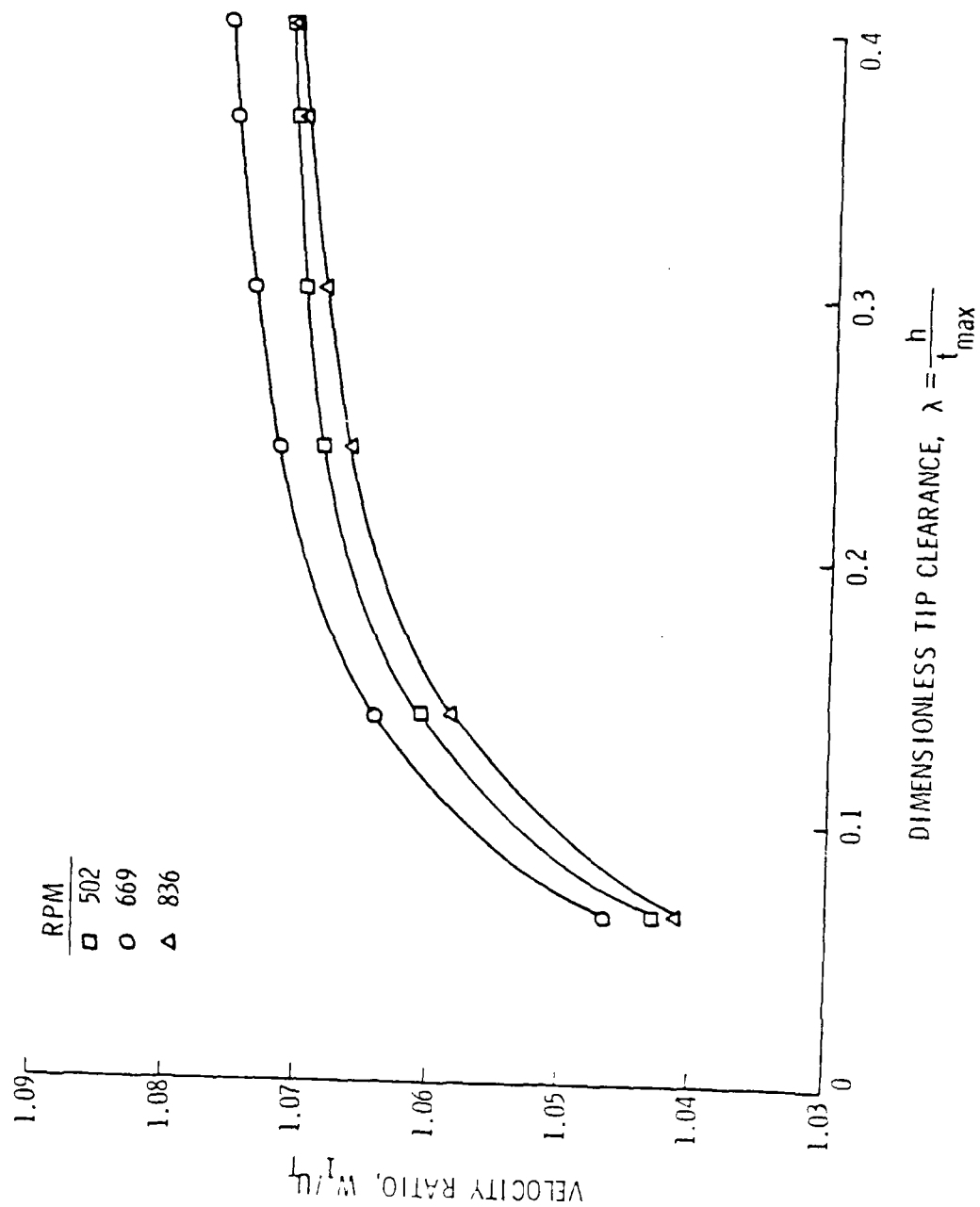
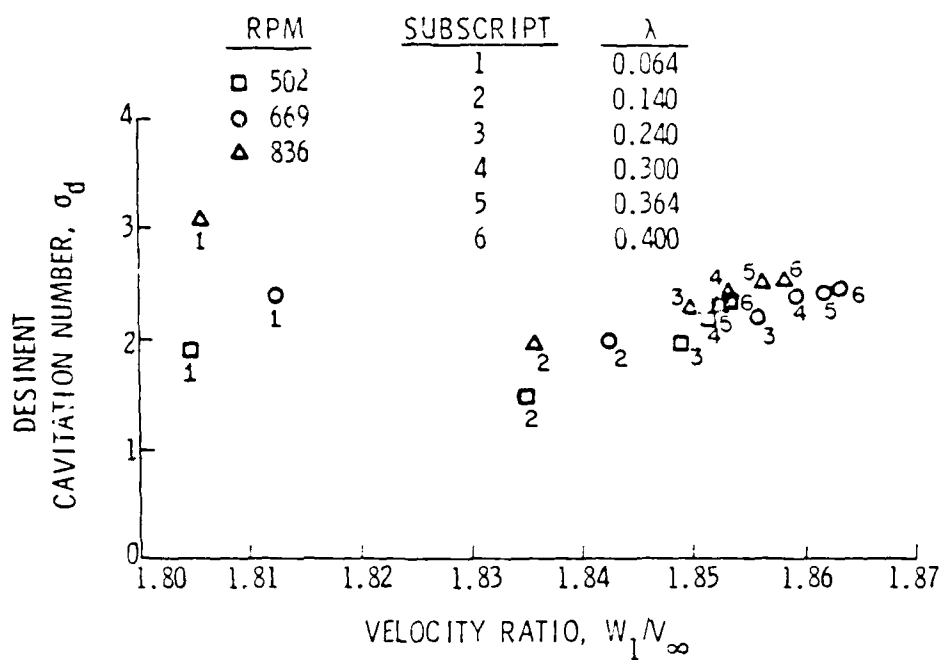
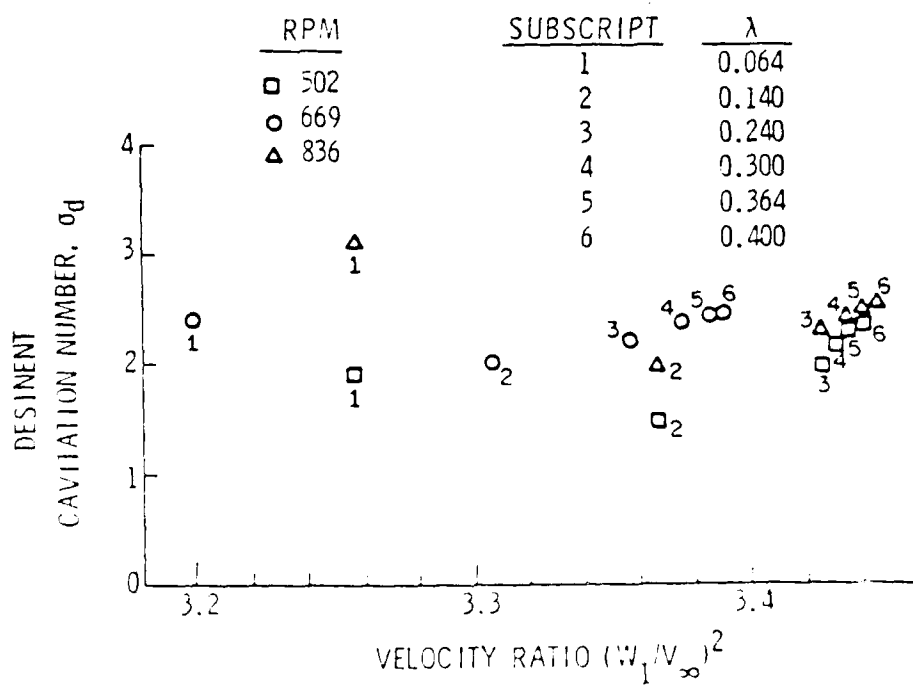


Figure 18. Variation of W_1 with Clearance Ratio for Configuration 3,

Figure 19a. Variation of Cavitation Number with W_1/V_∞ .Figure 19b. Variation of Cavitation Number with $(W_1/V_\infty)^2$.

The incidence angle, i , is calculated from

$$i = \beta_1 - \alpha_{\text{STAG}} - \alpha_{\text{CAM}} \quad (11)$$

where α_{STAG} and α_{CAM} are the stagger and camber angles of the tip section, respectively, known from the blade geometry. The relative inflow angle, β_1 , is given by

$$\beta_1 = \cos^{-1} \frac{W_x}{W_1} \quad (12)$$

Again, i is calculated for each clearance and shown in Figure 20. The trend shows a decreasing i with increasing clearance. If the lift coefficient at the tip is equivalent to i times a constant, the lift coefficient decreases with increasing clearance. Since σ_d increases with clearance, the expected trend is for the shed lift coefficient to increase with clearance. However, i is not a measure of the shed lift. Therefore, σ_d does not correlate with i .

Several points concerning i and the lift on the blade tip must be made. For one, the lift at the tip is fluctuating because perturbations, such as the leakage flow velocity, alter the flow field about the tip. Thus, i , which is calculated from steady-state velocities, is not a realistic indication of the lift on the tip. Secondly, the variation of shed lift with clearance is wanted since the shed lift, or shed circulation, effects the vortex strength, but i is a measure of the total lift on the tip. Considering these points, i is not included as a parameter for the correlation, but the shed lift coefficient is still considered a possible parameter.

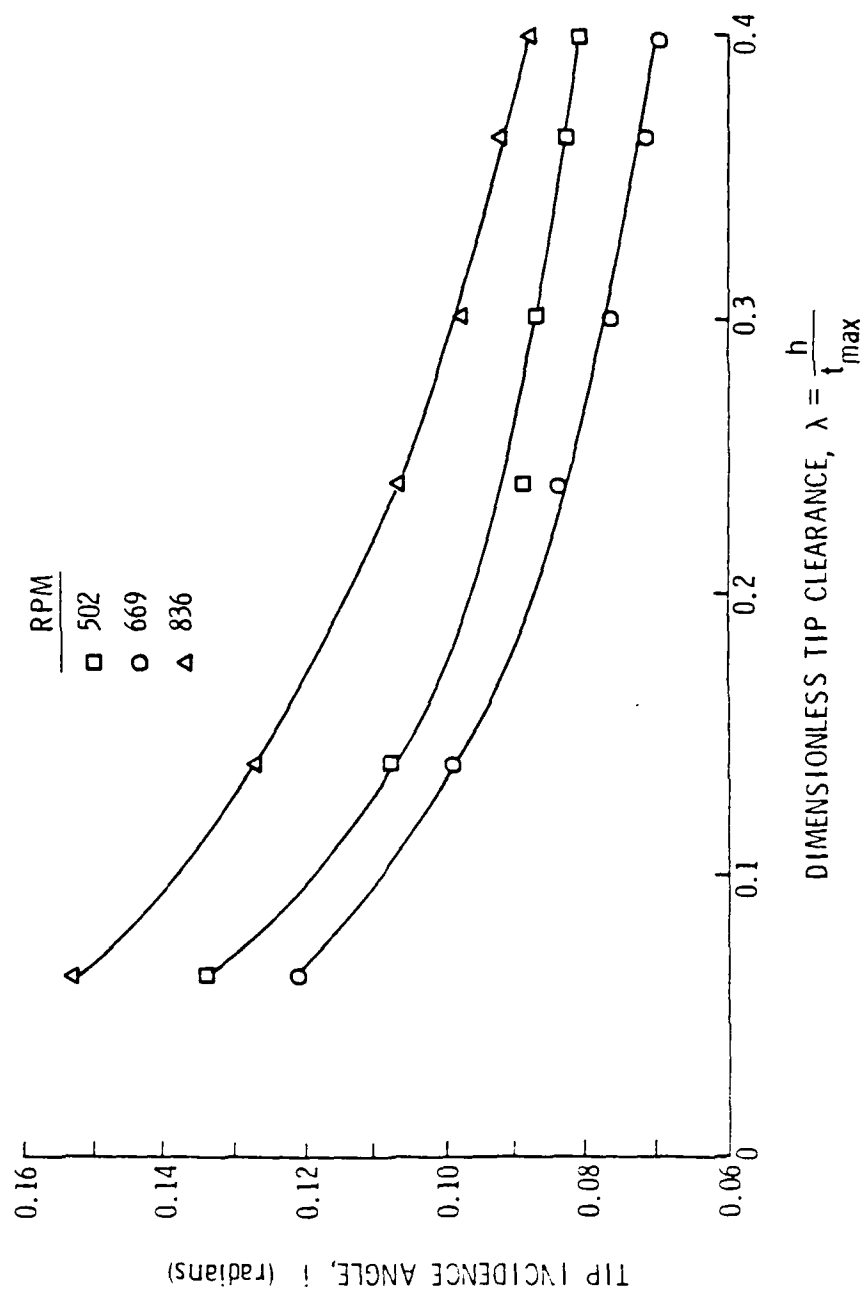


Figure 20. Variation of i with Clearance Ratio.

The integral properties of the boundary layers, as listed in Table 1, are not measured as functions of clearance. Hence, their influence on the σ - λ trend cannot be determined. However, the integral properties may influence the slopes of these trends as discussed earlier for the shape factors of configuration 2. Thus, some consistent trends exist for the integral properties, but they are difficult to include in a correlation model.

4.2.4 Discussion of the Experimental Data. The cavitation desinence data are important for two reasons. First, the data show the values of the parameters required to optimize cavitation performance. Secondly, the trends of the data indicate the important parameters needed for development of an analytical model.

To optimize the tip-wall vortex cavitation performance of a pump stage, the design of the rotor can be tailored using the experimental data. The optimum clearance would be kept between $0.10 < \lambda < 0.15$, irrespective of the RPM and flow coefficient. For the pump stage used in the present investigation, the optimum RPM would be the lowest allowable. Also, for a given RPM the best cavitation performance will be found when the rotor operates on or above its design flow coefficient. An optimum tip-wall boundary layer would reduce the lift on the blade tip. However, other design constraints of the pump determine the contour of the tip-wall and, hence, the boundary-layer size and shape.

Development of the analytical model to predict the cavitation results can be based empirically on the experimental data. This implies that the parameters of the data would be parameters of the

model. For the present investigation, the clearance, RPM, incidence velocity, and shed lift coefficient at the tip would become parameters of the model. The variation of σ_d with λ is substantial, but the functional dependence is not known. The data showed that σ_d varied slightly with RPM at large clearances and more so at small clearances. However, the RPM would not be a necessary parameter for determining the σ - λ trend because the slope of the curve was roughly independent of RPM. The incidence velocity and lift coefficient at the tip are dependent on the tip-wall boundary layer. The data indicate that they are important to the cavitation results and, thus, the model. However, to use the incidence velocity and lift coefficient data empirically, the tip-wall boundary-layer velocity profile must be measured.

4.3 Flow Visualization Results

Recall that an oil-paint film technique as described in Section 3.4 was used for flow visualization. The study was completed for the three RPM used during the experiments. The clearance and boundary-layer configuration were not varied during the oil-paint study program, so only three studies were made. Each oil-paint study was documented by photography for later comparison. Typical photographs of the blade pressure surface, tip surface, and suction surface are displayed in Figures 21a, 21b, and 21c, respectively.

Figure 21a shows the streakline pattern on the pressure surface of the rotor blade. Over most the blade span the transition is indicated by paint build-up at approximately 10% chord and increasing

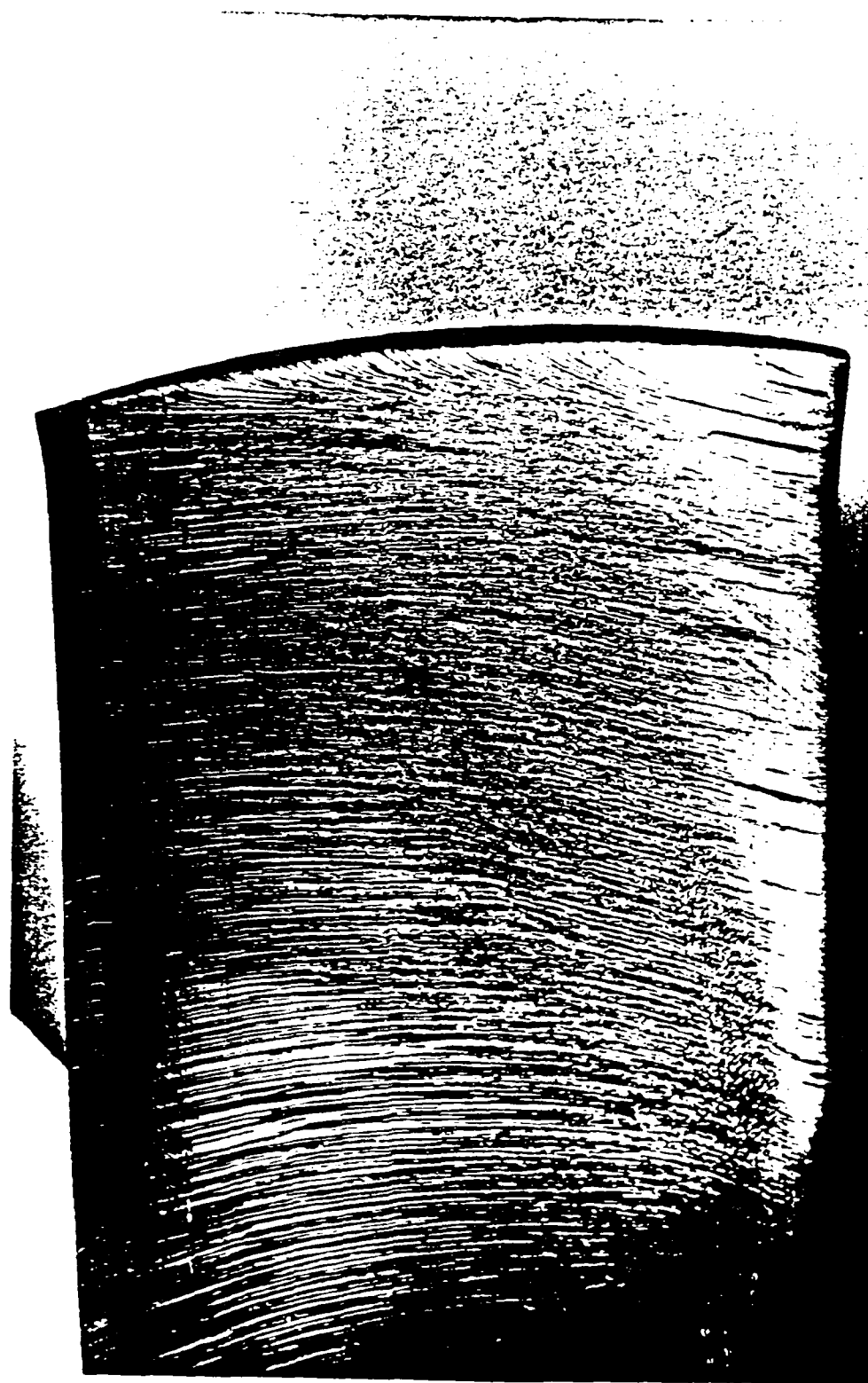


Figure 21a. Oil-Paint Film Pattern on Pressure Surface.



Figure 21b. Oil-Paint Film Pattern on Tip Surface.

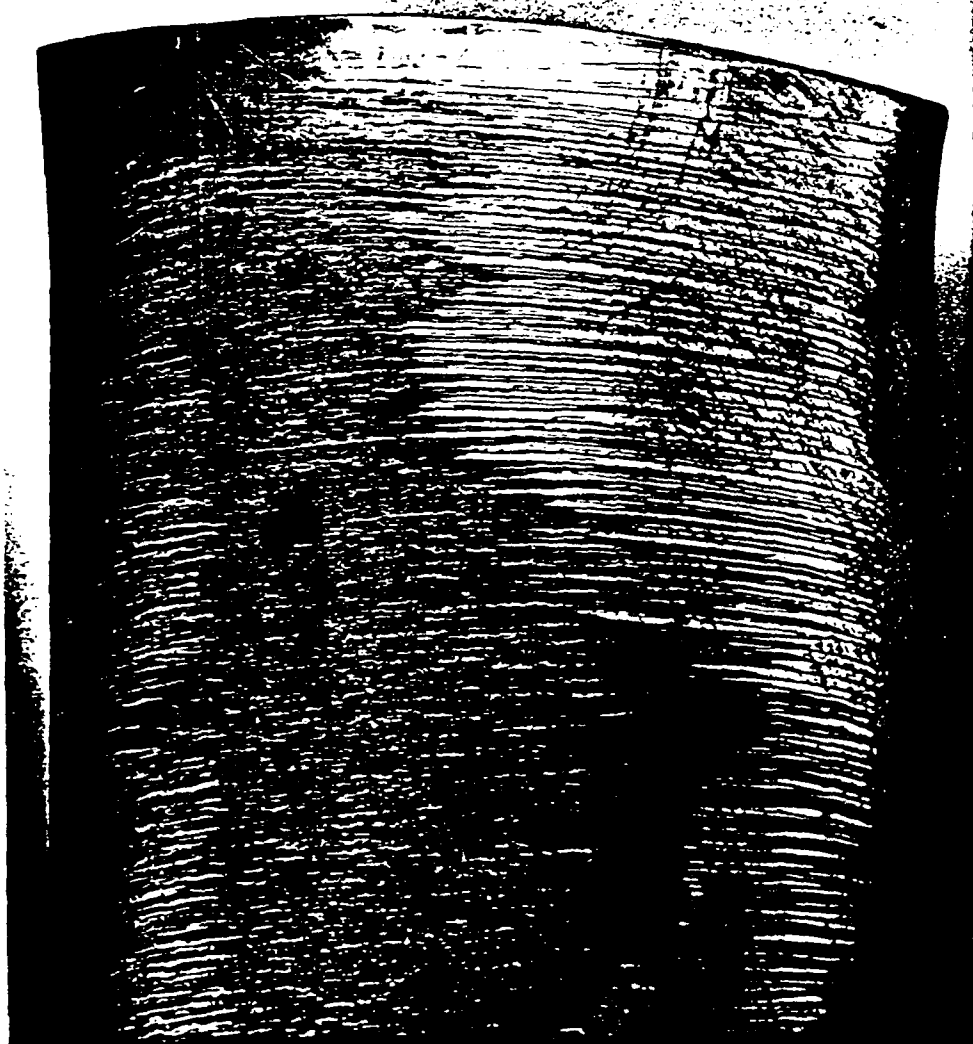


Figure 21c. Oil-Paint Film Pattern on Suction Surface.

to 20% chord near the tip. Generally, transition occurs at a smaller chordwise location for higher RPM. The RPM corresponds to the Reynolds number, and Reynolds number determines transition. Logically, higher RPM corresponds to earlier transition. The streakline pattern indicates no separation of the pressure surface boundary layer. In oil-paint studies, separation is indicated by streaklines abruptly ending on a surface.

The pressure surface pattern indicates that streaklines in the tip region pass into the clearance. Therefore, part of the pressure surface boundary layer enters the clearance as do the blade passage and tip-wall boundary-layer flows. Hence, the pressure surface boundary layer contributes to the clearance flow and, in turn, effects the tip-wall vortex formation. As seen in the photograph, a "dividing" streakline exists that originates somewhere on the blade leading edge and terminates at the blade tip trailing edge. On the tip-side of the "dividing" streakline all streaks pass into the clearance. On the root-side all streaks terminate at the blade trailing edge.

The spanwise location of the "dividing" streakline varies with RPM. For the lowest RPM, the dividing streakline is located furthest from the tip. At the highest RPM this streakline is located closest to the tip.

A photograph of the streakline pattern across the tip surface is shown in Figure 21b. The streaks remain attached while passing from the pressure surface to the tip surface because the corner formed by these surfaces is sufficiently rounded. The lack of separation indicates good gap cavitation performance in the clearance for this

rotor. Over the first 25% chord the streaklines are obliterated. The remaining streaklines crossing the tip make a consistent angle with the tip chord. Using this angle and the stagger angle of the tip chord, a small upstream axial velocity component is calculated for the clearance flow. This is due to the clearance velocity, V , that has a large upstream axial velocity component, induced by the pressure drop from the pressure to suction sides. However, in the rotating frame this induced velocity is tempered by the downstream axial velocity entering the clearance resulting in a smaller upstream component.

At the corner formed by the tip surface and the suction surface, a paint build-up is observed. This build-up indicates that the flow has separated at that location. Separation is expected here because the corner is relatively sharp and clearance flow is entering an adverse pressure gradient.

The suction surface streakline pattern is pictured in Figure 21c. The streaklines are fairly consistent from root to tip. At the 90% chord station, separation occurs because the suction surfaces of this rotor were modified in a previous experiment to get separation at this station. Because the tip-wall vortex should be present at the blade tip, induced radial velocities from the vortex are expected at the tip. However, little radial flow is evident near the tip leading edge. One possible explanation is that the vortex was displaced too far from the suction surface to effect the streaklines.

CHAPTER V

PARAMETRIC CORRELATION MODEL

5.1 Requirements of the Model

Classical cavitation theory states that the cavitation number is equated to the minimum pressure coefficient as

$$\sigma_d = -C_{p_{\min}} \quad (13)$$

Thus, for tip-wall vortex cavitation a model would calculate $C_{p_{\min}}$ of the tip-wall vortex for comparison with σ_d . In this instance, $C_{p_{\min}}$ is calculated as a function of the basic flow field parameters: clearance, RPM, and tip-wall boundary layer. From the data analysis, possible boundary-layer parameters include the incidence velocity and the shed lift coefficient at the rotor tip.

A starting point for generation of the parametric correlation model is the minimum pressure coefficient for the Rankine vortex given in Equation 8

$$C_{p_m} = -2 \left[\frac{\Gamma}{2\pi aV^2} \right]^2 \quad (8)$$

The Rankine vortex satisfies two model requirements. First, the Rankine vortex is inviscid which simplifies the model by excluding viscous effects. Second, Equation 8 includes the parameters: vortex circulation core radius, and reference velocity, that can be found in terms of the basic flow field parameters. Thus, the minimum pressure coefficient

model includes sub-models for circulation, core radius, and velocity. Derivation of the sub-models is accomplished by borrowing from previous model developments and including the data empirically. The resulting model is written functionally as

$$C_{p_{\min}} = f(\text{clearance, RPM, boundary layer}). \quad (14)$$

5.2 Derivation of Circulation and Core Radius Sub-Models

Assuming a Rankine vortex model, the circulation and the core radius of the tip-wall vortex must be known to determine the minimum pressure coefficient and, hence, the cavitation number. Neither the circulation nor the core radius was measured during the experimental program. These values must be estimated as functions of parameters that were measured during the program.

The vortex circulation is estimated from vorticity assumptions. The vorticity in the tip-wall vortex is composed primarily of the vorticity shed from the blade tip. The secondary and scraping vorticity are assumed to be an order of magnitude less than the shed vorticity. The vorticity is related to the circulation as

$$\Gamma = \int_A \underline{\omega} \cdot \underline{n} \, dA. \quad (15)$$

Therefore, if the shed circulation from the blade tip is calculated, it is nearly equivalent to the circulation in the tip-wall vortex. Thus, the shed circulation is used in the model.

The circulation about a section of a finite wing is given by

$$\Gamma = C_L V c/2 \quad (16)$$

where C_L is the section lift coefficient, V is the unperturbed velocity about the section, and $c/2$ is the section semi-chord. The reference velocity, V , is equated with the incidence velocity, W_1 , since it represents the free stream, unperturbed velocity impinging on the blade tip. Using W_1 satisfies two requirements of the model since W_1 is derived from the experimental data and known as a function of the clearance.

Determination of C_L for the circulation sub-model is complicated by the presence of the tip-wall. If the tip-wall is absent, the circulation, hence the lift, shed from the tip is the maximum circulation about the blade. However, when the tip-wall is in proximity to the blade tip, some lift is shed while the remainder is retained on the tip. This phenomenon was measured in separate experiments by Rains (7) and Lakshminarayana (6). Both found that the shed lift varies with the clearance. Lakshminarayana defined a shed lift coefficient at the tip, C_{L_T} , and found it varied with clearance as

$$C_{L_T} \propto h^{2/3} \quad (17)$$

while Rains found the result

$$C_{L_T} \propto h^{1/2} \quad (18)$$

Rains' experiment used a stationary, isolated blade in a water tunnel while Lakshminarayana used a cascade flow. For the pump stage of the present investigation, the blade loading and lift shed at the tip is more similar to Rains' stationary blade. Therefore, the result found by Rains is used in the circulation sub-model. Thus, the shed lift coefficient is given by

$$C_{L_T} = B\sqrt{\lambda} \quad (19)$$

where B is an unspecified constant. Inclusion of Equation 19 into the circulation sub-model gives

$$\Gamma = B\sqrt{\lambda} W_1 c/2 \quad (20)$$

which is an estimation for the circulation of the tip-wall vortex in parametric form. The parameters are the clearance and incidence velocity, a function of the clearance.

A sub-model for the core size, a , must be determined for the $C_{p_{min}}$ model. In Section 2.2.1, Rains' analysis for the roll-up of a vortex sheet is presented. His relationship for the resulting sheet radius, r_c , leads to an equation for the vortex radius, a . Equation 3 is the sheet radius derived by Rains,

$$r_c = 0.14 ht^{*.85} \quad (3)$$

where the vortex coordinate is

$$t^* = (5/c) \sqrt{C_{L_T}/(2\pi)}. \quad (2)$$

AD-A134 357

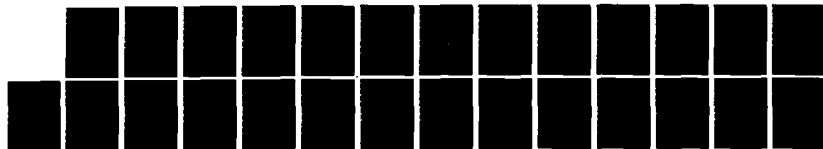
AN INVESTIGATION OF TIP-WALL VORTEX CAVITATION IN AN
AXIAL-FLOW PUMP. (U) PENNSYLVANIA STATE UNIV UNIVERSITY
PARK APPLIED RESEARCH LAB. B H SHUBA 27 MAY 83
ARL/PSU/TM-83-89 N00024-79-C-6043

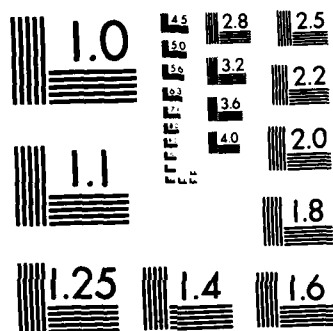
2/2

UNCLASSIFIED

F/G 20/4

NL





MICROCOPY RESOLUTION TEST CHART
NATIONAL BUREAU OF STANDARDS-1963-A

The shed lift coefficient relation of Equation 19 is used in Equation 2.

Also, the product of λ and ϵ in Equation 2 is

$$h/c = \lambda \epsilon. \quad (21)$$

Thus, combining Equations 2, 3, 19, and 21, the sheet radius is given by

$$r_c = 0.14 h \left(\frac{h}{c}\right)^{-.85} (B\sqrt{\lambda})^{.425} \left(\frac{\xi}{c}\right)^{.85}. \quad (22)$$

Rains estimated that the core radius is approximately the sum of the clearance and the sheet radius,

$$a \approx h + r_c. \quad (23)$$

However, Lakshminarayana assumed that the sheet radius is roughly equivalent to the core radius,

$$a \approx r_c. \quad (24)$$

Observations of the core radius made during the present experimental program support Lakshminarayana's result. Typically, the core radius was the order of the clearance, but using Rains' results the estimated radius is increased by a factor of two. Therefore, using Equations 22 and 24, the core radius sub-model can be expressed as

$$a = 0.14 h \left(\frac{h}{c}\right)^{-.85} (B\sqrt{\lambda})^{.425} \left(\frac{\xi}{c}\right)^{.85}. \quad (25)$$

The core radius sub-model is a function of the clearance, the vortex coordinate, ξ , and the blade's geometric properties.

5.3 Application and Discussion of the Model

The parametric correlation model is derived from the minimum pressure coefficient relationship for a Rankine vortex in Equation 8. Using the circulation and core radius relationships of Equations 20 and 25, respectively, and an arbitrary value of the vortex coordinate, ξ , the model becomes

$$C_{p_{\min}} = 0.646 (B\sqrt{\lambda})^{1.15} \left(\frac{W_1}{U_T}\right)^2 \left(\frac{c}{h}\right)^{.30} \left(\frac{c}{\xi}\right)^{1.70} \quad (26)$$

The parameters of this equation include the clearance, h , which determines λ , and the incidence velocity, W_1 , which is a function of the clearance and boundary-layer profile. The constants are B , ξ , U_T , and the rotor blade geometric properties t and c .

The functional variation of the parameters in the model deserve discussion. In Section 4.2.3, the cavitation number was found to vary linearly with W_1^2 , over the range $0.14 < \lambda < 0.40$. Since the model incorporates this same functional nature, it has correctly accounted for the influence of the incidence velocity. Also, in the model, the pressure coefficient varies with clearance to the 0.275 power. Since the $C_{p_{\min}} - \lambda$ trend must duplicate the $\sigma - \lambda$ trend for good correlation, the exponent on h must be less than unity. This exponent gives a shape similar to the $\sigma - \lambda$ trend.

B is the only unspecified value used in the model, and it is not known because the variation of shed lift with clearance is unknown. B is given a value such that the magnitude of $C_{p_{\min}}$ matches σ_d at a given clearance and that the resulting shed lift coefficient is reasonable.

The values of ξ depend on the location of the minimum pressure on the suction side at the blade tip as discussed by Rains (7). Usually, the minimum pressure occurs at the chordwise location of the maximum thickness. Accordingly, ξ is given a percent of chord value equal to the location of the maximum thickness at the blade tip.

The model correlates data for boundary-layer configuration 3 as shown in Figure 22. The values of B required for this correlation are 0.88, 0.905, and 0.935. For comparison, the experimental cavitation data are also plotted in the figure. The magnitude of σ_d and $C_{p_{\min}}$ are similar because the values for B were chosen to give equivalency. The slopes of the curves are also similar over the range $0.15 < \lambda < 0.40$. The model, which is an inviscid analysis, does not predict the trend in the viscous region, $\lambda < 0.15$. Different values for B change the magnitude of the $C_{p_{\min}} - \lambda$ curve, but the slopes do not change significantly. Therefore, the model includes the necessary parameters in their correct functional form to determine the slope of the $\sigma - \lambda$ trend in the inviscid region.

For further verification, the model is used to correlate the data of Mitchell (8) and Gearhart (14). For both sets of data, the boundary-layer profiles required to calculate W_1 were not available. Mitchell had measured a profile at only one RPM. The profiles at the other RPM are estimated from turbulent boundary-layer power law relationships. The profiles for Gearhart's data are generated assuming a turbulent, power law profile and knowing the length of the boundary-layer growth and the edge velocity. Once W_1 is calculated the model predictions for $C_{p_{\min}}$ are made. These are shown for Mitchell's and Gearhart's data in Figures 23

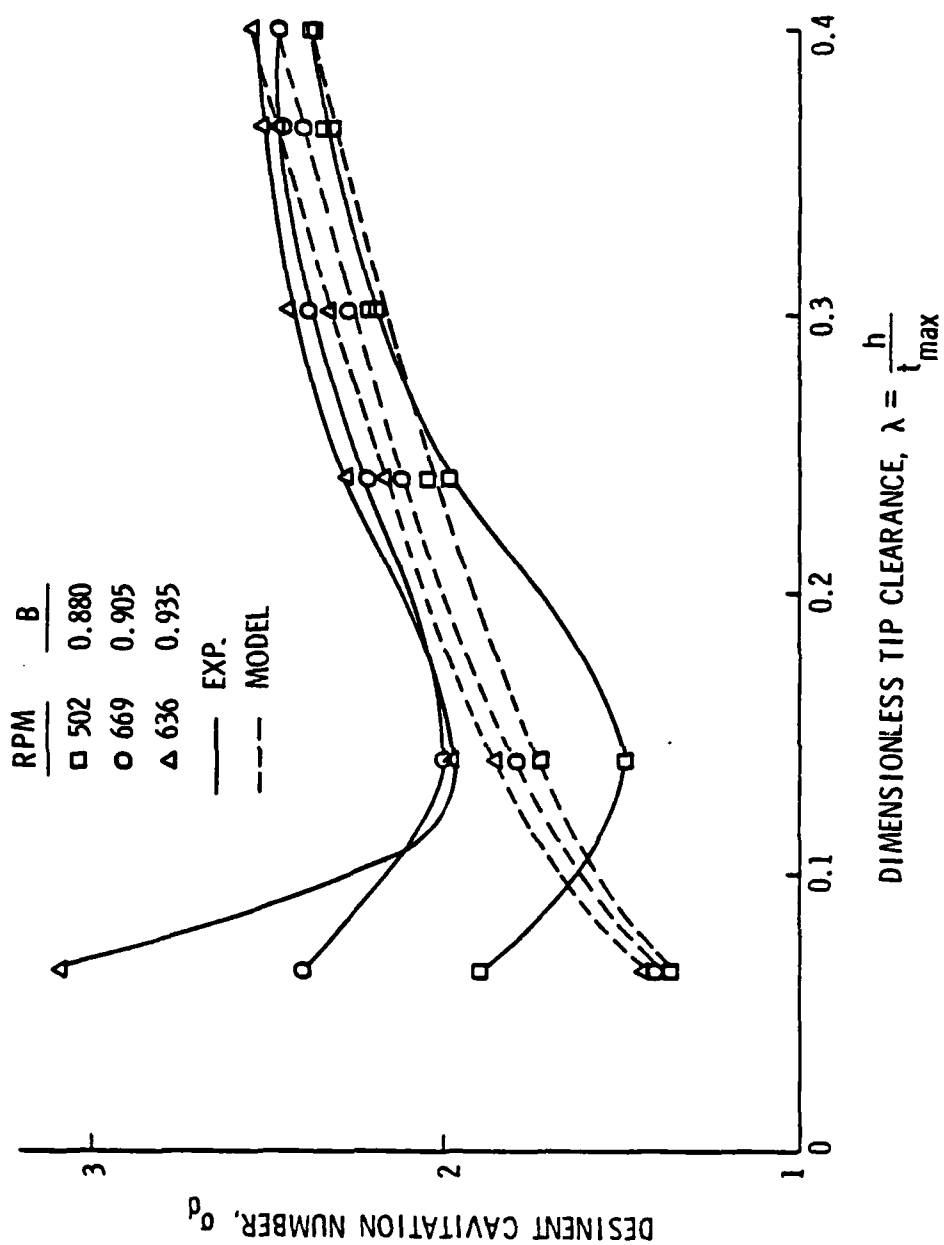


Figure 22. Comparison of Experimental Data and Model Results for the Present Investigation.

and 24, respectively. In both cases, good correlation is evident for slopes and magnitudes of the $C_{p_{\min}} - \lambda$ trends.

Although the same rotor was used by Gearhart and the present investigation, the values of B needed to match the magnitude of σ_d are different. Several reasons are cited for the discrepancy. The inflow conditions to the rotor were different for each experiment. Also, the boundary-layer profiles for Gearhart's data were estimated. In addition, the air content of the water, which has a strong effect on cavitation, was not identical in both experiments. Possibly, the static pressures used to calculate the cavitation inception or desinence numbers were not measured at consistent locations for both investigations.

Finally, observing the correlations for Mitchell, Gearhart, and the present investigations, the experimental data show a significant variation with RPM. The only variation with RPM in the model is the implicit variation of W_1 . As RPM increases, the boundary layer fills out, and W_1 increases. An explicit dependency on RPM may be justified since σ_d varies by as much as 25% over the range of RPM at constant clearance. This dependency on RPM may enter through the constant B .

In addition to $C_{p_{\min}}$, the model calculates the shed lift coefficient and the vortex core radius. These values are plotted as functions of the clearance in Figures 25 and 26 for Mitchell, Gearhart, and the present investigation.

In Figure 25, the estimation for the shed lift coefficient, C_{L_T} , is greater for Gearhart and the present investigation than for Mitchell's data. The magnitude of C_{L_T} is more realistic for the former

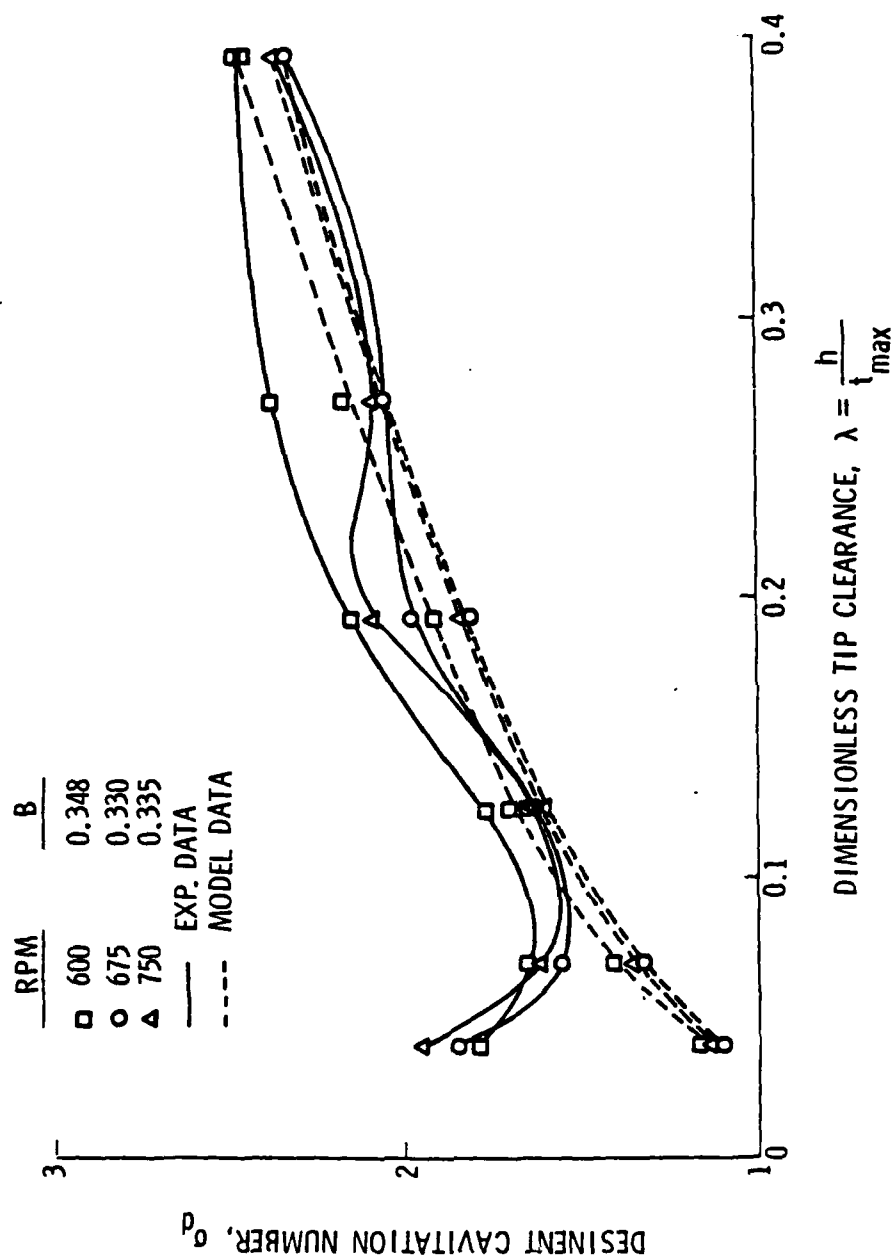


Figure 23. Comparison of Experimental Data and Model Results for Mitchell's Investigation.

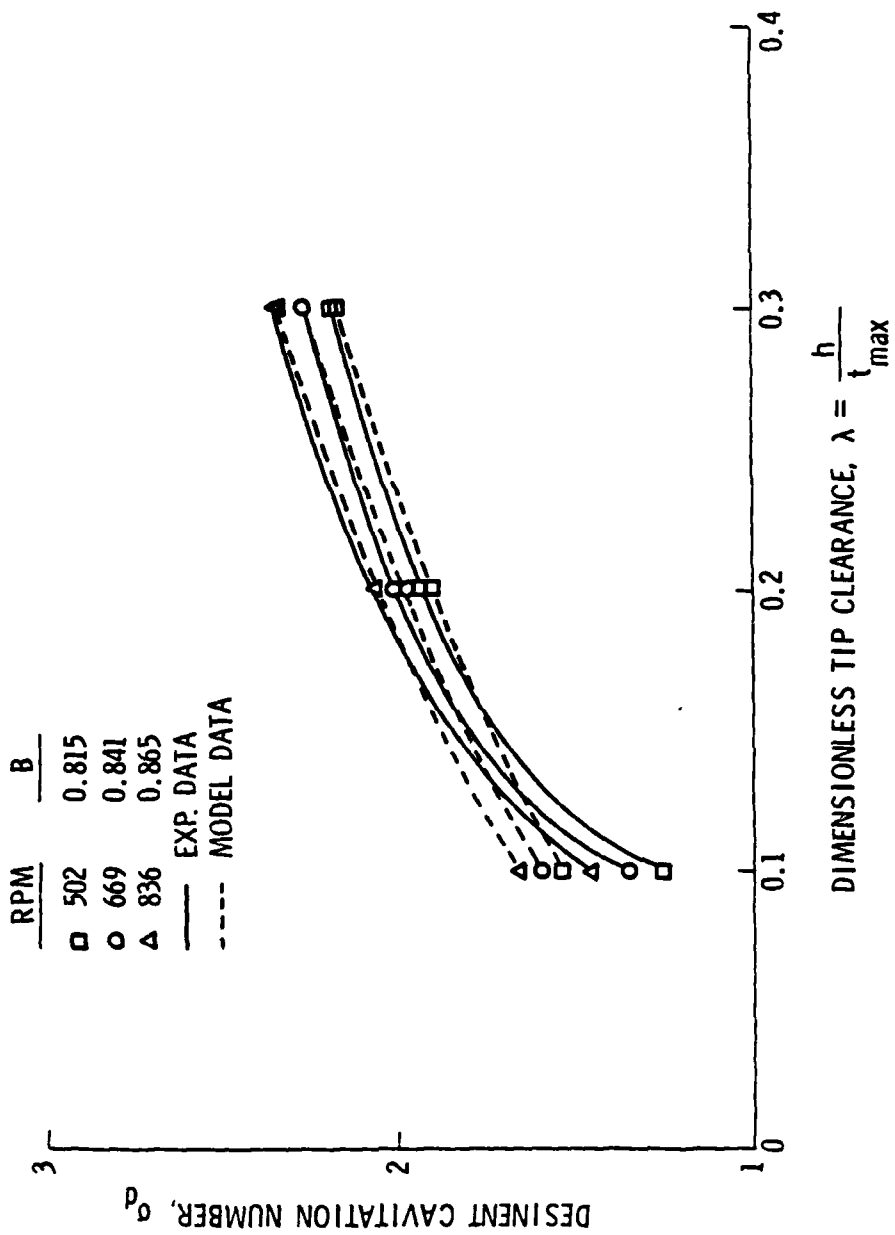


Figure 24. Comparison of Experimental Data and Model Results for Gearhart's Investigation.

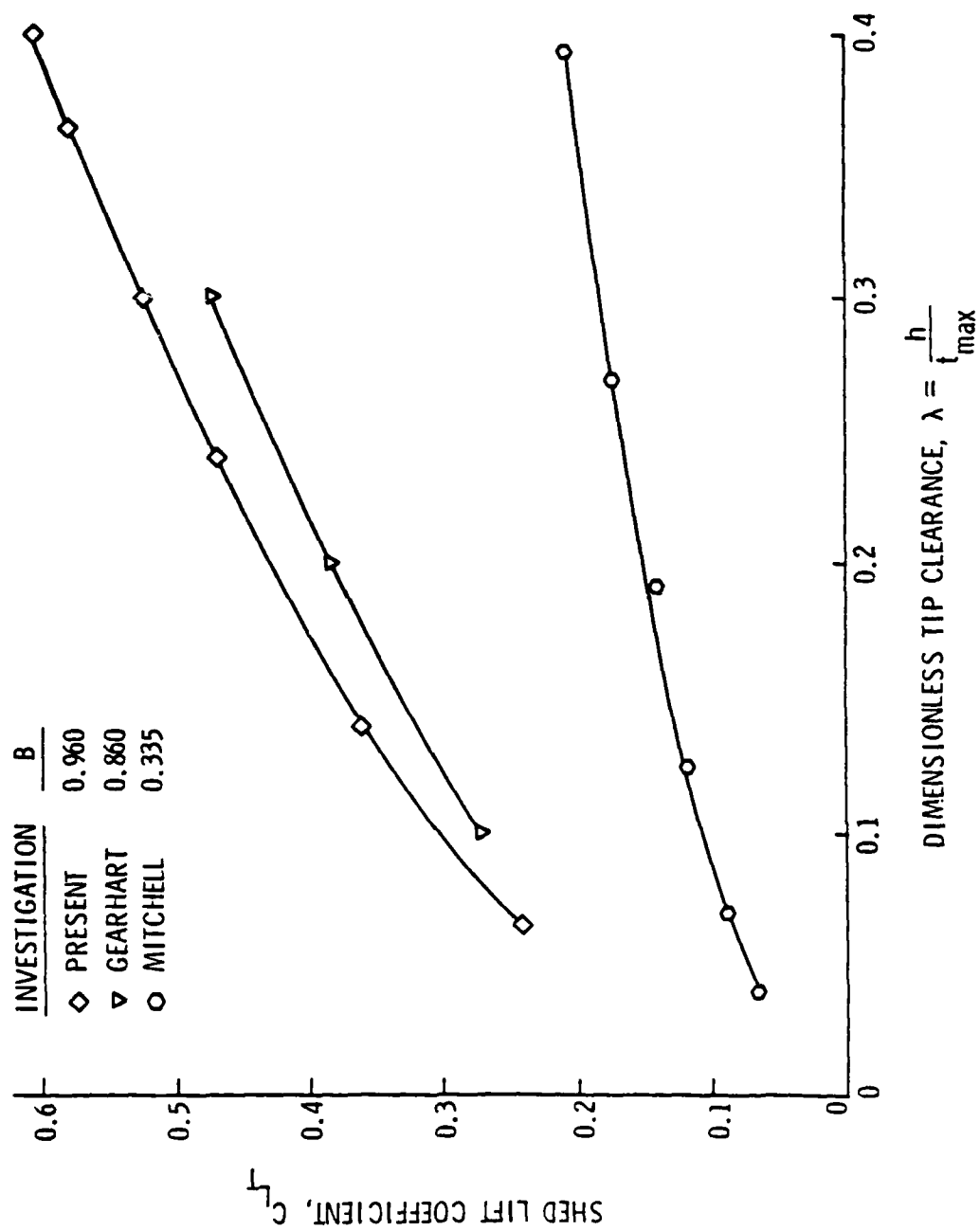


Figure 25. Model Estimates of Shed Lift Coefficient.

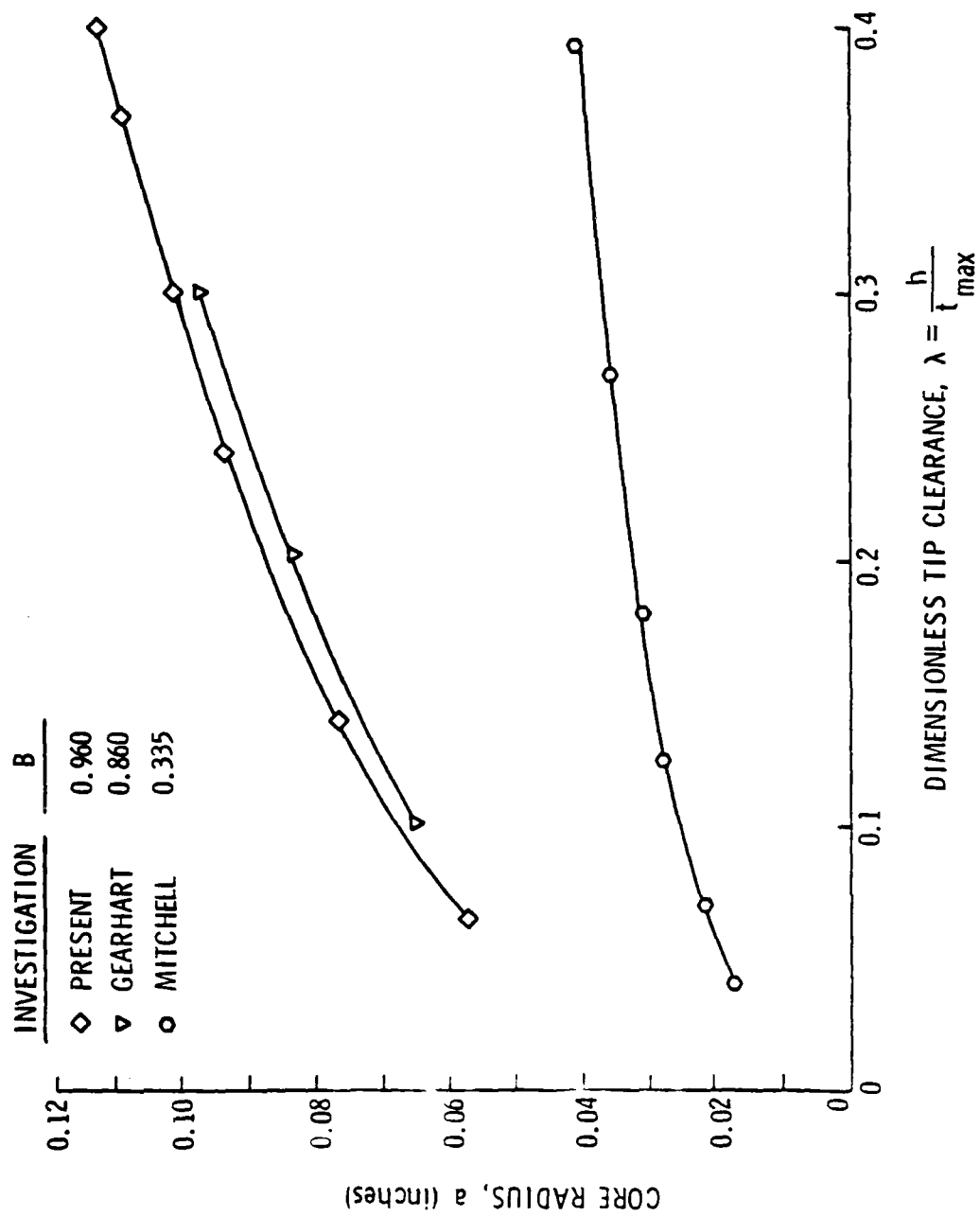


Figure 26. Model Estimates of Vortex Core Radius.

investigations than the latter because typical lift coefficients for rotor blade tips are roughly 0.50 to 0.80. Unless the rotor blade tip for Mitchell's investigation were designed for low loading, the C_{L_T} seems unreasonable. The reason for this difference is more likely the value of B . A higher value of B gives a higher C_{L_T} at constant clearance. Since a lower value of B is needed to match the model with Mitchell's σ - λ trend, it also reduces the value of the shed lift coefficient.

A similar observation and conclusion is made for the core radius estimations in Figure 26. The radii of Gearhart's and the present investigation are larger than that of Mitchell. Again, the value of B is primarily responsible for this difference. However, visual observations of the cavitating vortex indicate that the radius is roughly 0.05 inches. Thus, Mitchell's radii are more realistic than the others. However, the visual observations are not accurate, so the correct estimation for the core radius is not known conclusively.

From the comparisons of the model with the experimental data an estimate for the functional nature of B can be made since different values of B are required for different RPM. Therefore, B may be a function of RPM or the related Reynolds number effect.

RPM is converted to a Reynolds number, R_e , as

$$R_e = \frac{W C}{\nu} \quad (27)$$

where W is the mean relative velocity of the pump stage. Each RPM has a corresponding value of W . B is given for varying R_e in Figure 27 for data by Gearhart and the present investigation. Mitchell's data are

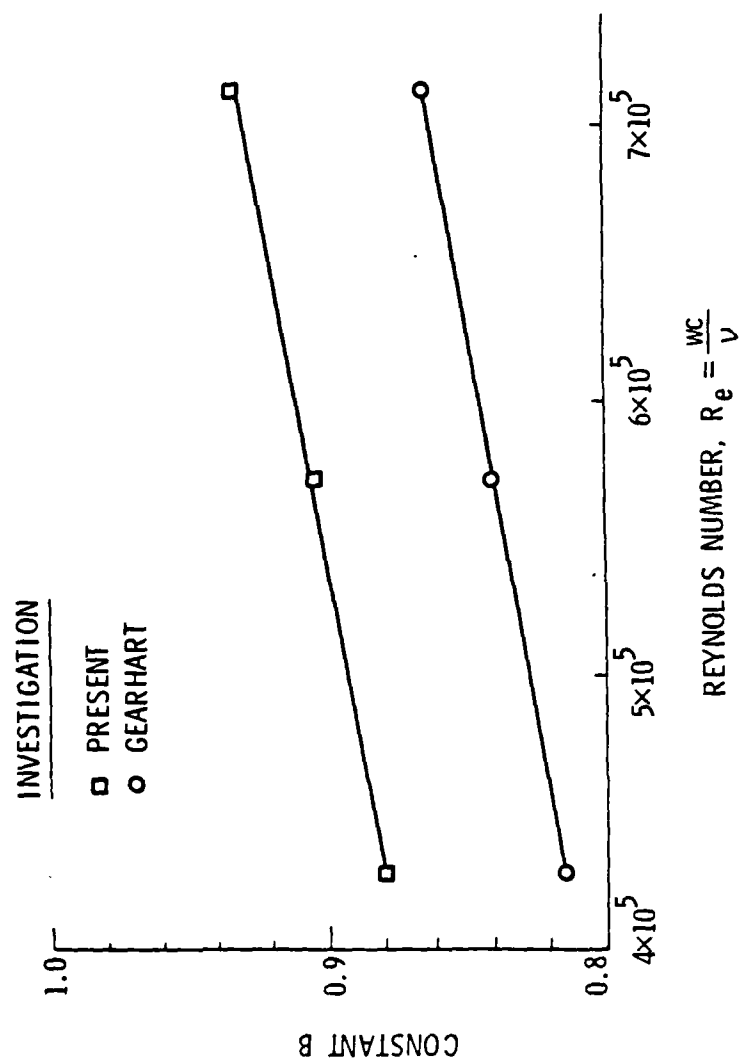


Figure 27. Variation of B with Reynolds Number.

not included because it failed to show a consistent trend with RPM.

In Figure 27, two lines exist since different values of B are required for each correlation. These lines are straight and have the same slope. Therefore, the equation of the lines is written as

$$B = 1.93 \times 10^{-7} R_e + B_{INT} \quad (28)$$

where B_{INT} is the intercept on the B axis. Equation 28 gives the functional variation of B with Reynolds number effect.

Since B determines the shed lift coefficient, lift is now known as a function of clearance and Reynolds number. Thus, as Dean (3) found increasing lift with RPM, Equation 28 determines the magnitude of increase. However, the validity of this estimate depends on the validity of the entire model.

CHAPTER VI

CONCLUSIONS OF THE INVESTIGATION

6.1 Conclusions from the Experimental Program

The results of the experimental data provide several important conclusions concerning tip-wall vortex cavitation. First, the present data prove that the trends for desinent cavitation number with clearance are repeatable. Secondly, an optimum clearance exists in the range of $\lambda < 0.15$. Thirdly, the effect of air content on cavitation is important. Lastly, the conditions for optimum tip-wall vortex cavitation are known.

The repeatability of the σ - λ trend is seen both within the present data and in comparison with previous data. Within the present investigation, nine σ - λ trends are determined for three RPM at three boundary-layer configurations. Six of these trends have roughly the same slope. Only configuration 2 shows a different slope, and the boundary-layer shape factor is expected to explain the difference. Comparing the present and previous data shows that the σ - λ trends are similar for all the investigations. The slopes of these trends are similar while the magnitudes vary slightly. Since the slopes are consistent, the σ - λ trend is a basis for a correlation model.

The present data show an optimum clearance equal to or less than λ of 0.15. If vortex cavitation occurs for $\lambda < 0.15$, the clearance for this λ is the optimum. If gap cavitation occurs in the clearance for $\lambda < 0.15$, the cavitation number at this λ is higher than that at $\lambda = 0.15$, and the optimum clearance remains at $\lambda = 0.15$. Both

forms of cavitation are observed in the present investigation which explains the different shapes of the σ - λ trends for $\lambda < 0.15$. If the tip is designed to minimize gap cavitation, tip-wall vortex cavitation determines the cavitation number. In this case the optimum clearance would be less than $\lambda = 0.15$. Therefore, the optimum clearance is determined by the form of cavitation occurring in the range $\lambda < 0.15$.

The present investigation shows the effects of air content on vortex cavitation. Before the air content effects were removed, the data exhibited reversed trends with RPM. The cavitation number increased with decreasing RPM at constant clearance. Also, the magnitudes of the cavitation number were exaggerated. After the effects were removed, the data assumed their expected trends. Thus, unless an experimental program controls the effects of air content, the actual trends of the cavitation data remain uncertain.

These data show what the values of the clearance, RPM, and tip-wall boundary-layer should be for optimum tip-wall vortex cavitation performance. As discussed earlier, the clearance should be in the range $\lambda < 0.15$ depending on the form of cavitation that occurs at the tip. For nearly all the data the lowest cavitation numbers occur for the lowest RPM condition. Typically, cavitation number increased with increasing RPM. Therefore, the optimum cavitation performance with respect to RPM should be found at the lowest RPM allowable. The magnitudes of the cavitation data do not show significant variation with boundary-layer configuration. However, a tip-wall boundary layer that reduces the loading, or lift, on the tip is desirable since it improves the tip-wall vortex cavitation performance.

6.2 Conclusions of the Parametric Correlation Model

Several conclusions can be made about the model. First, the model correlates the present and previous data. Secondly, only one unspecified constant enters the model calculations, so the model is almost complete.

The model duplicates the experimental σ - λ trend over the range $0.1 < \lambda < 0.4$ for present and previous data. Different values of B are required by the model for each investigation because each used different rotors or flow conditions. For the data of Gearhart and Mitchell, the model correlates the data despite the estimated boundary-layer profiles. Therefore, this model may also correlate future data for tip-wall vortex cavitation.

The unspecified constant, B , deserves discussion. B determines the magnitude of the shed lift coefficient as shown in Equation 19. For the model, increasing B increases the magnitude of $C_{p_{\min}}$ but leaves the slope of the $C_{p_{\min}}$ - λ trend unaffected. Therefore, the nature of B deserves more investigation.

The magnitudes of the cavitation numbers are effected by RPM, and B accounts for these magnitudes. Therefore, B is likely the parameter that measures the increasing lift found by Dean for increasing RPM. However, no data are available to verify the functional form of B found in this investigation. The model is sufficient in its present form to correlate tip-wall vortex cavitation.

CHAPTER VII

RECOMMENDATIONS FOR FURTHER RESEARCH

Before being used to predict cavitation performance, the parametric correlation model should be validated by experimental techniques. The functional relationships for shed lift coefficient and core radius developed for the model should be verified. This will determine the nature of the constant B . For the experimental data, the trend in vortex cavitation with air content should be studied.

The lift shed from the rotor blade tip can be determined by laser velocimetry. Using the laser velocimeter, the velocities on the pressure and suction sides of the tip can be measured at chordwise stations for varying clearance and RPM. These velocities can be integrated to get the lift on the tip as a function of clearance and RPM. In coefficient form, this lift can be compared with Equations 19 and 28 to determine the nature of B .

The core radius can also be measured by laser velocimetry. This was attempted during the present investigation but was too time consuming to be completed. The radii can be measured at chordwise stations for varying clearance and RPM. This data can be compared with the core radii predicted by the model. Since B is a parameter of the core radius sub-model, the nature of B can be found by comparing the laser data with the sub-model relationship.

Thus, two methods can be used to verify the functional form of the constant B . If both methods give approximately equal values for B , the parametric correlation model is validated. If the methods

give unequal values for B , the model is invalidated which suggests that the model is not parametrically correct.

Air content effects occurred during the present experimental program that drastically altered the trends in vortex cavitation. These effects can be studied by including air content as a parameter in an investigation similar to the present one. In this manner, air content effects can be systematically studied for vortex cavitation.

REFERENCES

1. Hansen, A. G., Herzig, H. Z., and Costello, G. R., "A Visualization Study of Secondary Flows in Cascades," NACA TN 2947, 1953.
2. Allen, H. W., and Kofskey, M. G., "Visualization Study of Secondary Flows in Turbine Rotor Tip Regions," NACA TN 3519, September 1955.
3. Dean, R. C., "The Influence of Tip Clearance on Boundary-Layer Flow in a Rectilinear Cascade," Gas Turbine Laboratory, Massachusetts Institute of Technology, December 1954.
4. Gearhart, W. S., "Tip Clearance Cavitation in Shrouded Underwater Propulsors," AIAA, J. Aircraft, Vol. 3, No. 2, March-April 1966.
5. Lakshminarayana, B., "Methods of Predicting the Tip Clearance Effects in Axial Flow Turbomachinery," ASME Transactions, J. Basic Engineering, September 1970.
6. Lakshminarayana, B., and Horlock, J. H., "Leakage and Secondary Flows in Compressor Cascades," Department of Mechanical Engineering, The University of Liverpool, Reports and Memoranda No. 3483, March 1965.
7. Rains, D. A., "Tip Clearance Flows in Axial Flow Compressors and Pumps," Hydromechanics and Mechanical Engineering Laboratories, California Institute of Technology, Report No. 5, June 1954.
8. Mitchell, A. B., "An Experimental Investigation of Cavitation Inception in the Rotor Blade Tip Region of an Axial Flow Pump," Admiralty Research Laboratory, ARL/RI/G/HY/11/2, August 1958.
9. McCormick, B. W., "On Cavitation Produced by a Vortex Trailing From a Lifting Surface," ASME Transactions, J. Basic Engineering, September 1962.
10. Billet, M. L., "The Effect of Secondary Vorticity on the Inception of Vortex Cavitation," ASME Transactions, J. Fluids Engineering, March 1981.
11. Bechtel, W. T., "The Influence of Surface Irregularities on Cavitation: Field Study and Limited Cavitation Near Wire Screen Roughness," M.S. thesis, Department of Aerospace Engineering, The Pennsylvania State University, 1971.
12. Lehman, A. F., "The Garfield Thomas Water Tunnel," Ordnance Research Laboratory Report No. NORD16597-56, September 30, 1959.

13. Kuiper, G., "Cavitation Inception on Ship Propeller Models,"
Doctoral thesis, Technological University in Belft, The Netherlands,
March 1981.
14. Gearhart, W. S., Private communications.

APPENDIX:

DERIVATION OF SECONDARY AND VORTEX CIRCULATION

The circulation that results from the secondary vorticity generated in the clearance is compared with the estimated circulation of the tip-wall vortex. The secondary vorticity is calculated from vorticity relationships for a relative frame of reference, and the estimated circulation is calculated from the Rankine vortex pressure coefficient relationship.

The form of the equation for secondary circulation as given by Billet (10) is

$$\Gamma = 2\pi \int_{r_1}^{r_2} r \underline{\omega}'_{s_2} \cos \beta_2^* dr \quad (29)$$

where β_2^* is the relative flow outlet angle and $\underline{\omega}'_{s_2}$ is the secondary vorticity generated in the clearance. $\underline{\omega}'_{s_2}$ is found from

$$\underline{\omega}'_{s_2} = \underline{\omega}'_{s_1} + 2\Delta\beta \underline{\omega}'_{n_1} \quad (30)$$

where $\underline{\omega}'_{s_1}$ is the relative streamwise vorticity entering the clearance, and $\underline{\omega}'_{n_1}$ is the relative normal vorticity. These values are found from

$$\underline{\omega}'_{s_1} = \omega_n \sin \beta_1 \quad (31)$$

$$\underline{\omega}'_{n_1} = \omega_n \cos \beta_1 \quad (32)$$

where ω_n is the normal vorticity and β_1 is the relative flow inlet angle. ω_n is calculated from the boundary-layer velocity profile data. Integrating Equation 29, the secondary circulation calculated

for varying clearances is listed in Table II.

The estimated circulation is found from Equation 8 solving for the circulation. This relationship is given as

$$\Gamma = \pi a V \sqrt{2\sigma} . \quad (33)$$

For the calculations, the core radius is estimated as equal to the clearance. V is set equal to 15 feet per second corresponding to the lowest RPM of the investigation. σ is set equal to 2.5 that is a typical cavitation number for these conditions. The calculated results are shown in Table II.

Comparing the results in Table II, the estimated circulation of the tip-wall vortex is an order of magnitude greater than the secondary circulation. Since the secondary circulation is not substantial, it must not be a major contributor to the tip-wall vortex.

TABLE II

COMPARISON OF SECONDARY AND VORTEX CIRCULATION

<u>Clearance</u>	<u>Secondary Circulation</u>	<u>Vortex Circulation</u>
.016 (in)	0.59 (in ² /s)	20.22 (in ² /s)
.035	1.87	44.26
.060	3.11	75.87
.075	4.04	94.83
.091	4.43	115.10
.100	4.92	126.40

DISTRIBUTION LIST FOR UNCLASSIFIED ARL TM 83-89 by B. H. Shuba, dated
May 27, 1983

Commander
Naval Sea Systems Command
Department of the Navy
Washington, DC 20362
Attn: Library
Code NSEA-99621
(Copy Nos. 1 and 2)

Naval Sea Systems Command
Attn: T. E. Peirce
Code NSEA-63R31
(Copy No. 3)

Naval Sea Systems Command
Attn: Code NSEA-63R3
(Copy Nos. 4 and 5)

Naval Sea Systems Command
Attn: F. B. Peterson
Code NSEA-56X
(Copy No. 6)

Naval Sea Systems Command
Attn: Code NSEA-9961
(Copy Nos. 7 and 8)

Commander
David W. Taylor Naval Ship R&D Center
Department of the Navy
Bethesda, MD 20084
Attn: Library
Code 522
(Copy No. 9)

David W. Taylor Naval Ship R&D Center
Attn: R. J. Boswell
Code 1544
(Copy No. 10)

David W. Taylor Naval Ship R&D Center
Attn: K. D. Remmers
Code 1522
(Copy No. 11)

David W. Taylor Naval Ship R&D Center
Attn: J. H. McCarthy
Code 1540
(Copy No. 12)

David W. Taylor Naval Ship R&D Center
Attn: T. E. Brockett
Code 1544
(Copy No. 13)

David W. Taylor Naval Ship R&D Center
Attn: A. F. Kilcullen
Code 1962
(Copy No. 14)

Commanding Officer
Naval Underwater Systems Center
Department of the Navy
Newport, RI 02840
Attn: Library
Code 54
(Copy No. 15)

Commanding Officer
Naval Ocean Systems Center
Department of the Navy
San Diego, CA 92152
Attn: Library
(Copy No. 16)

Commander
Naval Surface Weapons Center
Department of the Navy
Silver Spring, MD 20910
Attn: Library
(Copy No. 17)

Defense Technical Information Center
5010 Duke Street
Camerson Station
Alexandria, VA 22314
(Copy Nos. 18 through 23)

Naval Research Laboratory
Department of the Navy
Washington, DC 20390
Attn: Library
(Copy No. 24)

Office of Naval Research
Department of the Navy
800 N. Quincy Street
Arlington, VA 22217
Attn: Director
(Copy No. 25)

DISTRIBUTION LIST FOR UNCLASSIFIED ARL TM 83-89 by B. H. Shuba, dated
May 27, 1983

Office of Naval Research
Attn: C. Lee
(Copy No. 26)

The Pennsylvania State University
Applied Research Laboratory
Post Office Box 30
State College, PA 16801
Attn: GTWT Files
(Copy No. 27)

Applied Research Laboratory
Attn: J. W. Holl
(Copy Nos. 28 through 32)

Applied Research Laboratory
Attn: M. L. Billet
(Copy No. 33)

Applied Research Laboratory
Attn: W. S. Gearhart
(Copy No. 34)

Applied Research Laboratory
Attn: R. E. Henderson
(Copy No. 35)

Dr. Allan J. Acosta
Division of Engineering and
Applied Science
California Institute of Technology
Pasadena, CA 91125
(Copy No. 36)

END